Non-Linear Conductance at the Superconductor-Insulator Transition in Titanium Nitride

Dissertation
zur Erlangung des Doktorgrades der Naturwissenschaften
(Dr. rer. nat.)
Fakultät für Physik
der Universität Regensburg
vorgelegt von
David Kalok
aus Merlau

January 24, 2012

Die Arbeit wurde von Prof. Dr. Christoph Strunk angeleitet.
Das Promotionsgesuch wurde am 27.10.2011 eingereicht.
Das Kolloquium fand statt am 19.01.2012

Prüfungsausschuss:	Vorsitzender:	Prof. Dr. Andreas Schäfer
	1. Gutachter:	Prof. Dr. Cristoph Strunk
	2. Gutachter:	Prof. Dr. Milena Grifoni
	weiterer Prüfer:	Prof. Dr. Sergey Ganichev

SIGILLUM UNIVERSITATIS RATISBONENSIS

Contents

Chapter 1

Introduction

Traditionally, solid materials are separated in metals and insulators. The Fermi liquid model and with it the modified Drude formula can be applied for metals very well and can describe most of the observed behavior, e.g. heat capacity and resistivity. When cooling down a metal one would expect that the resistivity is going down since the number of phonons is decreasing and with that the electron-phonon scattering either. At very low temperature the resistance should then saturate, at a value that is determined by the impurities, or the system falls into a superconducting coherent state with no resistance. The superconducting state can be destroyed by applied magnetic field and the system is then expected to be in its metallic state again. This works for most superconducting bulk metals. However, for very disordered systems, in particular thin films, this does not hold. Thin films means that the film thickness is in the order or smaller than the coherence length of the superconducting state. An important film quantity is the sheet resistance $R_\square = \rho \cdot d = R \cdot W/L$. With applied magnetic fields the film develops a highly insulating state $R_\square > 1\,\mathrm{M\Omega}$. This transition is called magnetic field induced superconductor-insulator transition (B-SIT).

The transition from the superconducting state into the insulating state can be tuned by disorder (D-SIT) too. In fact, the transition was first observed in Bismuth films [1]. Thick films go into a superconducting state and with decreasing thickness the critical temperature decreases until the film goes into an insulating state below a critical thickness without an intermediate metallic state. Moreover, the transition shows a critical sheet resistance at the quantum resistance for Cooper pairs $R_\square = \hbar/4e^2 = 6.5\,\mathrm{k\Omega}$: Above the critical sheet resistance the sample shows insulating behavior, below the critical resistance the sample is superconducting at low temperatures. In principle, superconductivity is robust against moderate non-magnetic disorder, shown by Anderson [2], and could survive in the insulating state. However, strong fluctuations in the superconducting gap can destroy the phase coherence even at finite gap. Therefore, it is possible that localized superconductivity exists within the insulating regime.

In experiments, several remarkable features of the insulating state were observed: A huge positive magneto-resistance [3–5] at low fields, a magnetoresistance peak at intermediate fields and a smooth decay at high fields [6–8], activated temperature dependence [9, 10] and jumps in the current-voltage characteristics [10, 11]. The observed characteristics were found in several materials, in particular amorphous indium oxide and titanium nitride, and appear to be an inherent property of the insulating state. Other systems with a SI transition are granular systems [12] and high T_c superconductors [13]. Common to all materials is their quasi 2D character and their weakened superconductivity compared to the bulk. The activated temperature dependence is very unusual. In disorder driven localization, hopping transport mechanisms, known for doped semiconductors, are expected. The current jumps can be explained by a decoupling of the electrons from the phonons [14, 15] which leads to an electronic state much hotter than the sample temperature, an interesting phenomenon by itself.

The mechanism for the superconductor-insulator transition in disordered films is still an open issue. Different competing theories [16–18] try to explain the nature of the insulating state. An overview can be found in the recent review [19]. Known from the concept of localization, with disorder more (elastic) scattering events occur and can lead to additional or enhanced quantum interference effects. From fermionic systems, i.e. electron systems, several mechanisms for localizations are already known which have their origin in quantum interferences, e.g. weak localization and Anderson localization. One key question is whether superconductivity is the driving force of this insulating behavior. With superconductivity, Cooper pairs are present, with bosonic wave functions influenced by disorder or charging effects. For unpaired electrons, there are materials, so-called Mott-insulators, where the on-site charging energy is too high for an additional electron. This phenomenon is called Coulomb blockade. A similar mechanism exists for Cooper pairs. Artificial Josephson junction arrays (JJA) consist of superconducting islands connected to each other with a tunnel barrier. When the islands are small enough, charging effects become important, similar to quantum dots in electronic systems. In these systems two competing energies exist, the Josephson coupling and the charging energy. If the Josephson coupling is dominant, the network will be superconducting. If the charging energy is dominant, the network is insulating. It was early suggested that this network theory could explain the superconductor-insulator transition, but a mechanism for the formation of superconducting islands in a homogeneously disordered film was lacking.

Numerical simulations [20–22] showed that phase fluctuations can destroy global superconductivity and with high enough disorder, superconducting puddles can emerge embedded in a state with a superconducting gap but without coherence peaks. Scanning tunnelling spectroscopy [23–25] of the BCS superconducting gap in titanium nitride, indium oxide and niobium nitride showed a spatially fluctuating gap and in addition a vanishing coherence peak. The vanishing coherence peak can be explained by localized Cooper pairs [24, 26]. These specific pairs should have a fractal wave function. In both theoretical approaches [22, 26] the concept is an on-site, Anderson-localization like, random potential. The result is a pairing energy that survives disorder longer than the coherence which is necessary for global superconductivity. Up to now both recent concepts are focusing on disorder, i.e. (D-SIT). Describing all experimental findings, in particular incorporating the magnetic field, is still an open task. Another assumption is that charging effects are small. Whether this is true or not has to be investigated further.

In the case of quasi 2D superconductors, Josephson junction arrays can be used as a numerical tool to simulate continuous films: Putting superconductivity on a lattice. Therefore, one can expect that a charge dominated network can be used to answer the questions whether the insulating state is dominated by the electron pairing energy or by the charging energy. Calculations on insulating Josephson junction array [17] could already be used to explain the non-monotonic magnetoresistance and the activated temperature dependence. Additionally the model could explain the logarithmic dependence of the activation energy on sample size, found in indium oxide [27]. At very low temperatures the insulating Josephson junction array undergoes a phase transition into a state where charges are frozen into dipoles. The mechanism of the melting is called charge Berezinskii Kosterlitz Thouless (BKT) transition. The frozen state was dubbed "superinsulator" [28].

The initial purpose of this thesis was to obtain high resolution $I(V)$ measurements of the insulating state which can tell the origin of the current jumps of high bias. During the subsequent investigations also low bias non-linearities in $I(V)$ are found. The low bias non-linearity is expected for a charge-BKT transition. Extensive simulations of the electron-phonon decoupling can reproduce the high bias-behavior of the isotherms and the onset of the current jumps. Furthermore, it can be excluded that a simple electron-overheating explains the low-bias non-linearities. The logarithmic dependence of the activation energy on the sample size in the insulating state is observed the first time in titanium nitride.

This thesis is organized as follows. In chapter 2 the relevant theoretical concepts are presented. Chapter 3 presents the sample properties and the measurement schemes. The influence of electron heating on the current-voltage characteristics and to which extent this phenomenon can explain the non-linearities in the conductance for the measured samples is displayed in chapter 4. Chapter 5 presents the main experimental results of this work. The current-voltage characteristics and the extracted resistance is analysed in the framework of the Josephson junction network model with respect to magnetic field and sample size. Low bias non-linearities are revealed which can be attributed to a charge BKT transition. For this low-bias non linearity was searched before, but not found. This is the first time where it is observed experimentally. Additionally, the duality of the charge-BKT and the vortex driven BKT transition and its similarity in the current-voltage characteristic is highlighted. The high magnetic field data show a saturation in the resistance at high fields and all sample sizes. Chapter 6 discusses the experimental findings. Chapter 7 summarises the obtained results.

Chapter 2

Overview of the Relevant Concepts

2.1 Superconductor-Insulator Transition

In this section the experimental observations of the superconductor insulator transitions are presented. It will be seen that the insulating state shows remarkable dependences with respect to magnetic fields, temperature and applied voltage. Additionally to the measured transport properties scanning tunnelling experiments are presented.

In 1989 Haviland et al. [1] showed that Bismuth films grown on Germanium develop a transition from a superconducting state into an insulating state. The temperature dependence of the resistance near the transition is presented in figure 2.1a. At high temperatures the sheet resistance $R_\Box = R \cdot W/L$, with W the width and L the length of the sample, is increasing with decreasing thickness. The dependence of the resistance on the thickness can be fitted and explained in a percolation model [29] $R(d) = R_0(d - d_c)^{-t}$ with $d_c = 4.08\,\text{Å}$ and the predicted exponent $t = 1.3$. The separatrix in the sheet resistance between the superconducting and the insulating state is very close to the quantum resistance of Cooper pairs $R_\Box = \hbar/4e^2 = 6.5\,\mathrm{k\Omega}$. However, Pb films produced in the same manner show a higher critical resistance [1].

In figure 2.1b the temperature dependence of the resistance near the superconductor insulator transition in titanium nitride films is presented (Taken from [10]). The room temperature resistance was increased by soft plasma etching. The room temperature sheet resistance is a good criterion for the low temperature behavior. The $R(T)$ curves in figure 2.1b do not cross. The sample with the lowest sheet resistance, S4, become superconducting at $\simeq 0.5\,\mathrm{K}$. With increasing sheet resistance, shown from $1\,\mathrm{K}$, the critical temperature decreases until the first sample, I1, shows an dramatic increase in the resistance at low temperatures and no superconductivity. This transition is very sharp and no intermediate metallic state was found up to now. The insulating behavior is increasing further with increasing sheet resistance. Note, that the superconducting state shows an upturn in resistance, up to $30\,\mathrm{k\Omega}$, before the superconducting state (see inset). The insulating state differs from the superconducting state by an activated temperature dependence [9, 10] at low temperatures, shown in figure 2.2a,b).

The term disorder is ambiguous. In fact, disorder can increase the critical temperature [30, 31]. These samples are produced in the same quenched condensate manner like the Bismuth [1] films shown above but without a Germanium layer underneath. The increase in the transition temperature is explained by an increase in the electron-phonon coupling and thus an increase in the attractive potential of the Cooper pair mediated by the phonons. However, common to all materials which exhibit a SI transition is their quasi 2D character. In this system "disorder" is referred to homogeneously disordered systems where the normal state resistance, far away from the superconducting state, is a good qualitative measure of this specific disorder. Apparently, the transition is not connected to crystal structure because the transition is found in amorphous (InOx), polycrystalline (TiN), granular (Pb grains) films, and high T_c superconducting materials.

Next, we focus on two material systems, indium oxide and titanium nitride. In general,

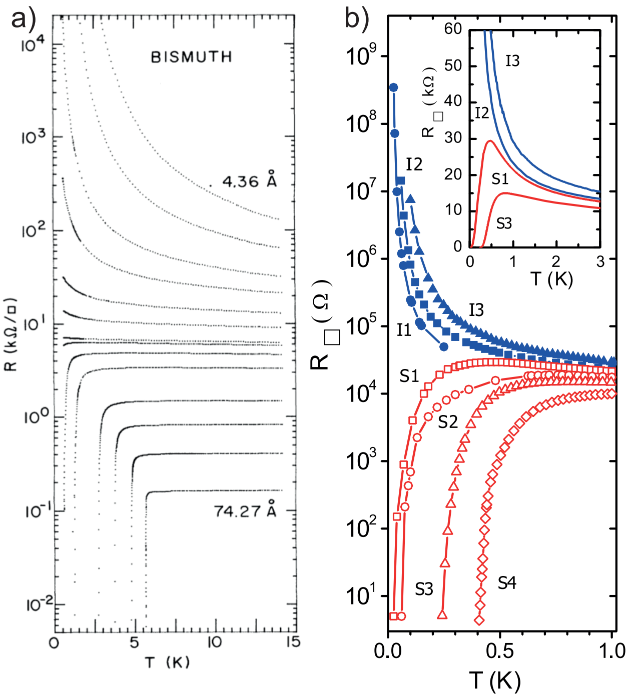

Figure 2.1: Disorder driven SIT: a) Evolution of $R(T)$ with respect to the thickness of Bismuth films deposited on Germanium. (Source [1]). b) $R(T)$ in titanium nitride films. The room temperature resistance was tuned by soft plasma etching. (Source [10]).

these two materials show similar features in the insulating state although the crystalline structure is amorphous in indium oxide and polycrystalline in titanium nitride. The similarity is displayed in figure 2.2. The indium oxide data is shown in the left column and the titanium nitride data in the right column. Figures a,b) show the activated temperature dependence of the resistance

$$R \propto \exp\left(T/T_0\right))$$

in both materials (Taken from [9, 10]). In b) the weak superconducting TiN film is driven into the insulating state by the magnetic field (B-SIT). The insulating state generated by the magnetic field shows no difference compared to the one generated by disorder. In c,d) the magnetic field evolution is shown (taken from [7, 10]). Both materials show a huge positive magnetoresistance at low fields up to a peak at $10\,\mathrm{T}$ in indium oxide and $5\,\mathrm{T}$ in titanium nitride. Above the peak the resistance decreases smoothly with increasing magnetic fields. The current-voltage characteristics is shown in e,f) (taken from [10, 11]). Here, the differential conductance is plotted against the applied voltage. At high temperatures the differential conductance increases with high-voltage bias. At low temperatures a jump in the current-voltage characteristics exists. Below the correspondent threshold voltage no resistance could be measured at this time. High resolution dc measurements revealed that the high bias increase and the jumps can be explained mostly by a decoupling of the electron temperature from the bath temperature [14, 15]. The high resolution dc measurements and the overheating analysis for titanium nitride are part of this thesis.

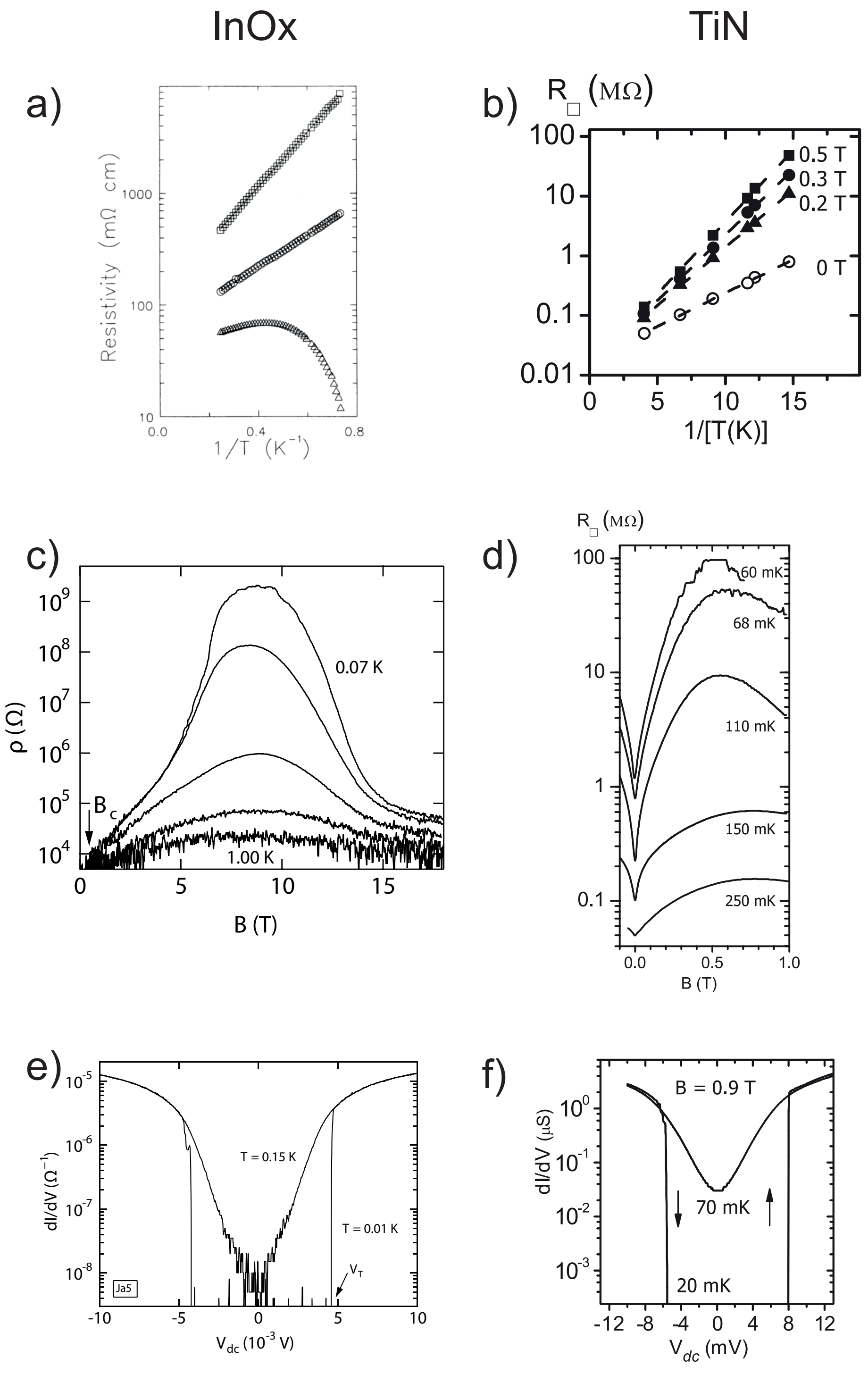

Figure 2.2: Overview of the experimental observations of the insulating state in the SI transition: a,b) Arrhenius activated behavior in the resistance; c,d) magnetoresistance peak with huge positive slope at low fields; e,f) jumps in current-voltage characteristics. (See text for references)

2.2 Superconductivity in Disordered Films

In this section the concepts of the superconducting state are presented. Additionally, the Ginzburg-Landau theory and the BCS-theory are introduced.

In general, the superconducting state can be characterized by the order parameter

$$\Phi(\vec{r}) = \Delta(\vec{r}) \exp\left(i\phi(\vec{r})\right) \tag{2.1}$$

with Δ the superconducting gap amplitude and ϕ the phase. If the phase has a spacial gradient, then a particle flow exists in the system. Since the particles are charges a current is created. The density of the number of superconducting particles is given by

$$n_s \quad = \quad |\Phi|^2 = \Delta^2 \quad . \tag{2.2}$$

The particle density n_s and the phase are conjugate variables and follow the uncertainty relation

$$\Delta n_s \Delta\phi \geq \hbar \quad . \tag{2.3}$$

There are two extreme cases. If the phase is fixed across the whole sample, i.e. $\Delta\phi \simeq 0$, the particles are delocalized and in a superconducting coherent state with zero resistance. If the particles are localized, the phase is fluctuating. The criterion for global superconductivity is that the correlator

$$G(\vec{r}) = \langle \Phi(\vec{r})\Phi(0) \rangle \tag{2.4}$$

remains finite at long distance. Three kinds of excitations can destroy the global superconducting order [25]:

- quasiparticle excitations (QE): primarily affect $|\Delta|$
- quantum phase fluctuations (QPF): number-phase uncertainty relation
- classical phase fluctuations (CPF): caused by thermal excitations

In conventional superconductors quasi-particle excitations are sufficient to consider. In disordered systems superconductors are characterized by poor screening of Coulomb interactions [32, 33] and small n_S. Strong enough phase fluctuations can destroy the superconducting order before the gap $|\Delta|$ goes to zero.

In the recent years scanning tunnelling microscopy (STM) enabled the direct measurement of the superconducting gap in disordered thin films. STM measurements have found a fluctuating gap in titanium nitride [23] and indium oxide films [24], presented in figure 2.3. Figure a) shows the gap energy in the two spacial directions in a superconducting TiN sample. It is seen that the gap is fluctuating and that there are puddles (red areas) where the gap is stronger than in the surrounding. In c) the normalized tunnel conductance of several titanium nitride films is shown. The curves are shifted for

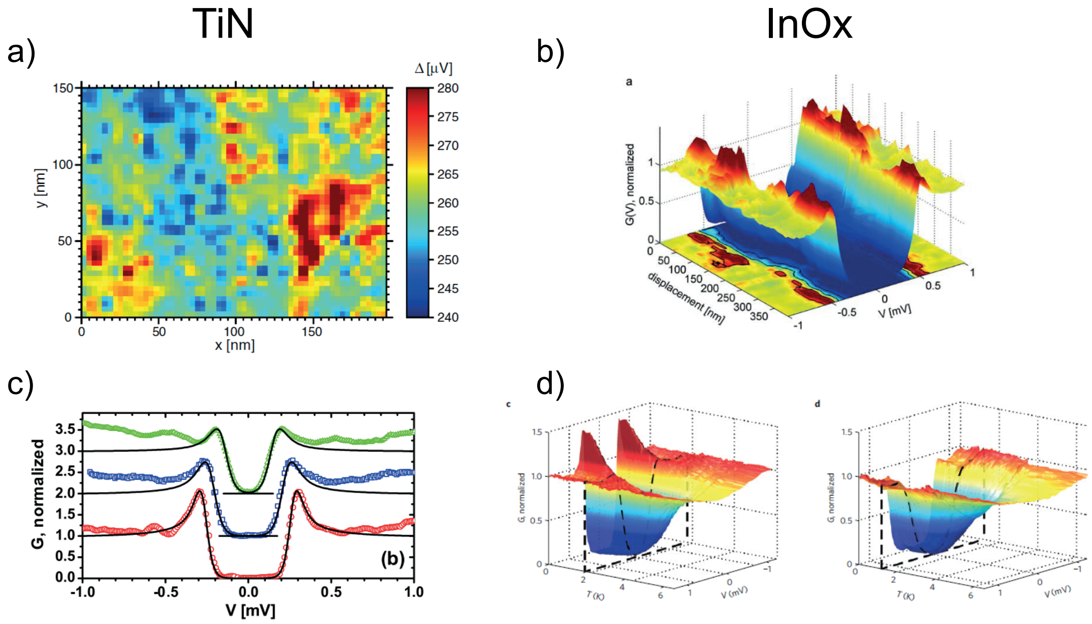

Figure 2.3: Scanning tunnelling measurements of TiN [a) and c)] and InO [b) and d)]: a) Spacial distribution of the gap Δ in TiN; b) spacial distribution of local density of states in InO; c) local density of states of three different TiN samples; d) temperature evolution of the local density of states in a low disorder sample (left) and a high disorder sample (right); Source [23, 24]

visibility. The red curve has the lowest sheet resistance at room temperature, the green curve the highest. Beside the gap the visible peaks are the coherence peaks of the superconducting state. With increasing disorder (higher resistance at room temperature) the peak is broadened. In b) the tunnel spectrum along one spacial direction in an indium oxide sample is shown. The peaks (red) besides the gap (blue region) are the coherence peaks of the superconducting state. There are regions where there is a finite gap but no coherence peak. Additionally, the gap, seen at the color plot at the bottom of the 3D plot, is varying in the spacial direction. In d) the temperature evolution of the local tunnelling conduction in indium oxide is shown. The left sub figure shows a spectrum with a coherence peak (low disorder sample) and the right sub figure shows no coherence peak (high disorder sample): The dashed line indicates the critical temperature T_c. Below T_c the coherence peak is emerging in the left figure which leads to a global superconducting state. In the right local tunnelling conductance a gap is emerging but no coherence peak is present. This kind of suppressed density of state was dubbed pseudo-gap.

In microscopic models the vanishing coherence peak is explained by a pairing potential that survives disorder longer than the coherence of the BCS state. Bouadim, Trivedi et al. [22] showed in Monte-Carlo simulation that, with high enough disorder, superconducting puddles can emerge embedded in a state with a superconducting gap but without coherence peaks.

2.2.1 Ginzburg-Landau Equation

The order parameter Φ can be treated in the Ginzburg-Landau (GL) model. The free energy is given by

$$F(\vec{r},T) \;=\; F_0+\alpha(T)|\Phi|^2+\frac{1}{2}\beta|\Phi|^4+\frac{1}{2m}|\left(-i\hbar\nabla-2e\vec{A}\right)\Phi|^2+\frac{1}{2\mu_0}B^2 \quad (2.5)$$

with $\alpha(T)=\alpha_1(T-T_c)$ close to the critical temperature T_c. If $\alpha<0$, there is a minimum of the free energy at the non-zero vacuum expectation value for Φ at

$$|\Phi|^2=\Delta^2=n_s=\frac{\alpha_1}{\beta}\left(T_c-T\right)\ . \quad (2.6)$$

Performing a Taylor expansion of the free energy 2.5 around the found minimum $|\Phi|$ yield a "mass" term for the vector field $\vec{A}$, the so called London penetration length

$$\lambda_L=\sqrt{\frac{m}{2e^2\mu_0 n_s}}\quad . \quad (2.7)$$

In thin films the penetration length in parallel magnetic fields is modified to

$$\lambda_{eff}\approx\lambda_L\left(\frac{\xi_0'}{d}\right)^{1/2}\quad , \quad (2.8)$$

where ξ_0' is the modified Pippard coherence and d the thickness of the film. In perpendicular fields the penetration length is given by

$$\lambda_\perp=\lambda_{eff}^2/d \quad (2.9)$$

Varying the free energy with respect to $\Phi^*+\delta\Phi^*$ yield the first Ginzburg-Landau equation

$$\alpha(T)\Phi+\beta|\Phi|^3++\frac{1}{2m}\left(-i\hbar\nabla-2e\vec{A}\right)^2\Phi=0\ . \quad (2.10)$$

The Ginzburg-Landau coherence length ξ can be interpreted as the shortest distance over which the wave function can vary without generating pair breaking

$$\xi=\sqrt{\frac{\hbar^2}{2m\alpha(T)}}\quad . \quad (2.11)$$

The value $\kappa=\lambda/\xi$ determines whether the material is a type-I ($\kappa<1/\sqrt{2}$)superconductor, without a vortex state, or type-II ($\kappa>1/\sqrt{2}$) with a vortex state. In type-II superconductors the value for destroying the vortex state is given by the maximum density of vortices. In this limit one flux quantum is trapped in minimal area of $2\pi\xi^2$. Therefore, the critical field is given by

$$B_{c2}=\frac{\phi_0}{2\pi\xi^2}\quad . \quad (2.12)$$

2.2.2 Bardeen-Cooper-Schrieffer Model

The superconducting state can be derived microscopically by the Bardeen-Cooper-Schrieffer (BCS) theory. The introduction here is taken from [34] and modified. In the simplest case (no disorder, no magnetic field, no boundary conditions) only singlet, zero-momentum states interact and scatter. These states can be described as

$$\begin{aligned} b_k &= c_{-k\downarrow} c_{k\uparrow} \\ b_k^\dagger &= c_{k\uparrow}^\dagger c_{-k\downarrow}^\dagger \quad , \end{aligned}$$

where $c_{k\uparrow}$ is the fermionic annihilation operator. The reduced Hamiltonian is given by

$$H = \sum_{k<k_f} 2|\epsilon_k| b_k b_k^\dagger + \sum_{k>k_f} 2|\epsilon_k| b_k^\dagger b_k + \sum_{k,q} V_{k,q} b_k^\dagger b_q \quad , \tag{2.13}$$

where k_f is the fermi momentum, $\epsilon_k = E - E_f$ the single-electron energy in respect to the Fermi energy, and $V_{k,q}$ the scattering matrix element between the pair states k and q.

The ground state of the superconductor is the linear combination of pairs $(k \uparrow, -k \downarrow)$ which are occupied (state O_k) of unoccupied (state $O_{(k)}$)

$$\psi = u_k O_{(k)} + v_k O_k \quad , \tag{2.14}$$

where v_k (u_k) is the probability amplitude to find a state occupied (unoccupied). The amplitudes are normalized such that $|u|^2 + |v|^2 = 1$. The phase of the Ground state can be chosen such that u_k is real:

$$u = \sqrt{1-h}; v = \sqrt{h} \exp(i\phi) \quad ,$$

with $0 \leq h \leq 1$. The phase ϕ is the same phase as in the order parameter. The complete BCS ansatz should include all k pairs and is given by

$$\psi_0 = \prod_k \left(u_k O_{(k)} + v_k O_k \right) \quad .$$

Minimizing the energy $\langle \psi_0 | H | \psi_0 \rangle$ with respect to the variational parameters h_k and v_k yield

$$h_k = \frac{1}{2} \left(1 - \frac{\epsilon_k}{E_k} \right) \quad , \tag{2.15}$$

with $\epsilon_k = E_e(k) - E_F$ the energy difference of a single electron from the Fermi energy and

$$E_k = \sqrt{\epsilon_k^2 + |\Delta(k)|^2} \quad . \tag{2.16}$$

The energy E_k is the single electron excitation energy. The complex value of Δ is determined by the famous self-consistent gap equation

$$\Delta(k) = -\frac{1}{2} \sum_q V_{k,q} \frac{\Delta(q)}{E_q} \quad . \tag{2.17}$$

The Cooper-pair size can be estimated by

$$\xi_0 = \frac{hv_F}{\pi|\Delta|} \quad , \tag{2.18}$$

where v_F is the Fermi velocity. The BCS theory connects the critical temperature with the gap

$$|\Delta| = 1.75 k_B T_c \quad . \tag{2.19}$$

2.3 Josephson Junction Array Model

In this section Josephson Junction arrays are introduced. The properties of the arrays are determined by two competing energies: The Josephson junction energy and the charging energy. It will be shown that there is a phase transition from superconducting arrays to insulating arrays determined whether the Josephson coupling is dominating or the charging energy. Interestingly, Cooper pairs are enhancing the charging energy and thus the insulating state. A conceptual phase diagram will be sketched for both low temperature states. An overview of Josephson junction arrays and their models can be found in Ref. [35].

The Josephson relations describe the dynamics of the junctions

$$\begin{aligned} V(t) &= \frac{\hbar}{2e}\frac{\partial \Delta\phi}{\partial t} & (2.20)\\ I(t) &= I_c \sin(\Delta\phi(t)) \quad , & (2.21) \end{aligned}$$

where $\Delta\phi(t)$ is the phase difference of the two superconductors, $V(t)$ and $I(t)$ is the voltage and the current across the junction. The Josephson energy is the accumulated potential energy in the junction. The energy accumulated across the junction is determined by the work over a certain time t

$$\begin{aligned} E &= \int_0^t V \cdot I dt' = I(t)\frac{\hbar}{2e}\frac{\partial \Delta\phi}{\partial t} \\ &= I_c \frac{\hbar}{2e}\int_0^{\Delta\phi(t)} \sin(\Delta\phi')d\Delta\phi' \\ &= I_c \frac{\Phi_0}{2\pi}\left[1-\cos(\Delta\phi)\right] \quad . \end{aligned}$$

The prefactor

$$E_J = I_c \frac{\Phi_0}{2\pi} \tag{2.22}$$

is called the Josephson junction energy and sets the characteristic energy scale of the junction. The energy will be optimized if the two phases are the same. Ambegaokar and Baratoff [36, 37] derived the relation between the Josephson energy and the superconducting gap

$$I_c R_n = \frac{\pi\Delta}{2e}\tanh\left(\frac{\Delta}{2k_B T}\right) \quad , \tag{2.23}$$

where R_n is the normal-state resistance of the tunnel junction and I_c the critical current of the tunnel junction. For $T = 0$ the critical current is given by $I_c = \frac{\pi\Delta(0)}{2eR_n}$.

The Josephson junction arrays consist of metallic islands coupled to each other with tunnel barriers. When cooled below the critical temperature T_c of the superconductor, the tunnel barrier forms a superconductor-insulator-superconductor (SIS) junction, a Josephson junction. As an example, a scanning electron micrograph of typical array is shown in figure 2.4 (From [38]). The islands are made of Al electrodes with a $\mathrm{Al_2O_3}$

tunnel barrier. The tunnel junction is the overlap of the base electrode (dark gray area) and the top electrode (lighter area). Thus, a SQUID geometry is formed, indicated by the red box. The result is an one dimensional chain of SQUIDs. The energy of a single Josephson junction is given by

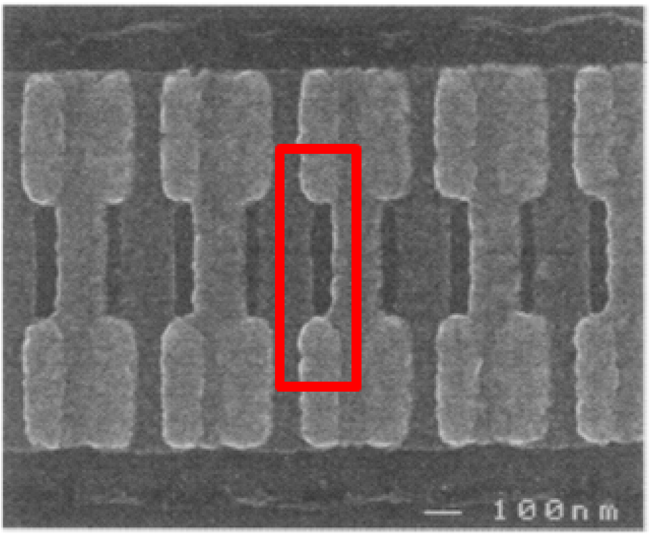

Figure 2.4: Scanning electron micrograph from Josephson junction array. The tunnel junctions are at the overlap between the base electrode (darker gray area) and the top electrode (lighter gray area). The red box indicates the SQUID geometry forming a 1D chain of SQUIDs. Source [38]

$$H = E_J\left[1 - \cos\left(\Delta\phi\right)\right] + E_C, \tag{2.24}$$

with E_J the Josephson energy and $\Delta\phi = \phi_1 - \phi_2$ the difference of the superconducting phase in both islands and E_C the charging energy of an island. When the dimensions of the islands is small, the capacitance is small and the charging energy

$$E_C \;=\; q^2/2C \tag{2.25}$$

is large and has to be taken into account. The schematics of a Josephson junction array is displayed in figure 2.5, taken from [28]. The green circles represent the superconducting islands and the crossed rectangles the Josephson coupled weak link between the islands. The energy of the array is given by

$$H = \frac{E_C}{2}\sum_{<i,j>} n_i n_j + \frac{E_J}{2}\sum_{<i,j>}\left[1 - \cos\left(\Delta\phi_{i,j}\right)\right] + \ldots, \tag{2.26}$$

with n_i the number of particles on island i and $\Delta\phi_{i,j} = \phi_i - \phi_j$. There are more terms in 2.26, including finite voltage and the lead electrodes [17] but, for the sake of

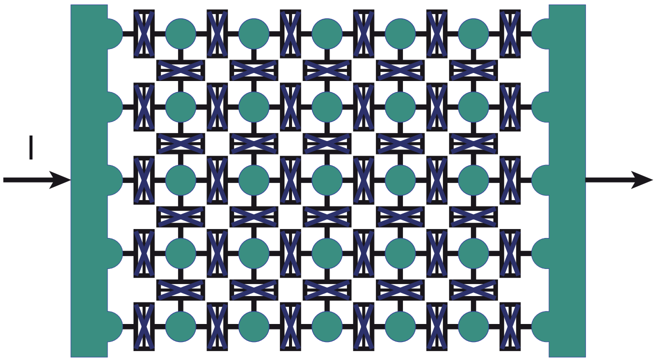

Figure 2.5: Schematics of a 2D Josephson junction array. The superconducting islands are indicated as green circles, the Josephson coupled weak link between the islands as crossed rectangles. Source [28]

clarity, omitted. First, the scenario $E_J \gg E_C$ is discussed. The second term in (2.26) resembles the classical Heisenberg XY-model, intentionally developed for ferro-magnets. A peculiar feature in 2D is that there is no phase transition accompanied by spontaneous symmetry breaking at $T > 0$ (Mermin-Wagner theorem). Instead the system undergoes a vortex driven Berezinskii Kosterlitz Thouless transition, explained in section 2.4: At low temperature there is a vortex anti-vortex lattice mediating superconductivity across the array. At high temperature there are free moving vortices contributing to a finite resistance. The resulting temperature dependence of the resistance shows a continuous transition into the superconducting state, compared to the sharp transition in the clean bulk.

When $E_C \gg E_J$ the system develops an insulating state at low temperatures. The total charging energy of one island is determined by the capacitance between two islands E_C and the capacitance to the ground E_{C0}. The case $E_C \gg E_{C0}$ is considered first. Astonishingly, Cooper pairs with the charge $q = 2e$ enhance the charging energy from $E_C = e^2/2C$ for electrons to $E_{CS} = 4e^2/2C$ and thus strengthen the insulating state. This effect can be seen in figure 2.6 taken from [39]. The conductance is plotted against the temperature. The superconductivity (S) is turned off by applying a finite magnetic field and the array returns in the normal state (N). At low temperatures the conductance is decreasing, i.e. the array becomes insulating for the superconducting array and the normal state array. However, the superconducting array shows a higher transition temperature into the insulating state than the normal one, which is due to the large charging energy of Cooper pairs.

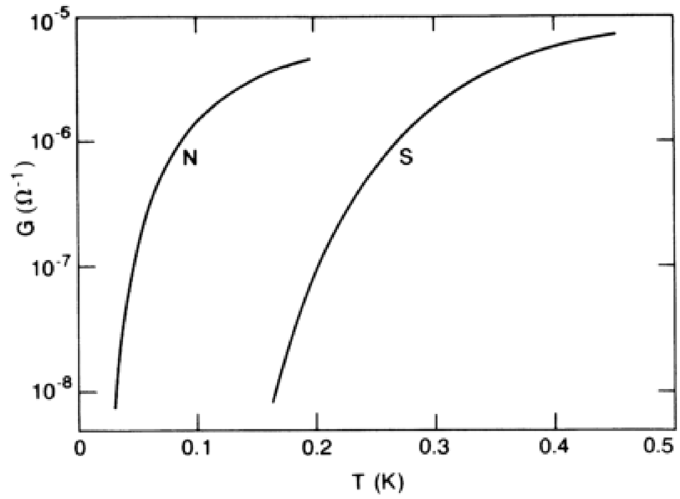

Figure 2.6: Conductance in the insulating state of artificial JJA. N is in the normal state (applied field 3 T) and S in the superconducting state. Source [39].

2.3.1 Charging Energy vs. Josephson Energy

With the vortex and the charge BKT mechanisms, the superconductor-insulator transition can be explained by a quantum phase transition [28, 39, 40], i.e. a change of a parameter in the Hamiltonian, and not the temperature, which leads to a change in the ground state. The phase diagram of the charge-unbinding and the vortex-unbinding in the superconducting array is shown in figure 2.7, taken from [40]. For ratios $E_J/E_C \ll 1$ the array undergoes a charge-BKT transition, with the low temperature insulating charge dipole phase. The transition temperature $T_{CS}^{(0)}$ is reduced by vortex interaction [40](Tunnelling of Cooper pairs), which become stronger with increasing E_J. Analogously, the vortex-unbinding transition temperature is reduced by charge interaction. The transition between the two low temperature phases occur at $E_J/E_C = a(2/\pi^2)$, with a larger but close to 1. Above the transition temperatures free charges or free vortices are present, which lead to dissipation and to a finite conductance and resistance, respectively. The transition between the free charges and free vortices above the transition temperatures was not well developed at this time and is still an open question.

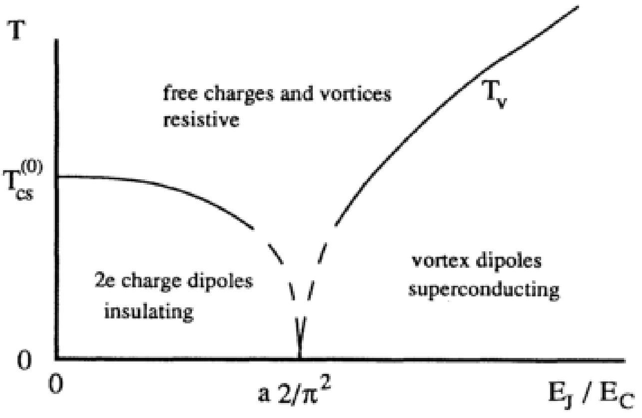

Figure 2.7: Phase diagram of the vortex-unbinding and charge-unbinding transition of a Josephson junction array. The two transitions meet at $T = 0$ at a value of $E_J/E_C = a2/\pi^2$ with a larger but close to 1. Source [40]

It was shown in calculations that in arrays on the insulating side above the transition temperature a collective charging energy Δ_C emerges [17]. The charging energy depends on the number of islands and the dimensions of the array. Taking into account the charging energy E_{C0} to ground the collective charging energy is given by

$$\Delta_C = \begin{cases} E_C \min\{\lambda_C, L\}/d & \text{1D} \\ E_C \ln \min\{\lambda_C, L\}/d & \text{2D} \end{cases}, \tag{2.27}$$

with E_C the charging energy between two islands and the screening length to the ground $\lambda_C = d\sqrt{E_{C0}/E_C}$. In the temperature range $E_C \leq k_B T \leq \Delta_C$ the temperature dependence of the resistance follows an activated behavior

$$R \propto \exp\left(\Delta_C/(2k_BT)\right) \quad . \tag{2.28}$$

First order perturbation theory of the charging energy with respect to E_J/E_C yield [17]

$$\Delta_c(B) \;=\; \Delta_c\left[1-\alpha E_J(B)/E_c\right] \quad , \tag{2.29}$$

where the parameter α is of the order of unity and depends on the geometry of the lattice. The Josephson junction magnetic field dependence can be calculated in a SQUID geometry, similar to the sample in figure 2.4. The field modulation of the Josephson coupling energy is given by [41]

$$E_J = \begin{cases} E_J|\cos(\pi f)| & \text{1D} \\ E_J\left\{1-4f\sin^2\left(\pi(1-f)/4\right)\right\} & \text{2D} \end{cases} \quad , \tag{2.30}$$

with $f = eBA_{loop}/\pi h$, A_{loop} the area of either the SQUID or the plaquette in the 2D array. In figure 2.8, taken from [17], the fits to experimental data with the derived formulas are shown. In 2.8a the length dependence of the activation energy, found in indium oxide [27], as a function of $\ln L$ is shown. The linear slope of the data (squares) is consistent with the predicted dependence for a 2D array from equation 2.27. Figure 2.8b shows the magnetic field dependence of the activation energy and the threshold voltage in the data from [10]. From the peak in the measured activation energy k_BT_0 (circles) the area $A_{loop} = 1.3 \cdot 10^{-3}\mu\text{m}^2$ can be determined. The activation energy is modeled in the 2D array. The value $\alpha E_J/C = 0.8$ is chosen to fit $T_0(B=0)$. The resulting fit (solid line) matches the data below the peak. At higher fields deviations occur. Also the periodicity in $E_J(B)$ is not found. The threshold voltage is approximately

$$eV_T \;\simeq\; \Delta_C \quad . \tag{2.31}$$

The threshold path is determined by the weakest link in 1D and therefore the charging energy in a 1D chain determines the threshold. Using the same A_{loop} and a modified different $\tilde{\alpha}E_J/E_C = 0.96$, due to different geometries, matches the measured threshold voltage (squares) below the threshold peak and slightly above.

In summary, the Josephson junction array model can reproduce the superconducting state as well as the insulating state in artificial arrays. Employing the JJA model to homogeneously disordered thin films can reproduce some of the observed properties of its insulating state: The Arrhenius activated behavior and its magnetic field and sample size dependence can be explained. Additionally, the threshold voltage can be reproduced as well.

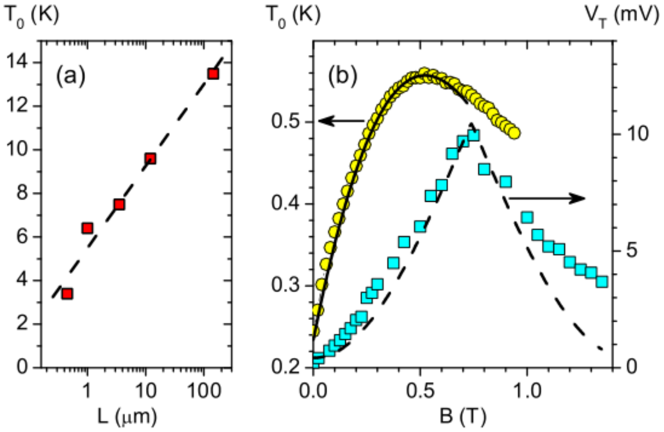

Figure 2.8: Josephson junction array model fits to measured data: (a) Activation energy extracted from [27] (squares) vs the sample size. (b) magnetic field dependence of the activation energy (circles) and the threshold voltage (squares) from [10]. The lines correspond to the fits within the Josepshon junction network model. Source [17]

2.4 Berezinskii-Kosterlitz-Thouless Transition

In 1972 Kosterlitz and Thouless [42] introduced a model for the phase transition from a liquid without long range order into a state with "topological" long range order. It was proposed for the XY-model and liquid Helium, and excluded for superconductors. Berezinskii already made similar considerations earlier. The model was refined and extended to thin superconducting films by Halperin and Nelson [43] and even further generalized by Young for arbitrary vector Coulomb gases [44].

In the XY-model in 2D, a conventional second order phase transition is not expected because of the Mermin-Wagner theorem: Continuous symmetries cannot undergo spontaneous symmetry breaking at finite temperatures in systems with sufficiently short-range interaction and system dimensions $d \leq 2$. This is because if a spontaneous symmetry breaking occurs, the corresponding Goldstone-boson will show a logarithmic infra-red divergence in the correlator. The destruction of the long range order can be intuitively understood that long range fluctuations can be created with little energy costs and since they increase the entropy they are favored and thus destroy the long range order.

So how is a long range order still possible? Consider the lattice sites as small vectors rotating in the plane of the lattice which, for simplicity, is a simple square lattice with spacing a. The Hamiltonian of the XY-model is given by

$$H = -J \sum_{\langle i,j \rangle} \vec{S}_i \cdot \vec{S}_j = -J \sum_{\langle i,j \rangle} \cos\left(\phi_i - \phi_j\right) \tag{2.32}$$

where $J > 0$ and the sum $\langle i, j \rangle$ over lattice sites is over nearest neighbours only. We will see later, that this Hamiltonian is much more general and can be applied not only to spin systems but also to Josephson junction arrays. To minimize the energy one would expect that all vectors would be parallel to each other but this, as already mentioned, is forbidden due to the Mermin-Wagner theorem. Nevertheless, one can generate a quasi-long range order by vortices. These topological objects are stable in time and do not decay because changing a single vector of the vortex would increase the total energy. For a single vortex the energy is given by

$$E_{Vortex} = J \ln\left(R/a\right), \tag{2.33}$$

where R is the size of the system and a the lattice spacing. The number of possible core locations is proportional to (R/a) and therefore the entropy is

$$S = 2k_B \ln\left(R/a\right) + O(1). \tag{2.34}$$

Thus, the free energy is given by

$$F = E - TS = \left(J - 2k_B T\right) \ln\left(R/a\right) \ . \tag{2.35}$$

At the temperature $T_{BKT} = J/2k_B$ the sign of the free energy is changing: At the free energy is $F > 0$, below T_{BKT}, a vortex is not favored thermodynamically. At $F < 0$, above T_{BKT}, a vortex is thermodynamically favored and can be excited.

2.4.1 Vortex-BKT

Now we focus on thin, quasi 2D, superconducting films. Since a superconductor is a charged super-fluid, one vortex would create a finite magnetic field and therefore not allowed as an excitation at zero magnetic field. The solution for this problem is a vortex-antivortex pair [43]. This object would not have any visible total magnetic field. The force between two vortices, obtained by Pearl [45], is given by

$$\begin{aligned} \frac{dU}{dr} &= \frac{\pi}{2}\frac{n_s\hbar^2}{m}\frac{1}{r}, r \ll L_s, && (2.36) \\ &= \frac{\pi}{2}\frac{n_s\hbar^2}{m}\frac{L_s}{r}, r \gg L_s, && (2.37) \end{aligned}$$

where L_s is the magnetic "screening length"

$$\begin{aligned} L_s &= \frac{mc^2}{2\pi n_s e^2} && (2.38) \\ &= 2\frac{\lambda_L^2}{d}, && (2.39) \end{aligned}$$

where λ_L is the bulk London penetration length and d is the film thickness. Therefore, for a sufficient thin film, the screening length L_s can exceed the sample size. Ignoring the area $r > L_s$ one finds the relation [46]

$$k_B T_c = \frac{1}{8}\pi n_s \hbar^2/m = c^2\hbar^2/16e^2 L_s, \tag{2.40}$$

where n_s is the number of electrons in the superconducting state per unit area. The transition separates a phase with bound vortex anti-vortex pairs ($T < T_{BKT}$) and a phase with free vortices ($T > T_{BKT}$). Free moving vortices will contribute to the resistance with

$$\sigma_s = \frac{e^2}{\hbar^2\pi^2}\frac{1}{n_f\mu},$$

where n_f is the number of free vortices and μ the vortex mobility $\mu = 2\pi\xi_0^2 c^2 \rho_n/\phi_0^2$, ξ_0 is the vortex lattice spacing. The important part in 2.41 is the number of vortices. It can be rewritten as $2\pi n_f = 1/\xi^2$ with ξ the correlation length. When $T \to T_{BKT}$ the correlation length is dominated by BKT fluctuations and follows $\xi \sim \exp(b/\sqrt{t})$ with the reduced temperature $t \equiv (T - T_{BKT})/T_{BKT}$. However, this region can be influenced by Ginzurg-Landau fluctuations which complicates the analysis. Qualitatively, the resistance is dominated by the number of free vortices. At temperature above T_{BKT} there are thermally excited free vortices. Below T_{BKT} the vortices are frozen and are bound and do not contribute anymore to the conduction. Besides the temperature a finite current can separate a vortex anti-vortex pair due to the opposite vorticity. In general, the $V(I)$ characteristic near T_{BKT} is given by

$$V \propto I^{1-\pi J_s(T)/T} = I^{\alpha(T)}, \tag{2.41}$$

where J_s is the superfluid density. Just below T_{BKT} the number of free vortices at finite current is proportional to $\pi J_s(T_{BKT})/T_{BKT} = 2$ which leads to $V \propto I^3$. In the thermodynamic limit, the superfuild densitiy should jump to zero above T_{BKT}, however, in a real system finite-size effects and inhomogeneity are producing a smooth downturn of J_s [47, 48].

As an example, $R(T)$ and $V(I)$ in the crossover region are presented in figure 2.9 (source [49]). The sample consists of proximity coupled Pb-Sn junctions. The 100 nm thick tin was deposited on 10^6 planar Pb discs arranged on a triangular lattice. The temperature is in the region where the lead is already superconducting but the tin is still in the normal state. In the upper graph we see the resistance plotted logarithmically against $t = \sqrt{T_{BKT}/(T - T_{BKT})}$. The resistance shows the predicted linear dependence on t. In the $V(I)$, shown in the lower graph, we see at high temperatures linear current-voltage characteristics. With decreasing temperature the $V(I)$ acquires a non-linear term which is superimposed upon the linear term. When reaching T_{BKT} the linear term vanished and the $V(I)$ follows a simple power law $V \propto I^3$. Below T_{BKT} the exponent in the current increases further.

In many experiments [48], it was found that the temperature dependence of the resistance can be influenced by fluctuations and excitations, for instance thermal activated single vortices [50] which leads to an exponential decrease of the resistance. However, the non-linear resistance can be viewed as a fingerprint of the BKT-transition.

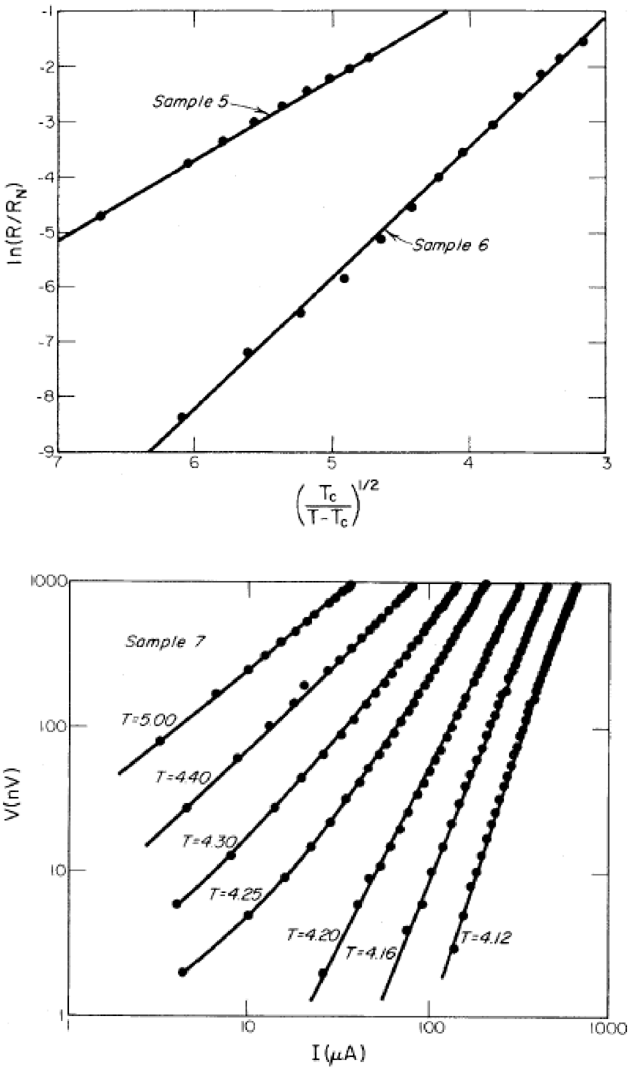

Figure 2.9: Pb-Sn junctions at temperatures where the lead is superconducting but not tin producing a proximity coupled Josephson junction network. *upper:* Logarithmic plot of the resistance vs the reduced temperature $t \equiv T_{BKT}/(T-T_{BKT})$. *lower:* Logarithmic plot of the voltage-current characteristic. At high temperatures the $V(I)$ is almost linear while at T_{BKT} $V \propto I^3$. Source [49]

2.4.2 Charge-BKT

Introduced for Josephson junction arrays [39, 40] the charge-BKT transition is based on the idea of a logarithmic Coulomb interaction. In a pure 2D system, this condition is fulfilled and, following the mechanism of the BKT transition, leads to a phase with bound charge anti-charge pairs and a phase with free charges. In figure 2.10 the schematic distribution of a charge anti-charge pair in a Josephson junction array is shown. The array consists of superconducting island coupled to each other via tunnel junctions. Two islands, separated by the distance d, are containing a net charge of opposite sign. The neighbouring islands are polarized by the pair but not contain any net charge. The potential, solved in a quasi-continuous approximation, is given by [39]

$$\phi(r) = \alpha K_0(r/\lambda_C), \tag{2.42}$$

with the screening length $\lambda_C = d(C/C_0)^{1/2}$, where C_0 is the capacity to the ground from the islands and C the capacity of the tunnel junction and K_0 the modified Bessel function. For $r \gg \lambda_C$ the Bessel function drops off exponentially. For $r \ll \lambda_C$ the potential is $\phi(r) = -\ln(r/\lambda_C)$ and again the BKT-mechanism can be used and yield a transition temperature of

$$k_B T_{BKT} \;=\; E_C/4\pi\epsilon_c,$$

with ϵ_c a non-universal constant slightly larger than one [39]. In the superconducting state the charge is $2e$ and the transition temperature $k_B T_{BKT} = E_C/\pi\epsilon_c$. Above T_{BKT} the number of free charges is given by

$$n_c \;=\; \exp\left(-2b/(T/T_{BKT}-1)^{1/2}\right) \tag{2.43}$$

which has a structure similar to the number of free vortices in the vortex BKT transition. Below T_{BKT} the charges are frozen and the array is insulating. Applying a finite voltage across the array can break apart dipoles resulting in a non-linear conductance [40]

$$I \;\propto\; V^{\alpha(T)}. \tag{2.44}$$

The exponent α is one above T_{BKT} and shows a universal jump at T_{BKT} to three. This current-voltage characteristics displays the duality of the vortex and charge BKT, meaning that replacing current and voltage and resistance with conductance will lead to very similar observables.

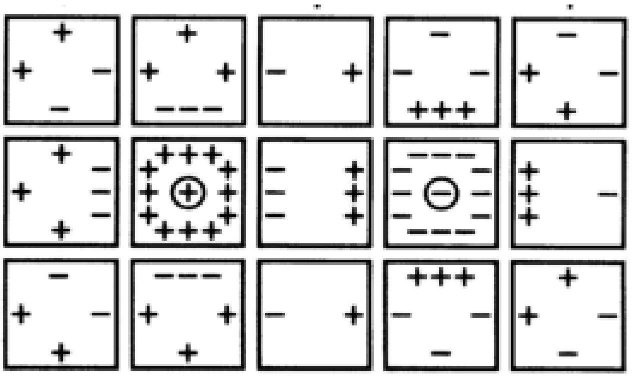

Figure 2.10: Schematic distribution of a charge anti-charge pair in a Josephson junction array. The neighbourhood of the actual charge is polarized but do not contain a net charge. Source [39]

2.5 Electron-Phonon-Decoupling

A consistent description of threshold behavior requires the consideration of heating instabilities which usually accompany a dielectric breakdown. Analyzing the I-V characteristics of an amorphous InO film in the field-tuned insulating state at the magnetic field slightly exceeding the upper critical field, B_{c2}, Ovadia and collaborators [14] showed that they are consistent with an overheating of the electron system above the lattice temperature. A similar $I-V$ characteristics was observed before, e.g., in YSi [51] which does not show any superconducting behavior. Importantly, the treatment of [14], explained in detail in [52], was based solely on the experimentally determined temperature dependence of the resistance (depending on the electron temperature) and the electron-phonon relaxation rate, and did not contain any information or specifics about the superconductivity-related nature of the high resistive state and the magnetic field effects. In this section, we will provide a comprehensive guide sufficient to do a self-consistent analysis of experimental data.

Several assumptions are made:

- The electron-electron (e-e) interaction is strong enough for electrons being mutually thermalized; i.e., one can introduce their temperature T_{el} although the system is driven out of equilibrium by a finite voltage;
- The electron-phonon interaction is weak so that electrons can be out of equilibrium with the phonon bath of temperature T_{ph}, i.e., $T_{el} > T_{ph}$;
- $R(T)$ dependence at a finite voltage is the same as in the Ohmic regime but $T_{el}(V)$ is substituted for T;

The starting point is a general heat balance equation

$$\frac{V^2}{R(T_{el})} = I_E^{out} - I_E^{in}, \tag{2.45}$$

where $R(T_{el})$ is the sample resistance which depends only on the electron temperature, I_E^{out} is the energy flow between the charge current carriers (electrons) and the phonon bath and I_E^{in} is the back flow from the phonon bath to the charge carriers. Thus, the right-hand side of equation 2.45 is merely the total power that the electronic system loses to the phonon bath:

$$P = \Gamma\Omega(T_{el}^{\beta} - T_{ph}^{\beta}) \quad , \tag{2.46}$$

where T_{ph} is the phonon temperature, Γ the electron-phonon relaxation rate, Ω the volume of the sample, $\beta = n + 2$, where n is the power describing the temperature dependence of the electron-phonon relaxation rate: $\tau_{e-ph}^{-1} \propto T^n$. The value $n = 3$ was first calculated in and found in most metals. The value $n = 4$ was calculated in for very disordered conductors. Following the self-consistent procedure described in [14] and will be explained in the following we will find exponents $\beta \approx 6$ which are close this disordered conductor scenario. Using equation 2.46 in 2.45 yields an equation applicable to electronic systems:

$$\frac{V^2}{R(T_{el})} = \Gamma\Omega(T_{el}^{\beta} - T_{ph}^{\beta}), \tag{2.47}$$

with the two parameters $\Gamma\Omega$ and β. Next, we have to extract the specific electron temperature for the applied voltage bias in the $I-V$, $I(V) \rightarrow T_{el}(V)$. Therefore, we invert $R(T) \rightarrow T(R)$ in order to get a measure for the electron temperature. With this relation and using $R_{loc} = V_{loc}/I_{loc}$ locally we obtain a $T_{el}(V)$. In Figure 2.11 the T_{el} transformation of the $I-V$ from [14] is shown. The sample is amorphous InO which is superconducting in zero field. The magnetoresistance peak is at $B = 8$ T. The shown data is measured above it. For isotherms below 100 mK, discontinuities in I of up to 5 orders of magnitude are observed. There are two jumps in each isotherms which show hysteric behavior. We denote by V_{LH} the transition from the low resistive (LR) state to the high resistive (HR) state and from HR to LR by V_{HL}, respectively. When using the explained transformation we see the discontinuity exists in $T_{el}(V)$ too. This is guaranteed by the used method since $R(T)$ is a continuous function.

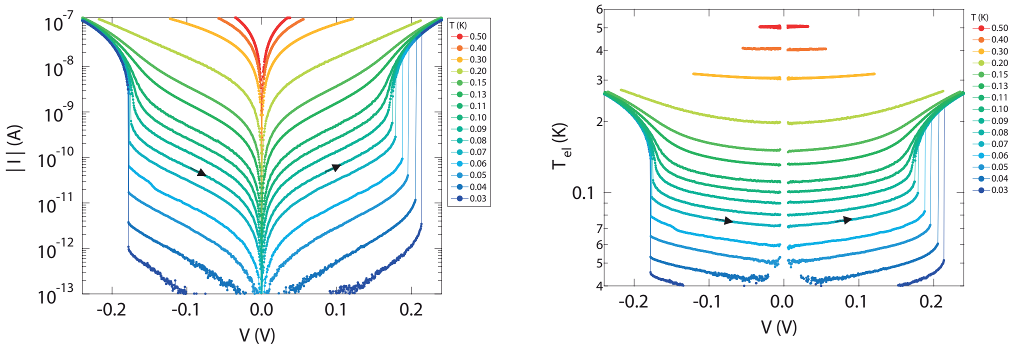

Figure 2.11: *left*: $I-V$ isotherms measured on the magnetic field-tuned insulator at $B = 11$ T. The voltage is swept from -0.25 to 0.25 V, indicated by the arrows on one of the curves.
right: T_{el} vs V, extracted from the $I-V$ curve and calibrated using the measured $R(T)$ at $V = 0$. The sweep direction is indicated by the arrows. Points near $V = 0$ have been omitted due to the large relative noise in I which causes excessive errors in the calculation of T_{el}. Pictures taken from [14]

Now, the parameters $\Gamma\Omega$ and β can be determined: Above the threshold voltage the electrons are decoupled from the phonon bath and therefore the total heating power is absorbed by the electrons, whereas the phonon cooling remains constant. Thus, for sufficient high bias, equation 2.46 yields

$$I \cdot V = \Gamma\Omega T_{el}^{\beta}, \tag{2.48}$$

and we can extract β from the data fit. This can be seen in figure 2.12. The inset shows the power plotted versus T_{el} in log-log scale for $T = 0.05$ K. We see that the power yield $P \propto T_{el}^{\beta}$ with $\beta = 6$, asymptotically. For low power T_{el} goes to $T_{el} = T_{ph} = T$ due to the gauge of T_{el}. By adjusting the parameter $\Gamma\Omega$ Ovadia and collaborateurs can obtain

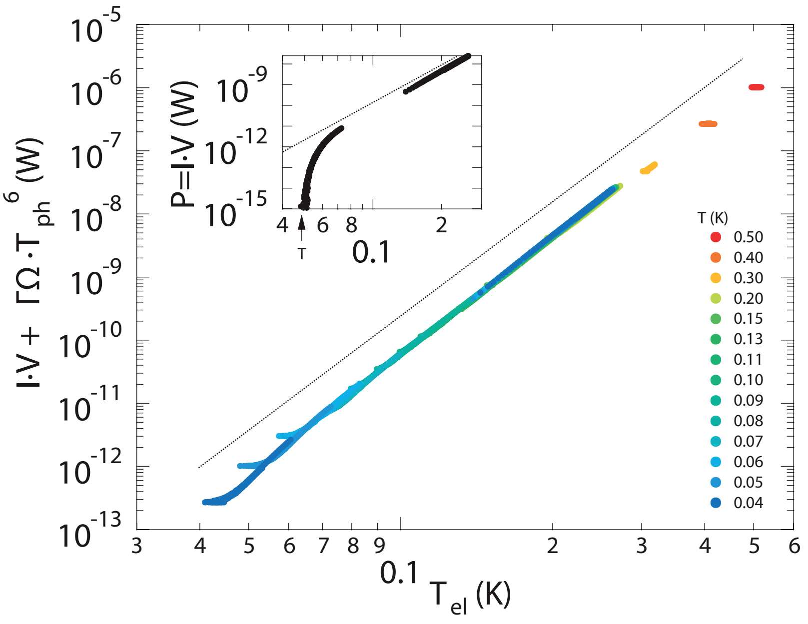

Figure 2.12: Plot of $IV + \Gamma\Omega T_{ph}^{\beta}$ versus T_{el}. A single adjustable parameter $\Gamma\Omega$ is used for all T_{ph}, and a dotted line with slope 6 is plotted alongside the data for comparison (shifted for clarity). [inset] Plot of $P = IV$ versus T_{el} for $T = 0.05$. At high P, $P \propto T_{el}^{\beta}$ (dotted line has slope 6 for comparison) Pictures taken from [14]

a collapse of the entire data onto a single power-law curve in log-log scale with slope $\beta = 6$ which can be seen in figure 2.12. The obtained $\beta = 6$ was also calculated for very disordered systems and the determined Γ measured also in a heavily doped silicon on insulator film [53] with Γ in the same range of values and $\beta = 6$.

Chapter 3

Materials and Methods

3.1 Sample Properties

Two samples are investigated made from the same TiN film. The film is approximately $5\,\mathrm{nm}$ thick grown on a $10\,\mathrm{nm}$ thick silicon dioxide layer on a silicon wafer. A transmission electron microscope micrograph of the TiN film can be seen in figure 3.1. The micrograph was taken by Gutakovskii and Latyshev, Novosibirsk. The black bar corresponds to $10\,\mathrm{nm}$. It is seen that the film is polycrystalline with a typical grain size of $5\,\mathrm{nm}$. The carrier density is roughly $n \approx 2\text{-}4 \cdot 10^{22}$. The untreated wafer is superconducting with a coherence length $\xi_d = 9\,\mathrm{nm}$.

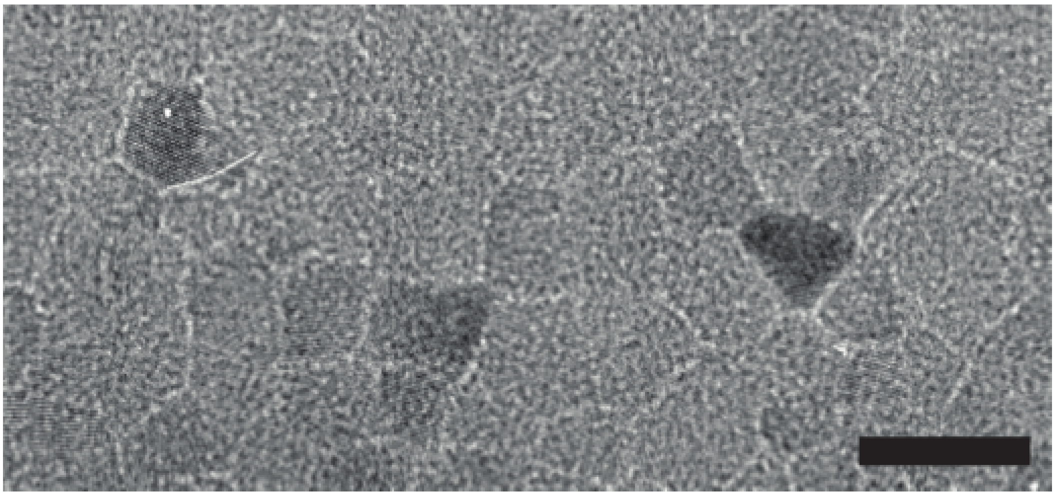

Figure 3.1: Transmission electron microscope micrograph of TiN film performed by Gutakovskii and Latyshev, Novosibirsk. The scale bar corresponds to $10\,\mathrm{nm}$. Published in [54]

In figure 3.2 an optical microscope picture of sample S is shown. The sample is patterned into a Hall bar by UV lithography and subsequent plasma etching through the TiN film by Baturina et al. [10]. The red area indicates the current path across the sample. The blue area indicates the voltage probe leads of the four-point current bias setup. The width of the current path is $50\,\mathrm{\mu m}$ and the maximum length between the voltage probes is $450\,\mathrm{\mu m}$ resulting in nine squares sheet resistance in series. When measuring two-point between the current leads one measures 26 squares in series. The contacts to the chip carrier is realized by soldering silver wires with indium onto the TiN contact pad and to the chip carrier. The resulting contact shows a good electric contact and is very robust against thermal and mechanical stress and easy to repair. Employing controlled oxidation in air at $\simeq 270°C$ sample S was pushed very close to superconductor-insulator transition. The sheet resistance at room temperature is $4.26\ \mathrm{k\Omega}$. Sample S also allowed a fine tuning into the insulating state by applying a small magnetic field.

Sample I has the purpose to investigate the size dependence of the superconductor-insulator transition in thin TiN films. The challenge for size dependent measurements

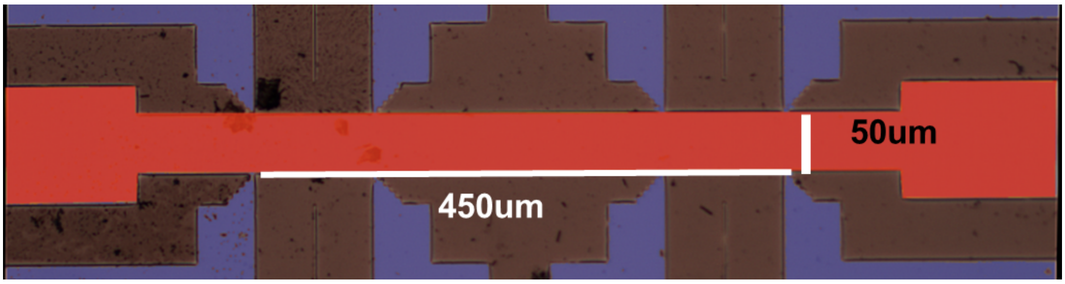

Figure 3.2: Optical microscope picture of sample S: The Hall bar is defined by plasma etching through the TiN film. The red area indicates the current path across the sample. The blue area indicates the voltage probe leads. Sample patterened by Baturina et al. in Novosibirsk

is that the material in all sizes should be the same. Additionally, the steep temperature dependence of the resistance demands a very stable and reproducible temperature. To avoid these problems, several square shaped samples were patterned by electron beam lithography on a single chip. The final design and the sample is made by myself in the clean room facilities at Prof. Weiss chair at the University of Regensburg. Figure 3.3 shows an optical picture of the whole chip (a) and the square sizes $5\,\mu\mathrm{m}$ (b) and $240\,\mu\mathrm{m}$ (c) of sample I. The patterned sizes are $0.5, 1, 2, 5, 10, 20, 60, 120, 240$ and $500\,\mu\mathrm{m}$. The width to length ratio is kept for each size 1:1. Thus, the sample is more suitable for measuring high resistive state than sample S at the same sheet resistance. Additionally, the sheet resistance is the measured total resistance which makes analysis more convenient. The squares are aligned such that the access for the bonding wires is maximized and easy, i.e. without crossing bonding wires. The length of the samples is defined by broad gold contacts $100\,\mathrm{nm}$ thick with a $5\,\mathrm{nm}$ titanium adhesion layer [golden area in a) and b)] and the width is defined by a trench etched with directed argon plasma [light gray area in b) and c)]. The gold contacts are narrowing from the pad to the actual sample, when the sample size is much smaller than the bonding pad. The gold contact is at the end slightly broader than the desired width but the distance between the contacts are designed to be exact at the desired distance. Thus, there is a larger alignment tolerance for the etching which overlaps with the excess gold contact. With this setup, it is possible to measure several samples simultaneously, at the same fields and temperatures.

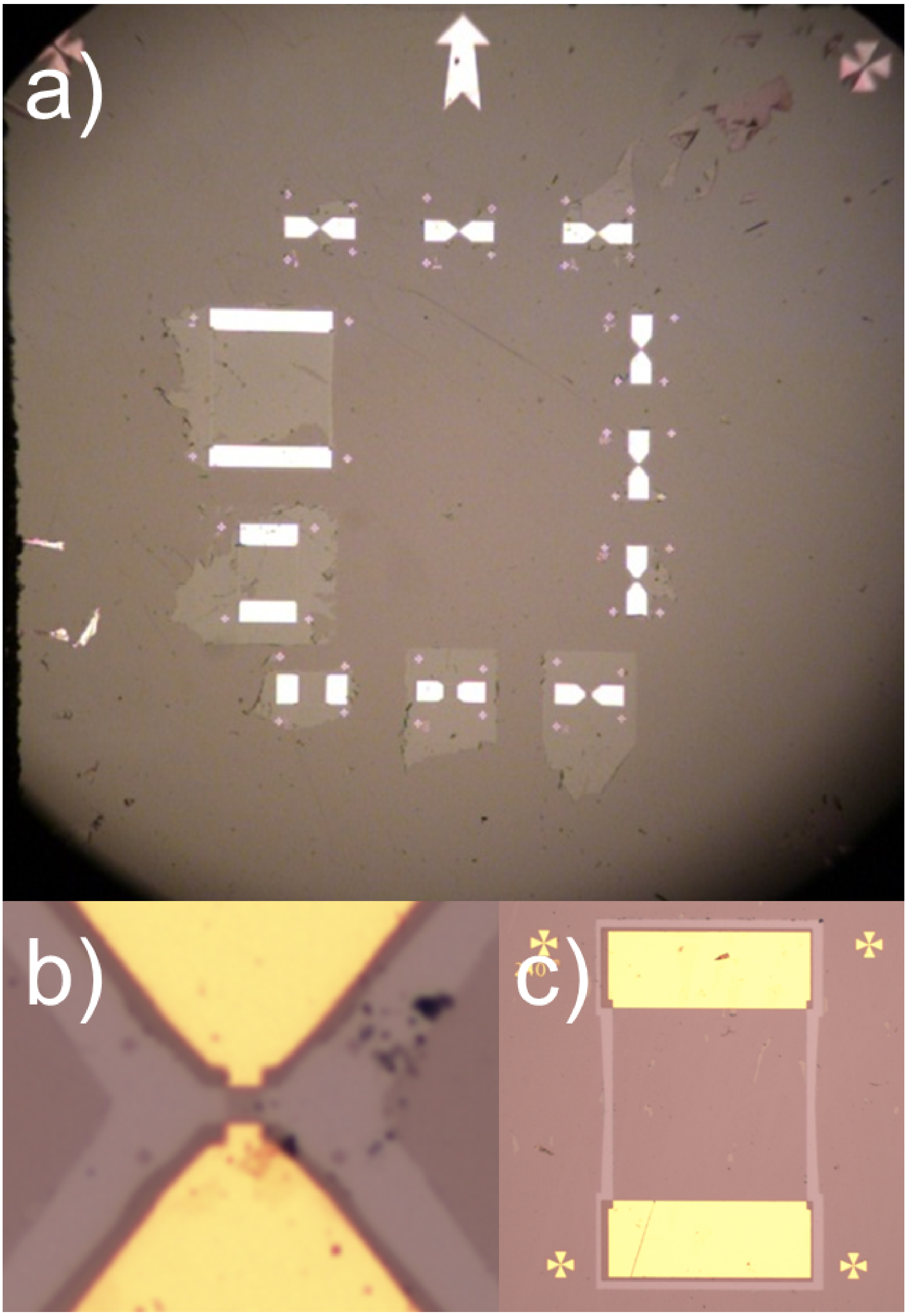

Figure 3.3: Optical microscope picture of sample I: a) picture of the whole chip. The patterned sizes are 0.5, 1, 2, 5, 10, 20, 60, 120, 240 and 500 µm. b) and c) Closer pictures of the sample 5 µm and 240 µm. The length of each sample is defined by gold contacts (golden area) and the width is defined by etched trench (light gray area). Chip patterned at the University of Regensburg by D. Kalok

3.2 Measurement Setup

When measuring near the superconductor-insulator transition, i.e. the transition between a low resistive, even "zero" resistance, state and a high resistive state one has to be vigilant about the used setup. Using the wrong measurement scheme can lead to astonishing but wrong results. For instance, the sample is superconducting and henceforth has zero resistance below a critical current and therefore no voltage drop across the sample. However, if we use a measurement setup which fixes a voltage we will measure the current that is needed to produce this voltage drop and therefore the current is above the critical current. Hence, we would never see the superconducting region, especially, if the voltage sweep is too rough or the current is measured in an ac setup. In general, a too steep function in $I(V)$ and $V(I)$, respectively, is hard to measure and it is better to change from $I(V)$ to $V(I)$ and vice versa. Additionally, when measuring at temperatures below 100 mK one has to take into account the Joule power heating originated from applied currents or voltages. For a fixed current the Joule power is

$$P_{Joule} = R \cdot I^2 \tag{3.1}$$

and for a fixed voltage

$$P_{Joule} = \frac{V^2}{R}. \tag{3.2}$$

As a rule of thumb, the power below 100 mK should not exceed 1 pW. Therefore, for a sample with a low resistance a current bias setup minimize the Joule heating and for a high resistance sample a voltage bias setup is optimal.

3.2.1 Low Resistance - Current Bias

When searching for a weak superconducting state one has to take precautions not destroying superconductivity by the measurement. First, consider Johnson-Nyquist noise [55, 56] (thermal noise). The voltage variance (power spectral density) per Hertz bandwidth is given by $\bar{v}_n^2 = 4k_BTR$. This can be rewritten as root mean square of the voltage as

$$v_n = \sqrt{4k_BTR\Delta f}, \tag{3.3}$$

where Δf is the bandwidth. The resulting current noise is obtained by simply dividing v_n by the resistance

$$i_n = \sqrt{\frac{4k_BT\Delta f}{R}}. \tag{3.4}$$

It is important to know that thermal noise is intrinsic to all resistors and is not a consequence of a bad setup. However, a bad setup can add additional noise on top of it. As a rule of thumb a $50\,\Omega$ resistor at $1\,\mathrm{Hz}$ bandwidth has a voltage noise of $1\,\mathrm{nV}$

at room temperature, i.e. a current noise of $0.02\,\mathrm{nA}$. The found critical current of sample S is of the order of $10\,\mathrm{nA}$. Therefore, a bandwidth above $1\,\mathrm{kHz}$ can destroy the superconducting state. This can be avoided by additional filtering (dampening the high frequencies) of the lines and higher resistive lines. In a four point contact setup, i.e. two contacts for the current and two contacts measuring the voltage drop, the lines of the voltage measurements can be high resistive because no current is flowing through these lines. The standard lines have a cut-off frequency of $500\,\mathrm{MHz}$ due to room temperature pi-filters and low temperature cooper-powder filters. In the used setup an additional low-pass filters at the mixing chamber temperature are used in series with a resistance of $2\,\mathrm{k}\Omega$. Thus the incoming current noise from room temperature is reduced to $i_{300} = \sqrt{4k_BTR_{300}/R_G\Delta f}$. Hence, the current noise is reduced significantly due to the series resistance and additionally due to the lower cut-off frequency of the low-pass filter.

The setup for the low resistive/superconducting state, used for sample S (see chapter 5), can be seen in figure 3.4. The setup is a 4-point current bias setup where $V(I)$ and dV/dI is measured simultaneously. The sample is placed in a dilution system with a base temperature of 25 mK electromagnetic shielded with a grounded copper box. All feed-throughs have a pi-filter rf filtering. The dc-current is defined by an external voltage source and a series resistor. The additional ac-current, used by the lock-in, is superimposed by the SR830 internal ac-source and an additional series resistor. The series resistors are connected directly to the cryostat. The other end of the line is terminated at room temperature with a ground cap. The voltage drop across the sample is amplified by an NF LI-75A low noise differential pre-amplifier (Fixed gain x100) which is placed inside the copper box. Measuring the superconducting state directly with a multimeter were not successful because the additional noise destroyed the weak superconducting state. The amplified dc signal is separated from the ac signal by an SR560 pre-amplifier outside the copper box and measured by an Agilent 3458A multimeter. The ac voltage signal is measured after the pre-amplifier by the SR830 lock-in.

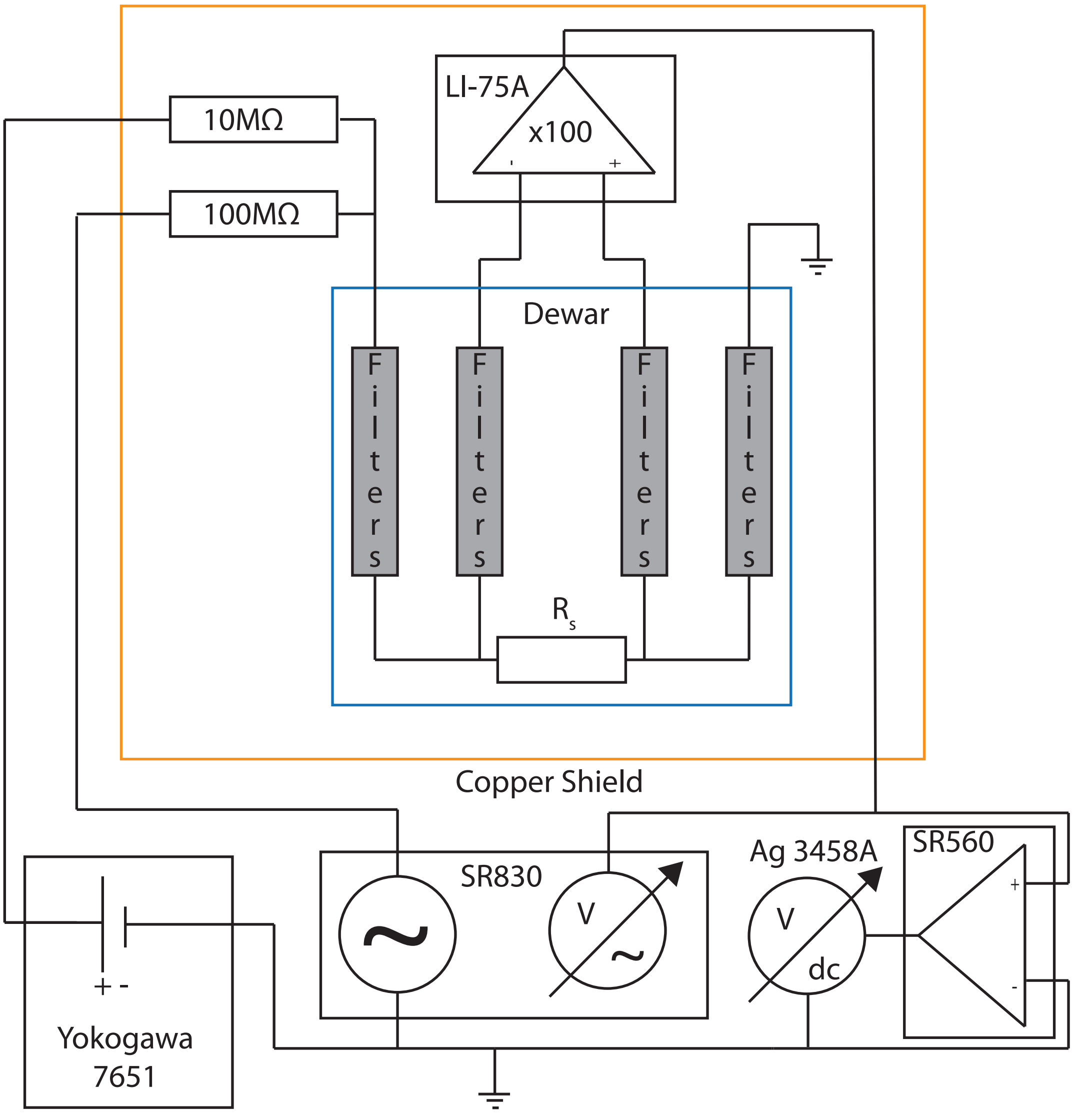

Figure 3.4: Current Bias setup $IV + dI/dV$: The dc-current is defined by an external voltage source and a series resistor. The additional ac-current is superimposed by the SR830 internal ac-source and an additional series resistor. The resulting voltage drop across the sample is amplified by an NF LI-75A low noise differential pre-amplifier. The amplified dc signal is separated from the ac signal by a SR560 pre-amplifier and measured by an Agilent 3458A multimeter.

3.2.2 High Resistance - Voltage Bias

The insulating state was measured in the same dilution system: Base temperature of 25 mK electromagnetic shielded with a grounded copper box, all feed-throughs have a pi-filter HF filtering. Since the applied voltages are less than one mV a voltage divider is attached directly to the bias input line of the cryostat. Thus, the voltage delivered by the voltage source can be a factor of $100 - 10000$ larger and therefore the ratio of the collected voltage noise, usually of the order of $10\,\mu\mathrm{V}$, to the signal voltage is also a factor $100 - 10000$ better. Since the resistances can be very high the corresponding current is very low and therefore a current to voltage transimpedance amplifier is used with a very tiny noise level.

The typical setup, used for sample S (see chapter 5), is presented in figure 3.5. As the main voltage source a Yokogawa7651 was used which is decoupled from the common ground and grounded to the copper shield which enclose the entire cryostat and the sensitive measurement lines. A voltage divider (1:1000) with the resistances of $\approx 680\Omega$ and $\approx 0.7\Omega$ was attached to the input line of the cryostat. The outgoing current was measured by a low noise DL1211 current to voltage transimpedance amplifier with a typical gain of $10^{-9} - 10^{-11}$ A/V and rise time of $0.3 - 1$ second for dc measurements. The resulting voltage was then measured outside the copper box by an Agilent 3458A digital voltmeter. In order to reach the specified noise level of the amplifier one has to be aware of external noise sources. The main contributions are 50 Hz ground loop noise, power consuming devices, e.g. heat guns, and mechanical vibrations.

The 50 Hz noise cancellation is a very tricky and not always an obvious task and I would like to note that finding ground loops is usually a try and error task since the exact internal connections scheme inside a device are sometimes well hidden in the manuals or just not specified. In general, a star point grounding is advised but not always achieved; especially, when many devices are connected to the measurement, e.g. thermometers, parallel sample measurement. The second best method and sometimes easier to achieve is the "heavy grounding" approach. This means that all devices are grounded with a very low Ohmic (copper cables) to one "star point" but the interconnection between the devices, e.g. BNC and GPIB cables, can add another grounding. This copper cable grounding has happened to be the most reliable grounding since it can occur that the outer shield of a BNC cable can do a bad connection ($R > 1\Omega$) between two devices. For the frequency range of the performed measurements (< 1 kHz) this method was sufficient.

Mechanical vibrations can lead to voltage noise due to piezoelectric effects in the flexible BNC cables. Therefore, the sensitive, non-amplified connections should be as short as possible and they should be mechanical decoupled from the lab floor which is fulfilled inside the copper box.

In order to simplify the setup and to shorten the sensitive part of the setup between the voltage divider and the pre-amplifier the Femto DDPCA-300-S was bought and used

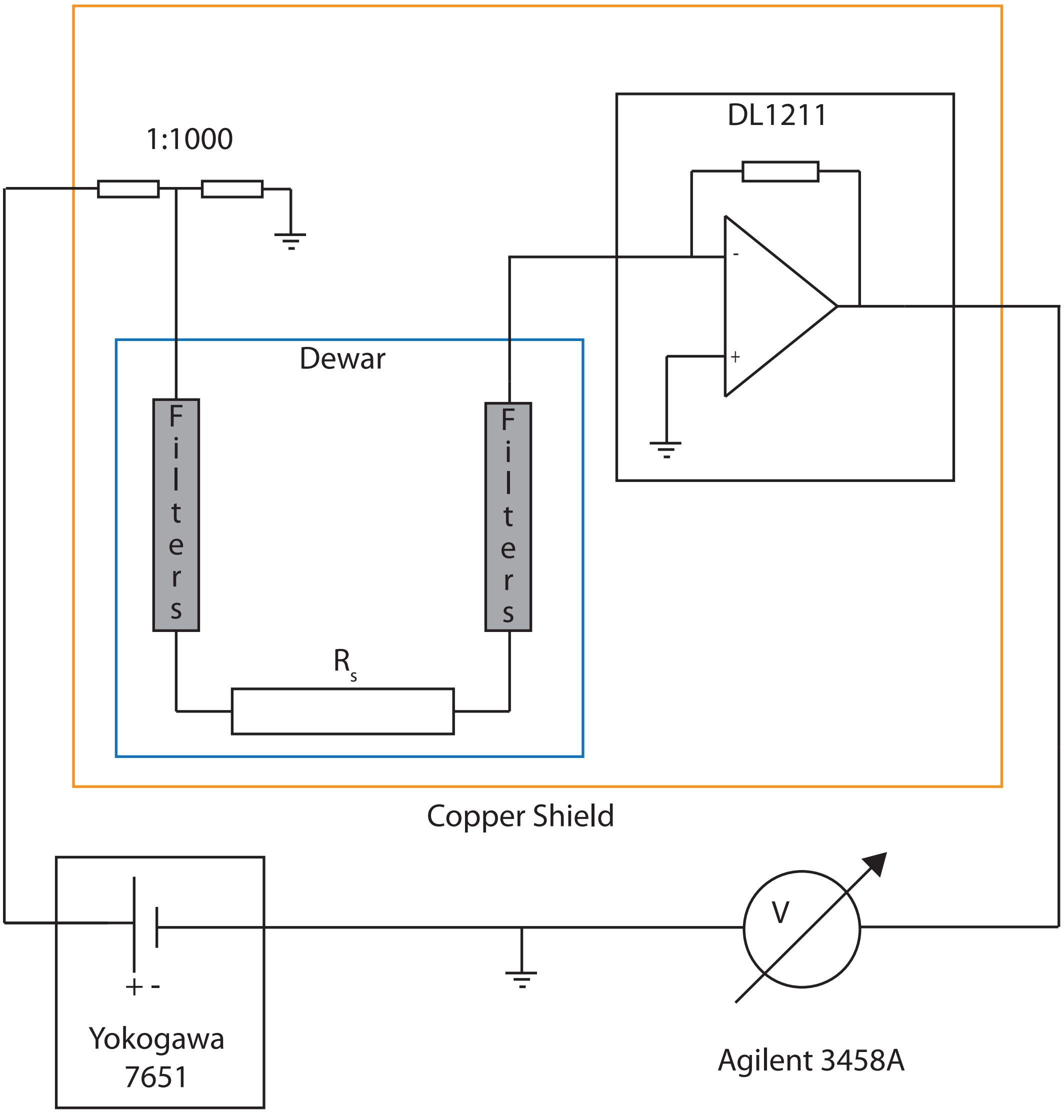

Figure 3.5: Voltage bias setup: The external voltage is provided by an Yokogawa 7651 voltage source. The voltage applied to the sample is the external voltage divided with a voltage divider. The resulting current is amplified by a current to voltage DL1211 transimpendance amplifier and measured by an Agilent 3458A DC multimeter.

for the measurements of sample I (see chapter 5). The device was customized by the company such that the bias current can be applied to the non-inverting input of the operation amplifier. Additionally a divider (1:-100), a 8 Hz low pass and a voltage buffer is used for the bias input for a stable biasing. With the biasing already inside the amplifier, only one side is needed and the other side of the sample just needs a ground cap or a cold mass connection inside the cryostat. Another advantage is that the gain can be set by the measurement PC which was not possible before. This feature was not used

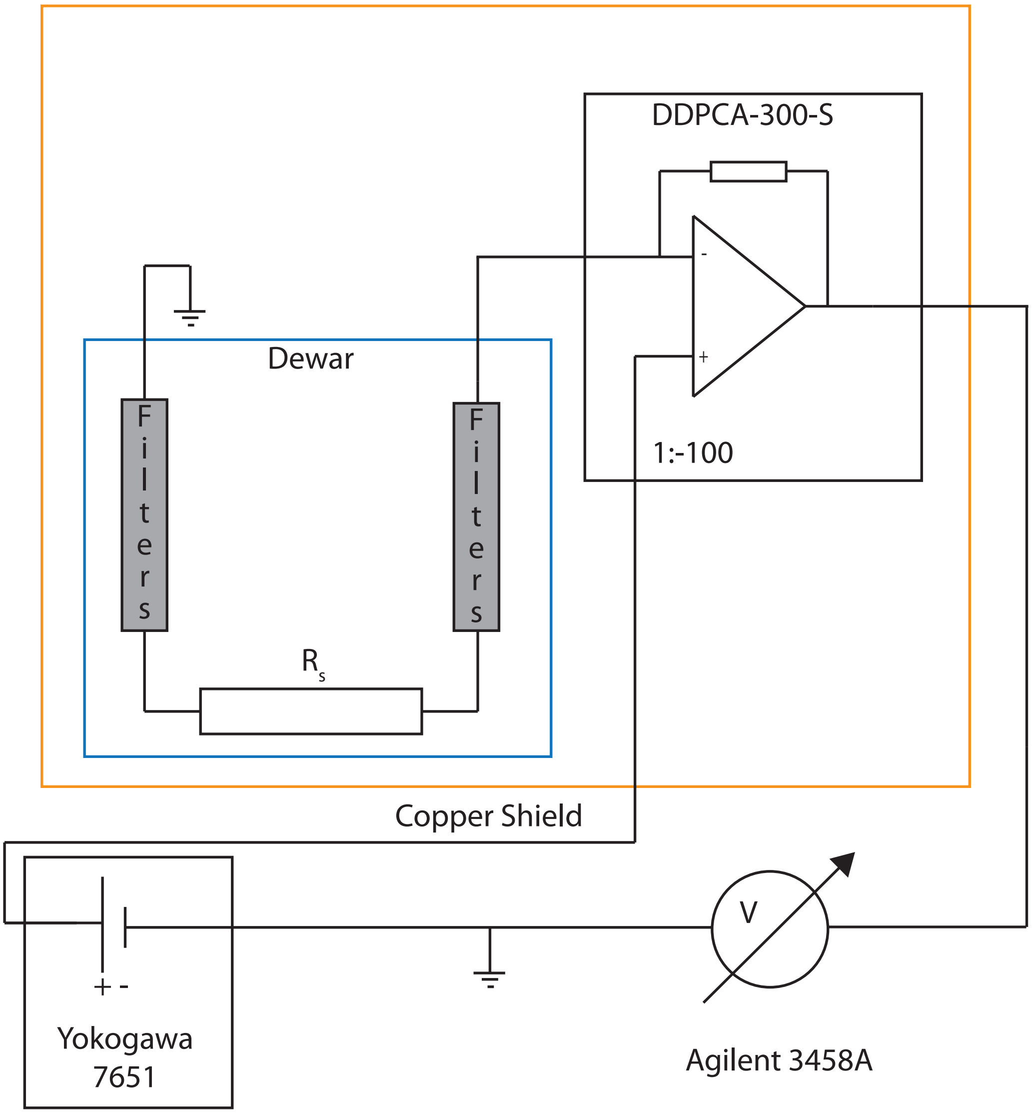

Figure 3.6: Improved voltage bias setup: The voltage bias is applied through the amplifier. The other end of the sample is terminated by a ground cap. The needed current employing the voltage is then amplified by the Femto DDPCA-300. The resulting voltage is measured by an Agilent 3458A multimeter.

yet but should not be a problem. The final setup is displayed in figure 3.6. Since the device is very small it could be put directly onto the input connection of the cryostat using a sponge as an additional suspension. Thus, all cables could be removed from the sensitive part of the measurements. With this method it was much easier to achieve a setup which was within the specified noise level of the amplifier and as good as the DL1211 noise or even better.

3.2.3 Magnetoresistance

The resistance is changing dramatically with applied magnetic field. Additionally, the regime where the resistance can be extracted is strongly field dependent. The resistance as a function of the magnetic field is measured in an ac setup. When the resistance is small, a current excitation is used and the voltage response is measured. When the resistance is high, a voltage excitation is used and the resulting current is measured. In the low resistance regime the current bias is used setup shown already in figure 3.4. The bias is set to zero and the ac excitation has to be big enough to measure a resistance at very small resistances but small enough to be still in the linear regime.

At high resistances a voltage bias ac setup is used. The ac excitation is applied via a voltage divider (1:10000). The external ac voltage is provided by the SR830 lock-in. Since with increasing resistance the cut-off resistance of the system is decreasing, the used frequencies are between 1-$3\,\mathrm{Hz}$.

Chapter 4

Electron-Phonon Decoupling

The overheating analysis described well the $I-V$ jumps in InO [14]. But is it the only mechanism that leads to $I-V$ current jumps? The shown data in [14] were taken above the upper critical field where the superconductor is considered to be destroyed and just a normal, but very disordered, metal remains. Consequently, we need to investigate the region where the superconductor-insulator transition happens, i.e., the area below the critical field where the resistance increases several orders of magnitude from zero magnetic field to its maximum. In this region the current-voltage relation shows a strong non-linear behavior below the threshold voltage which supports a charge-anticharge BKT like transitions originated from a Josephson junction array. From this model a threshold voltage is expected too where the voltage exceeds the global charging energy of the network.

First, we take a look at the $I-V$ isotherms. The sample S is an etched hall bar with 26 squares in series. The resistance was tuned by heating in ambient air such that it is close but below the disordered driven superconductor insulator transition. Since the sample is highly resistive an 2-point voltage bias setup was used. The measurement was performed in dilution fridge with a base temperature of $\approx 25\,\mathrm{mK}$. The magnetic field was applied parallel and perpendicular to the sample. The presented $I-V$'s in figure 4.1 shows the magnetic field with the broadest threshold voltage at base temperature. In the left graph we see the isotherms measured in parallel field at 1.5 T. As the temperature drops the resistance increases. Below 100 mK the $I-V$'s start to bend until a jump in the current arises below 40 mK with hysteresis and current upturn below the threshold voltage similar to the isotherms in [14].

Now, let us focus on the perpendicular field. The right graph in figure 4.1 show the isotherms at 0.9 T in perpendicular field. First, we see a smooth opening of a high resistive state with hysteresis in the threshold voltage but the threshold voltage is larger than in parallel field. Moreover, the current below the threshold is much smaller too and does not always show an upturn. Additionally, the jump from the high resistive state to the low resistive state fluctuates whereas in parallel field it increases monotonously with lower temperature.

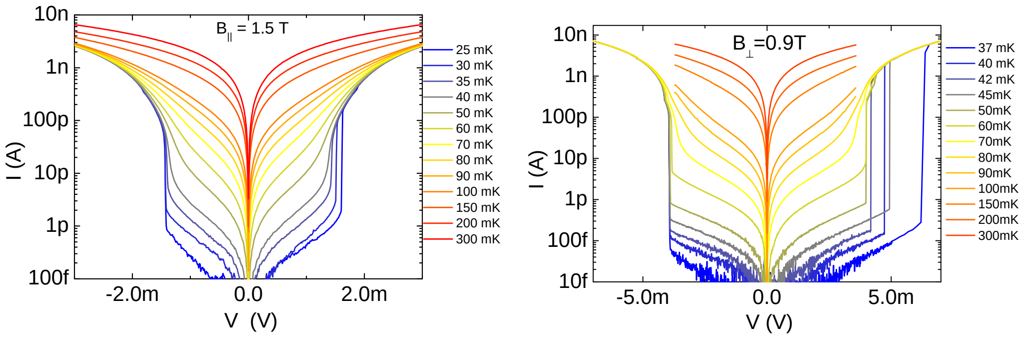

Figure 4.1: *left*: $I-V$ isotherms measured in parallel magnetic field at $B = 1.5T$, below the maximum in $R(B)$. The voltage is swept from left to the right. *right*: $I-V$ isotherms measured in perpendicular magnetic field at $B = 0.9T$, below the maximum in $R(B)$.

For a quantitative heating analysis we need to transform $I-V$ into $T_{el}-V$. Since the resistance rises above the experimental limit or the $I-V$ is intrinsic non-linear at zero bias, and thus the resistance is not defined, the transformation can only be done above a certain temperature and local resistance. In figure 4.2 we see the extracted $T_{el}(V)$ for both B-field orientations. In the parallel field we see that the electron temperature is bending down at low bias and thermalize with the bath. At high bias the curves converge to one temperature which is determined by the local Joule power heating. With decreasing temperature the down bending gets stronger and stronger until the discontinuity, visible in $I-V$, occurs at ≈ 38 mK too. Below the threshold $T_{el}-V$ show similar characteristics as the $I-V$'s, i.e. hysteresis, monotonic increase of V_{HL} with decreasing temperature and in particular the upturn in $T_{el}(V)$ before V_{HL}. The increase of the threshold voltage V_{HL} with decreasing temperature is due to the fact

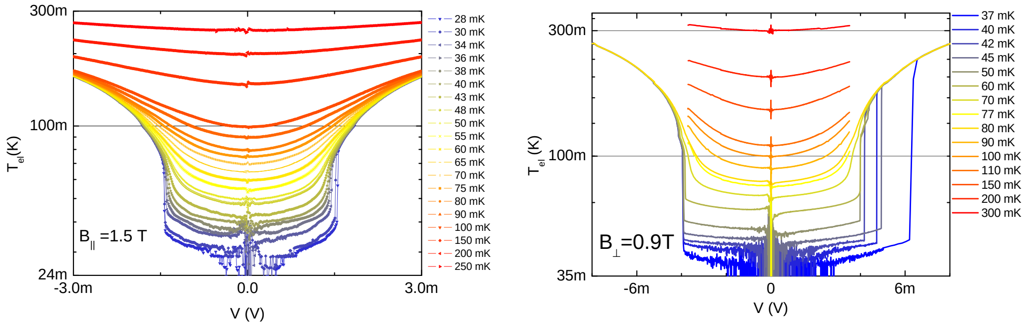

Figure 4.2: *left*: T_{el} vs V for parallel magnetic field extracted from the $I(V)$ by determining locally the electron temperature from the $R(T)$ and $R = V/I(V)$. *right*: T_{el} vs V for perpendicular field orientation down to the bath temperature where a zero bias resistance could still be measured.

that the resistance is rising steep enough such that the Joule power $P = V^2/R$ is decreasing faster for fixed V than the electron-phonon cooling in eq. 2.47 is decreasing. Henceforth, a higher voltage is needed to decouple the electrons from the phonon bath. In total the findings are qualitatively in good agreement with the ones in InO [14]. For higher temperature above 70 mK in perpendicular field orientation $T_{el}-V$ is qualitatively similar to the parallel field. In perpendicular field and low temperatures we see a different picture. The first jump at $T = 70$ mK shows the expected hysteresis and the upturn before V_{HL} but at $T = 60$ mK there is no upturn and moreover V_{HL} is even smaller. When we go to lower temperatures the randomness of V_{HL} becomes visible and we see that an upturn occurs only when V_{HL} is large whereas V_{LH} is almost temperature independent and is similar to the parallel field behavior and InO_x, respectively.

4.1 Simulation of $I-V$ characteristics

From all the experimental findings in both field orientations the question arises how much is quantitatively explainable within the electron-phonon decoupling model. The beauty of this model is that there are only two free parameters in eq. 2.47 for a given $R(T)$. First, the β is determined by the slope in the high Joule power region of the isotherms, in a double logarithmic plot as seen in figure 4.3 where the Joule power is plotted versus the electron temperature. The dashed line shows the slope for $\beta = 5$. Performing these fits for several temperatures yield a beta of $\beta \approx 5$ and a electron-phonon coupling strength $\Gamma\Omega \approx 70$ nW/K^5.

With these two parameters we can compute $I-V$. First, equation 2.47 can be rewritten as

$$V = \sqrt{R(T_{el})\Gamma\Omega(T_{el}^{\beta} - T_{ph}^{\beta})} \tag{4.1}$$

and so we can calculate V as a function of T_{el}. The corresponding I is obtained by locally applying

$$I(V) = V(T_{el})/R(T_{el}) \tag{4.2}$$

on $V - T_{el}$. In figure 4.4 the calculation for $B_\perp = 0.9$ T with $\beta = 5$ $\Gamma\Omega = 70$ nW/K^5 is shown. In the upper graph we see the electron temperature vs. the applied voltage. The most prominent feature is the S-shaped region. Here, the $I-V$ jumps occur. When approaching this region from low bias the electron temperature is close to the bath temperature until the backbending starts. The following path is forbidden, the so-called instability region, and the next possible temperature is the overheated one, decoupled from the bath temperature. When approaching from high bias, i.e. from the decoupled region, the electron temperature decreases with lower bias until the left backbending occurs and the electrons thermalize with the bath. The corresponding transformed

$I - V$ is shown in the lower graph. The dashed lines indicate the two jumps. Whereas the jump from the hot state to the cold state, V_{LH}, is almost temperature independent, the jump from the cold state to the hot state, V_{HL}, moves to higher voltages with lower temperatures. At 42 mK the model curve shows a bump in the instability region which is in the T_{el} vs. V and is caused by the extreme sensitivity about $R(T)$ and its error margin at high resistances. Remeasuring the resistance in the $I - V$ and an interpolation between the data points resolve the problem.

In the previous fits, seen in figure 4.3, the power β could be determined well; However, only $\ln(\Gamma\Omega)$ could be determined and therefore the absolute value has a considerable error margin. Since V_{LH} is almost temperature independent in the simulation and in the measurement it is suitable to fine tune the electron phonon coupling, leaving β fixed. In figure 4.5 V_{LH} for different powers of β at $T = 50$ mK is shown. Since, the electron phonon coupling changes its dimension with different β the threshold voltage is plotted vs. $\Gamma\Omega T_{ph}^{\beta}$, which is the power coming from the phonon bath. The horizontal dashed line indicates the measured threshold voltage. For $\beta = 6$, V_{LH} shows the steepest increase. For smaller β the back-flowing power is higher for the desired V_{LH}. This may seem first counterintuitive. It can be explained by rewriting the heat balance equation to

$$P = \Gamma\Omega T_{ph}^{\beta}\left[\left(\frac{T_{el}}{T_{ph}}\right)^{\beta} - 1\right] \quad .$$

The Taylor expansion around $T_{el} \approx T_{ph}$ yield

$$P \approx \beta\Gamma\Omega T_{ph}^{\beta-1}\left[T_{el} - T_{ph}\right] \quad . \tag{4.3}$$

Therefore, for a fixed Joule power P and fixed phonon temperature the prefactor in (4.3) is larger such that the difference $T_{el} - T_{ph}$ has to be smaller in order to compensate the Joule power. Hence, a strong deviation of the electron temperature from the phonon temperature occurs at higher applied Joule power for a larger β and the overheating jump occurs at a higher voltages.

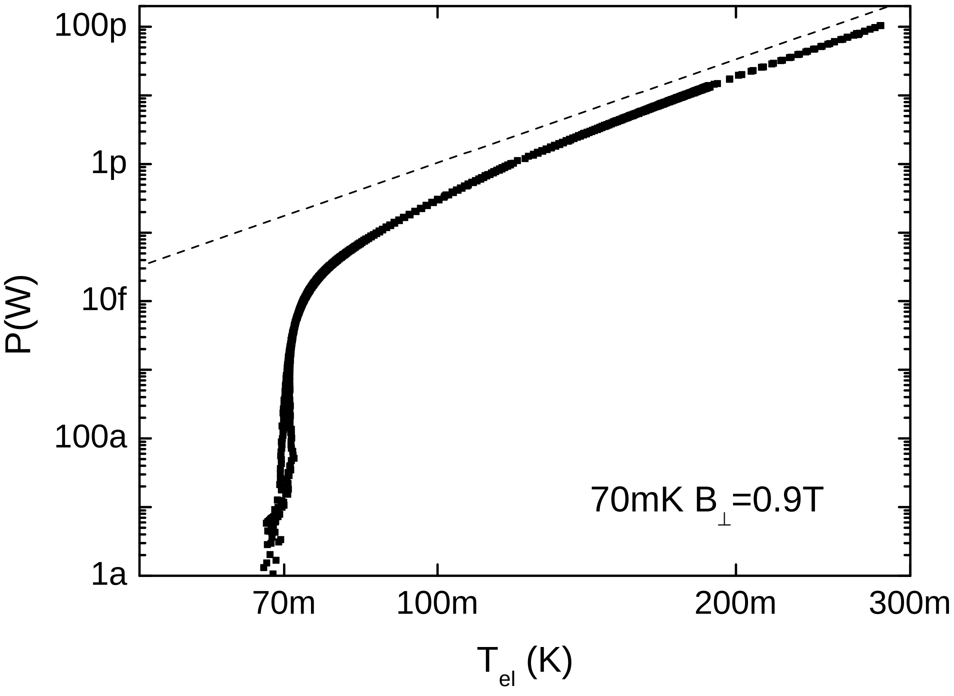

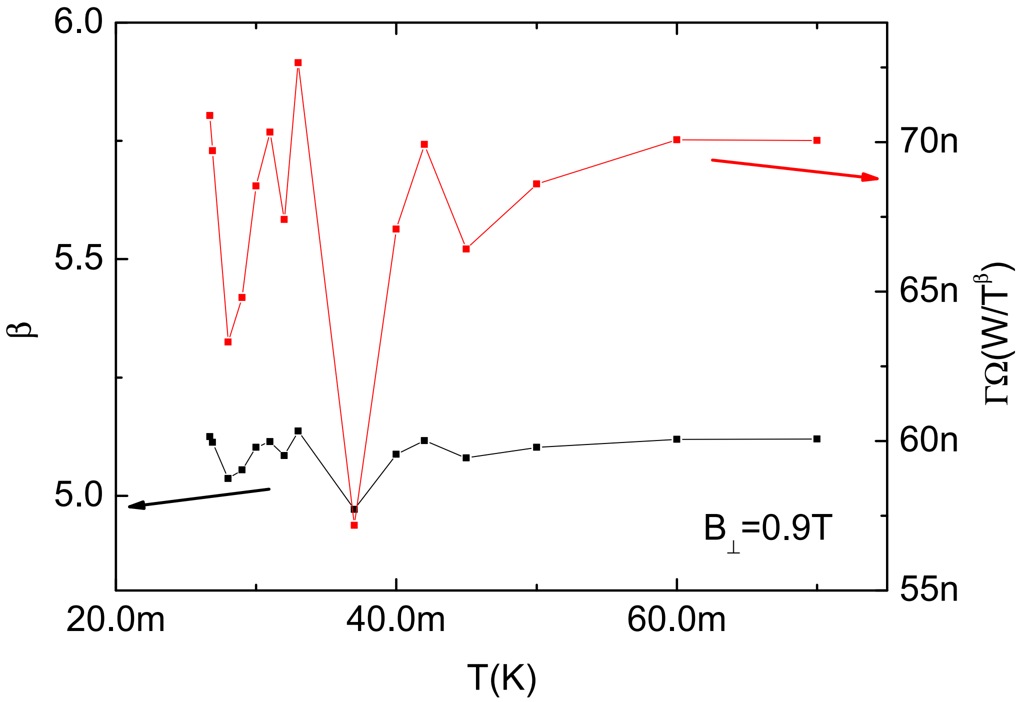

Figure 4.3: *upper*: Joule power vs electron temperature at 70 mK at $B_\perp = 0.9$ T magnetic field. Dashed line corresponds to the $P \propto T_{el}^5$. *lower*: Extracted electron-phonon couling $\Gamma\Omega$ (left axis) and power dependence β (right axis) for different bath temperatures.

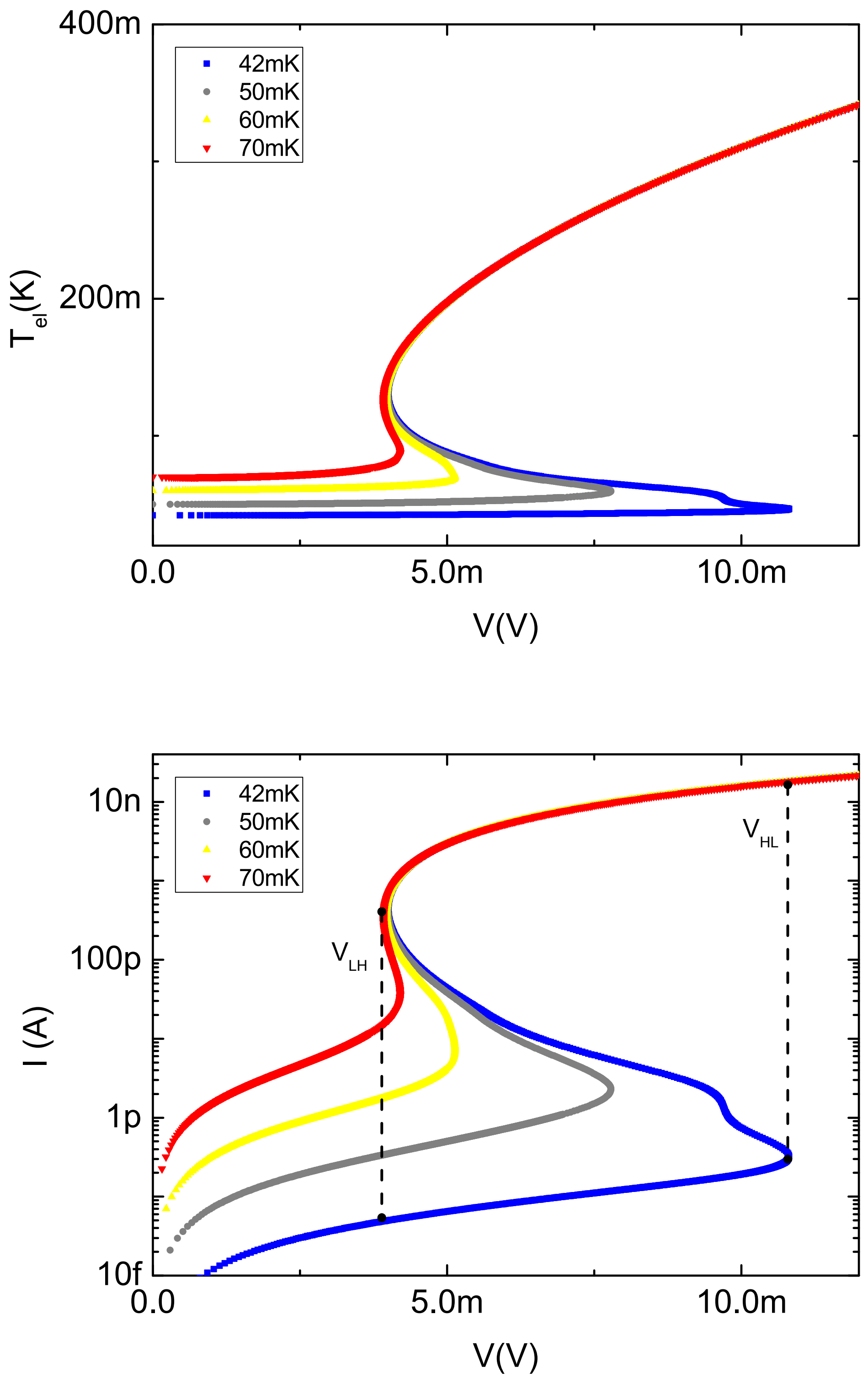

Figure 4.4: *upper:* Simulated T_{el} vs. V obtained by solving eq. 4.1 numerically using measured $R(T)$ and $\beta = 5\ \Gamma\Omega = 70\ \mathrm{nW/K}^5$, determined from the high bias fits. *lower:* Transformed $I-V$ isotherms. Dashed lines indicate the jumps V_{LH} and V_{HL}.

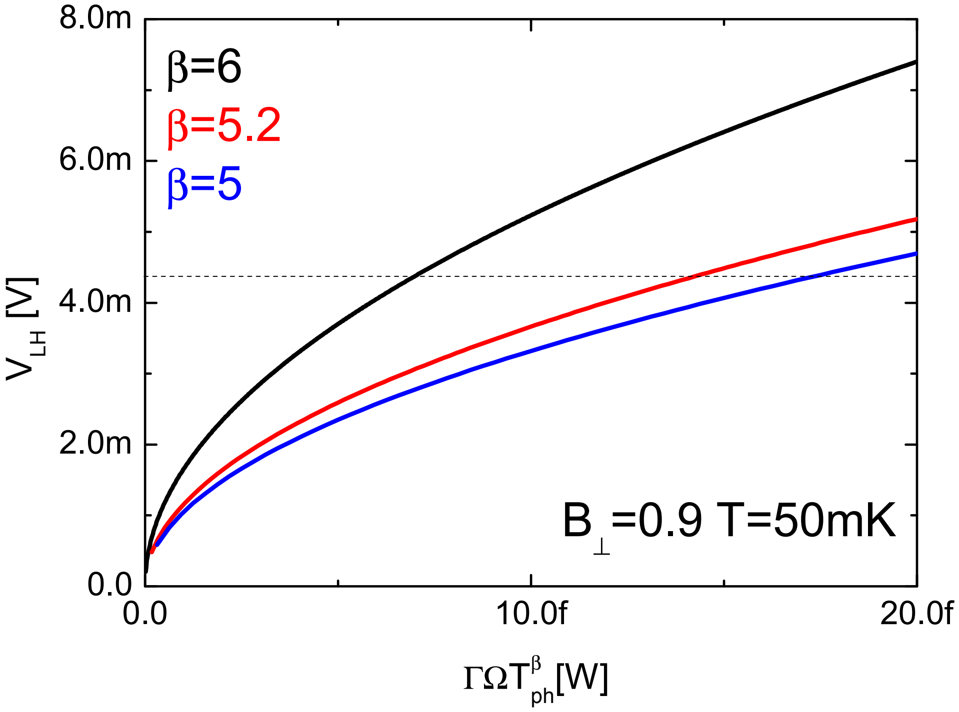

Figure 4.5: Switching point V_{HL} as a function of $\Gamma\Omega T_{ph}^{\beta}$ at fixed phonon temperature of $T_{ph} = 50$ mK. The three different curves correspond to different exponents $\beta = 6$, 5.2 and 5. The dashed horizontal line indicates the experimental switching voltage.

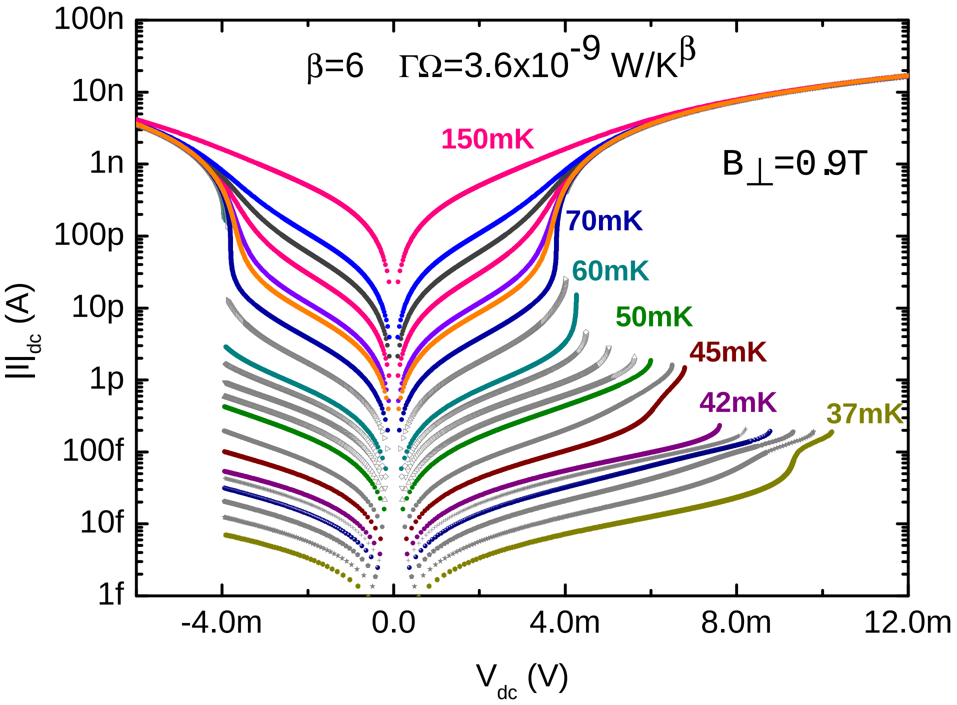

Figure 4.6: Simulated $I-V$ isothems: Solving numerically the heat-balance equation within the electron-phonon decoupling model (parameters: $\beta = 6$ and $\Gamma\Omega = 3.6$ nW/K^6) using the measured $R(T)$ at $B_\perp = 0.9$ T.

4.2 Final Results

After several iterations of the fitting scheme, described in section 4.1, we obtain the optimized values of β and $\Gamma\Omega$ in respect to the matching of the $I(V)$. The question arises whether the electron-phonon decoupling can describe the $I(V)$ at low temperatures. In figure 4.7 we see the results calculated for sample S at four representative fields. This final simulation was performed by A. Bilušić and myself. The model describes well the $I(V)$ curves at $T_{ph} > 60$ mK in $B_\perp$ (showing $B_\perp = 0.9$ T fig. 4.7a) with switching from HR to LR state and all $I(V)$s for all temperatures in parallel magnetic field orientation ($B_\| = 0.7$ and 1.5 T in fig. 4.7c,d) and in all $I(V)$s in $B_\perp$ without switching ($B_\perp = 1.75$ T, fig.4.7b). Furthermore, the model describes well the LR and the value V_{LH} even at $T < 60$ mK and correctly predicts the temperature where the first discontinuity occurs. In perpendicular field the model fails to predict the high resistive state at low temperatures (plots for $T_{ph} = 50$ and 40 mK in fig. 4.7a). In particular, the model strongly underestimates the magnitude of the current in the HR state and also overestimates the value of the jump from the HR to the LR state V_{HL}. This is clearly seen in fig. 4.7a, where V^*_{LH} the calculated value in the electron phonon model significantly exceeds the variance of the experimental V_{HL}, indicated by the gray shaded area, at $T = 40$ mK. From figure 4.5 we see that for higher $\Gamma\Omega$ the threshold voltage is increasing. Therefore, in order to move the $I(V)$ simulations closer to the measured isotherms the electron-phonon coupling has to be lowered.

Figure 4.8 presents the comparison between the measured $I(V)$ isotherms of sample I at zero magnetic field and the overheating simulations for the length $L = 2$, 5, 20 and $240\,\mathrm{\mu m}$ at $T = 80$ (left column) and $150\,\mathrm{mK}$ (right column). The value for the electron-phonon strength $\Gamma = 1.46 \cdot 10^{-10}\mathrm{W}/(\mathrm{K}^5\mu\mathrm{m}^3)$ and $\beta = 5$ was determined by using the high bias heating power analysis (see section 4.1) for $L =240\,\mathrm{\mu m}$. The corresponding simulated I(V) are displayed in red. At the temperature $T =150\,\mathrm{mK}$ fig 4.8b) the simulated isotherm matches the data for the specific length $L =240\,\mathrm{\mu m}$. At the lower temperature $T =80\,\mathrm{mK}$ (fig 4.8a)), the simulation fails to reproduce the low bias data for. The simulated low-bias current is too low and it predicts a threshold voltage while the measured isotherm shows none. However, the simulated isotherm for $L =20\,\mathrm{\mu m}$ over the whole voltage range for both temperatures (c)-d)) matches the measured isotherm, although the fit values are determined for the bigger sample. For the smaller samples $L = 2$ and $5\,\mathrm{\mu m}$ the fixed Γ produces a too high current in the simulation at low bias compared to the data (e-h), the opposite effect than in fig. a). When using the electron-phonon coupling determined at the specific length (green curves) the simulations match the measured data better. The reason of the readjustment can be seen in figure 4.8. The electron-phonon coupling strength, extracted from the high bias fit, is plotted vs the system size. With decreasing system size the coupling strength Γ seems to increase. Since the length $L = 20$ and $L =240\,\mathrm{\mu m}$ share almost the same coupling strength the simulations in 4.8 c-d) match the measured isotherms. Furthermore, the extracted electron-phonon coupling for $L = 2$ and $5\,\mathrm{\mu m}$ are larger than for $240\,\mathrm{\mu m}$ which explains the large deviation of the simulated isotherms for fixed electron-phonon coupling in 4.8 e-h). With the notion that the smaller samples can be simulated with the extracted electron-phonon coupling for the specific sample size even at T =$80\,\mathrm{mK}$, the coupling strength at low temperatures for L =$240\,\mathrm{\mu m}$ should be adjusted to lower values in order to match the isotherms.

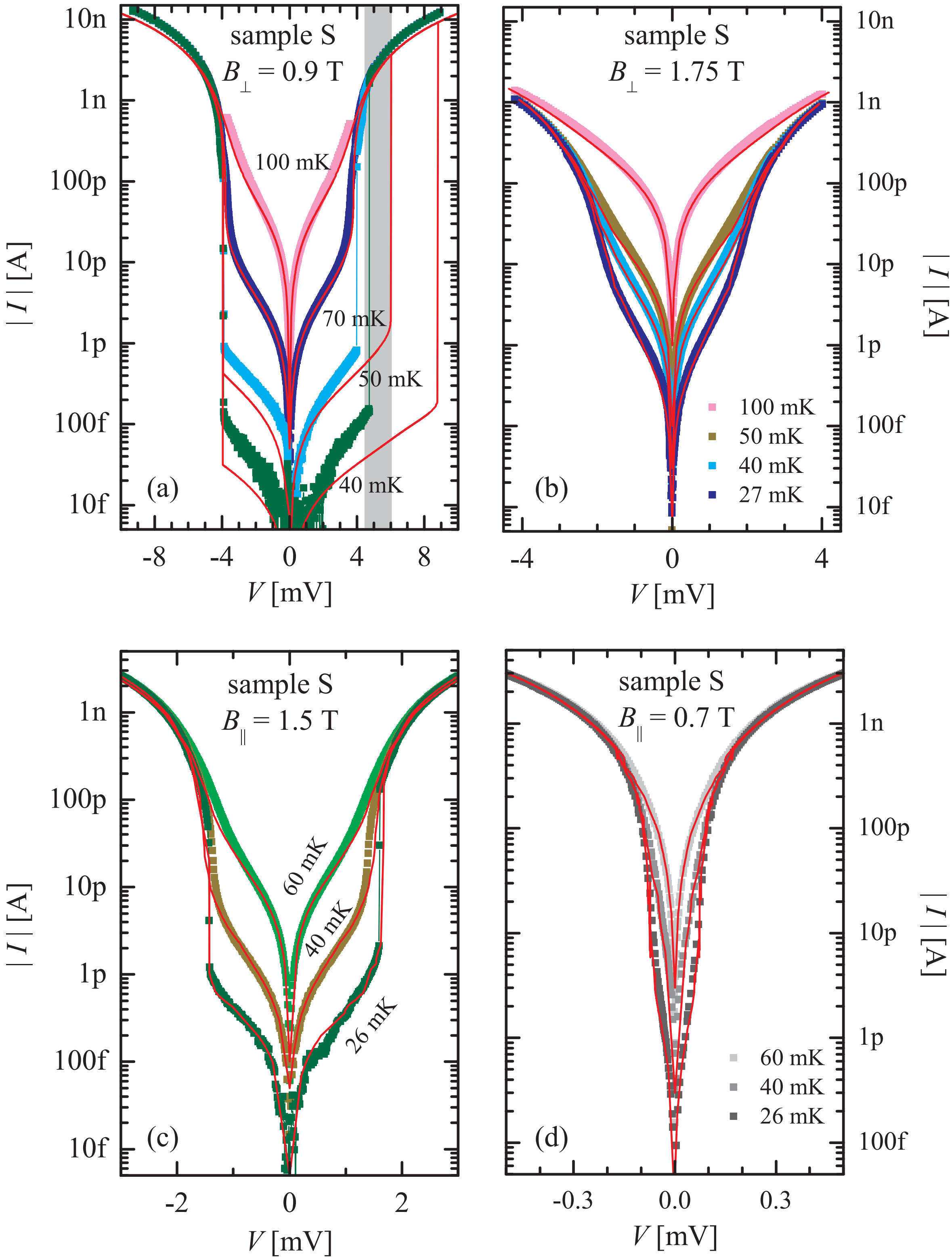

Figure 4.7: Comparison of the experimental $I(V)$ isotherms of sample S for different fields and temperatures with the curves calculated from the electron-phonon decoupling model. The voltages have been swept from negative to positive values. The gray shaded area in panel (a) indicates the variance interval of the measured V_{HL}.

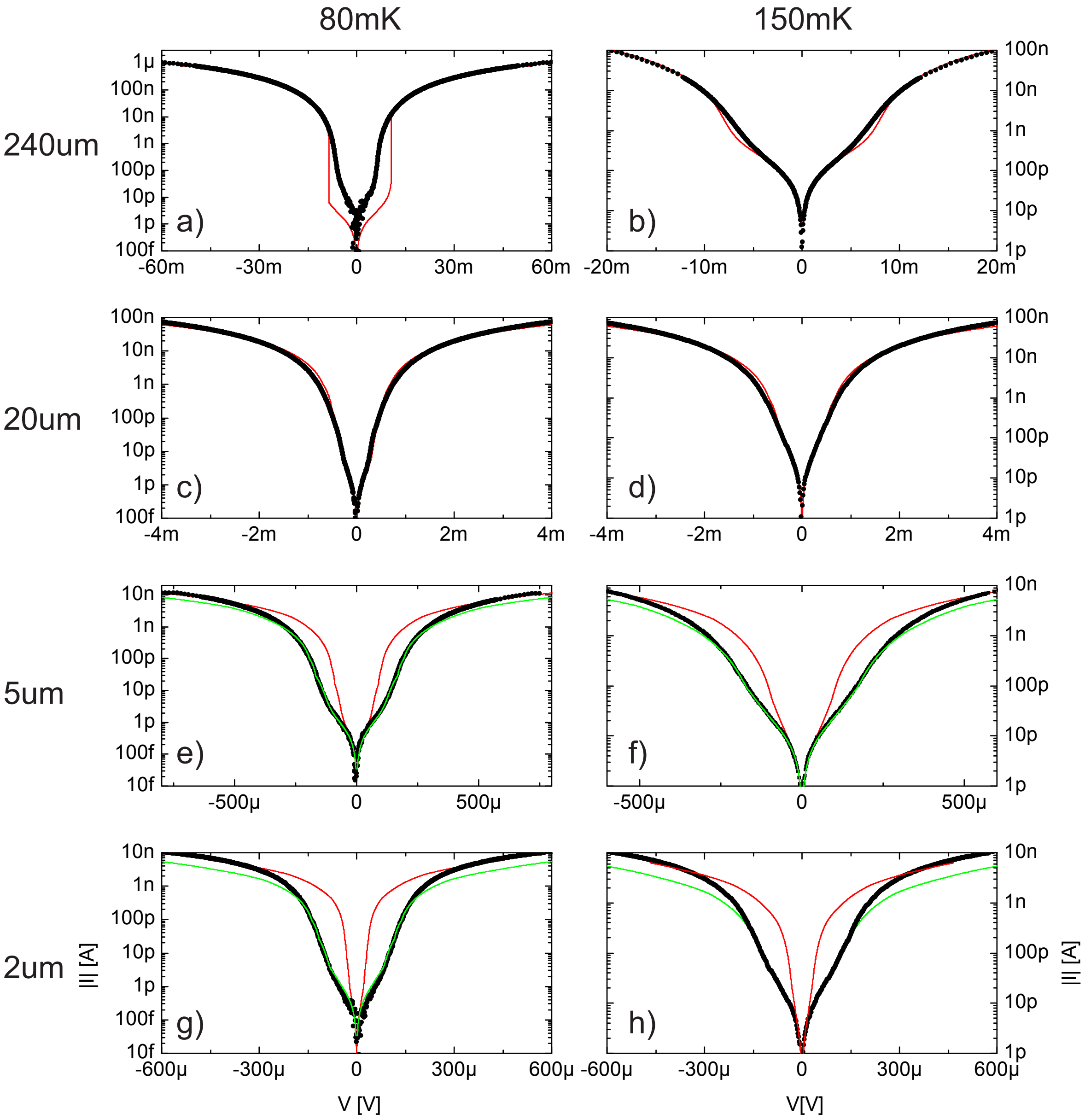

Figure 4.8: Comparison of the experimental $I(V)$ isotherms (black) and the simulation (red and green) in the overheating model for sample I in zero magnetic field for the length $L = 2$, 5, 20 and 240 µm at $T = 80$ and 150 mK. The voltage have been swept from negative to positive values. The red curves are simulations using the electron-phonon coupling strength $\Gamma = 1.46 \cdot 10^{-10}\mathrm{W}/(\mathrm{K}^5\mu\mathrm{m}^3)$ determined for the sample $L =$240 µm. The green curves (e-h) are the simulations using the electron-phonon coupling determined at the specific length at high bias.

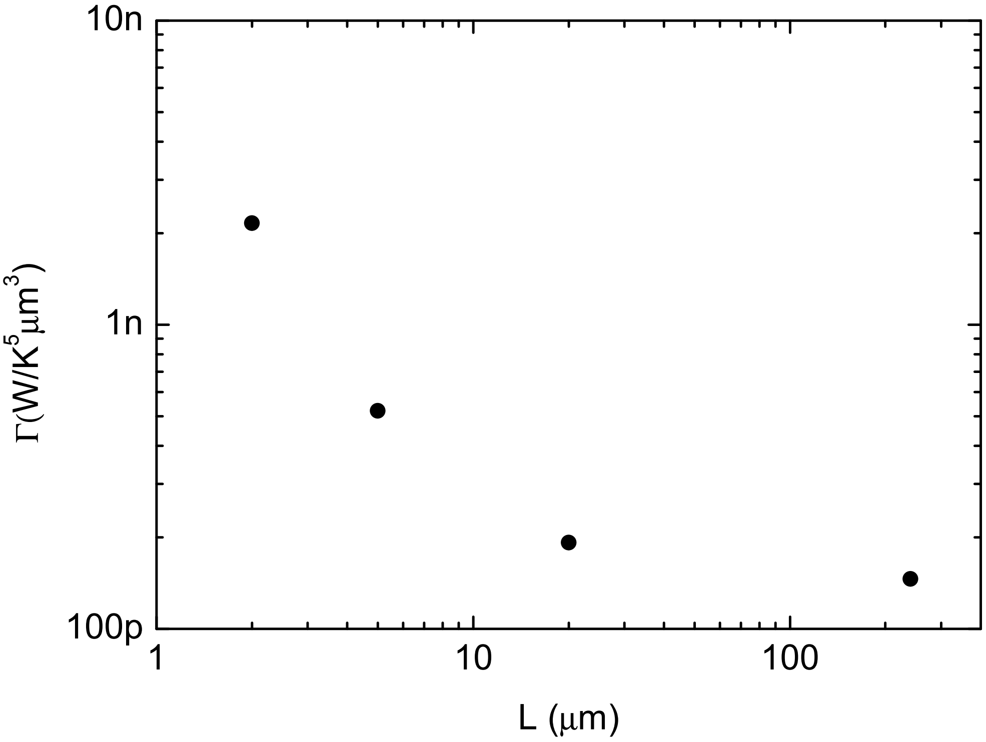

Figure 4.9: Extracted electron-phonon coupling strength Γ vs the sample size *L* of sample I

4.3 Discussion

To summarize the above observations, the high bias voltage non-linearities can be explained in the electron-phonon coupling model. Furthermore, the onset of the linear low-bias characteristics and current jumps at moderate temperatures can be explained as well in both samples.

We note that the high resistive state of sample S in $B_\perp$ deviates from the electron-phonon decoupling model and moreover that this deviation develops in the temperature range where the power law dependence of $I(V)$ deviates from linear Ohmic law, seen in section 5.3.

The heating analysis of the different length of sample I revealed that the non-linearities at temperatures $T > 100\,\mathrm{mK}$ can be explained within this model. But for the biggest sample, $L = 240\,\mu\mathrm{m}$, the simulations with the temperature independent electron-phonon coupling underestimate the current at low bias although the isotherms show qualitatively heating behavior. However, the same electron-phonon coupling strength is still sufficient to describe the isotherms for $L = 20\,\mu\mathrm{m}$. It will be seen in section 5.3 that the length $L = 240\,\mu\mathrm{m}$ shows also non-linear low bias current-voltage characteristics at low temperatures.

These deviations in both samples can be due to a phase transition charge BKT transition. However, a change in the electronic density of states with T cannot be excluded. This change can come from a phase transition, the charge BKT transition included, which affects the electron density of states and leads to an temperature dependent $\Gamma(T)$: If electrons are bound in a Cooper pair, they do not contribute any more to the electronic state and would decrease the electron phase space for the scattering, thus reducing the electron-phonon coupling strength even at a constant transition matrix element. Note, that in the analysis and the subsequent considerations the exponent β is fixed. However, a change in β with temperature is again a manifestation of a change of the system. The high bias extraction of the electron-phonon coupling revealed a decreasing strength Γ with increasing system size for sample I. The activation energy is decreasing with decreasing system size as well and therefore pushing a possible significant change of the electronic density of states to lower temperatures. This consideration is consistent with the experimental observation of the simple electron-phonon coupling. In order to prove the electron-overheating model a direct measurement of the electron temperature is desirable.

Additionally, it can be speculated that local fluctuations in the resistance across the sample creates areas with lower resistance where the current is flowing. The interplay between temperature dependent highly insulating areas and low resistive current, described by percolation, can lead to a decrease in the volume where the current is flowing. Thus, the term $\Gamma\Omega$ in the heat balance equation should be replaced by $\Gamma\Omega_{eff}(T)$. For further analysis samples with varying aspect ratios of length and width should be investigated.

Chapter 5

Superconductor-Insulator Transition in TiN

The superconductor-insulator transition (SIT) in homogeneously disordered films is considered to be a quantum phase transition which can be driven by disorder (D-SIT) or magnetic field (B-SIT). Its underlying mechanism is however still under intense debate with competing theories. In this chapter the measurement results of two samples are presented. The results will be checked against the Josephson junction array model. The first sample is still superconducting (”sample-S”) and is just below the disordered induced SIT so that a small magnetic field already turns the sample into the insulating state. The second sample is already insulating at zero magnetic field (”sample-I”). This sample consists of several squares with different length (0.5, 2,5,20,240,500 μm) and is probing the system size dependence of the transition.

For both samples dc $I - V$ measurements were performed as a function of temperature and magnetic field. In the insulating state a dc-voltage bias was used and in the superconducting/low resistivity state a ac+dc current bias setup. The detailed measurement scheme can be found in chapter 3.2. Sample S was measured in parallel and perpendicular field and sample I in perpendicular field orientation, in respect to the sample plane.

5.1 Overview

At zero magnetic field sample S is superconducting. Figure 5.1 displays the $V(I)$ isotherm evolution in temperature at zero magnetic field. The voltage is taken at the most outer voltage leads of the Hall bar. The current is swept from left to the right. At $1\,\mathrm{K}$ the isotherm is linear and with lower temperature becomes non-linear. A jump in the voltage is visible at $50\,\mathrm{mK}$ indicating the superconducting state. This superconducting state is more visible in the simultaneously performed dV/dI measurements, shown in figure 5.2. The temperatures range from 500 (red) down to $28\,\mathrm{mK}$ (dark blue). With decreasing temperatures the low bias resistance is decreasing until below $100\,\mathrm{mK}$

a superconducting state emerges with three critical currents. These currents can be associated with different domains inside the sample by measuring the inner voltage leads. The smallest critical current has has a value of $I_c = 10\,\mathrm{nA}$. The zero bias resistance for $R(T)$ is taken from the dV/dI measurements at $I = 0$.

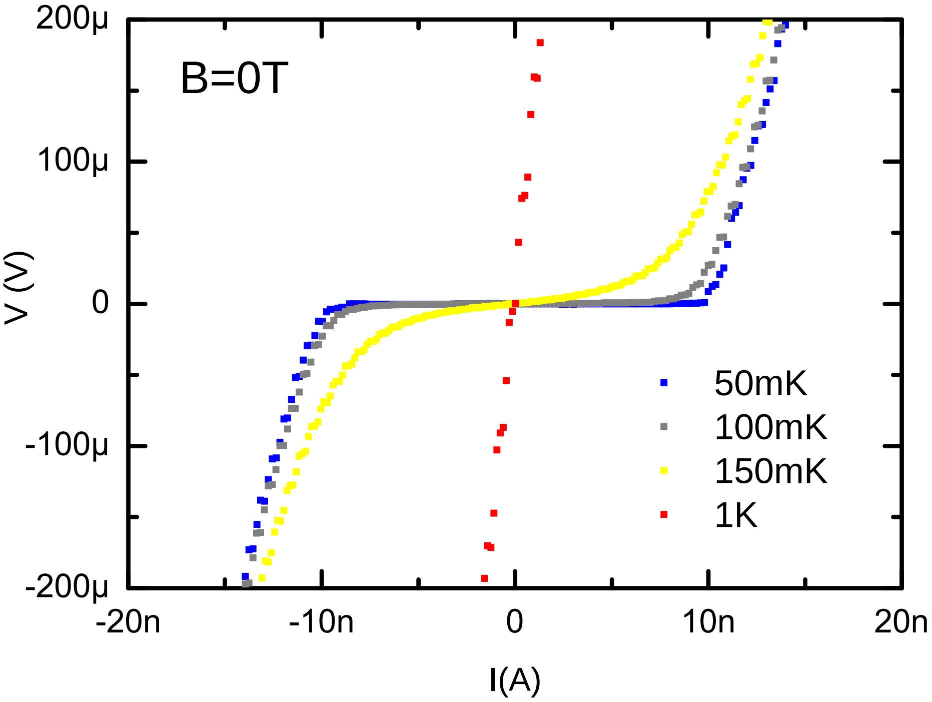

Figure 5.1: V vs I in linear scale of sample S at zero magnetic field. The current is swept from left to the right.

With applied magnetic field sample S is driven into the insulating state. In figure 5.3 the current-voltage isotherm evolution in temperature is presented. The voltage is swept from the left to the right. The upper graph shows the isotherms in parallel field orientation. The field is chosen to be close to the resistance maximum in $R(B)$. The $I(V)$ shows linear behavior at $300\,\mathrm{mK}$ between -5 and $5\,\mathrm{mV}$. With lower temperature the $I(V)$ develops a continuously growing non-linear behavior, clearly visible between -2.5 and $2.5\,\mathrm{mV}$. This non-linearity can be explained by electron-overheating, presented in chapter 4. In the lower graph the isotherms in perpendicular field orientation are presented. Again, the non-linearities are growing with lower temperature. At temperatures below $70\,\mathrm{mK}$ the isotherms exhibit a discontinuity and a pronounced hysteresis. This jump is also there in parallel field at the lowest temperatures but not visible in a linear plot. A detailed investigation concerning electron-overheating and low bias non-linearities can be found in 4.2 and 5.3, respectively. In both field orientation

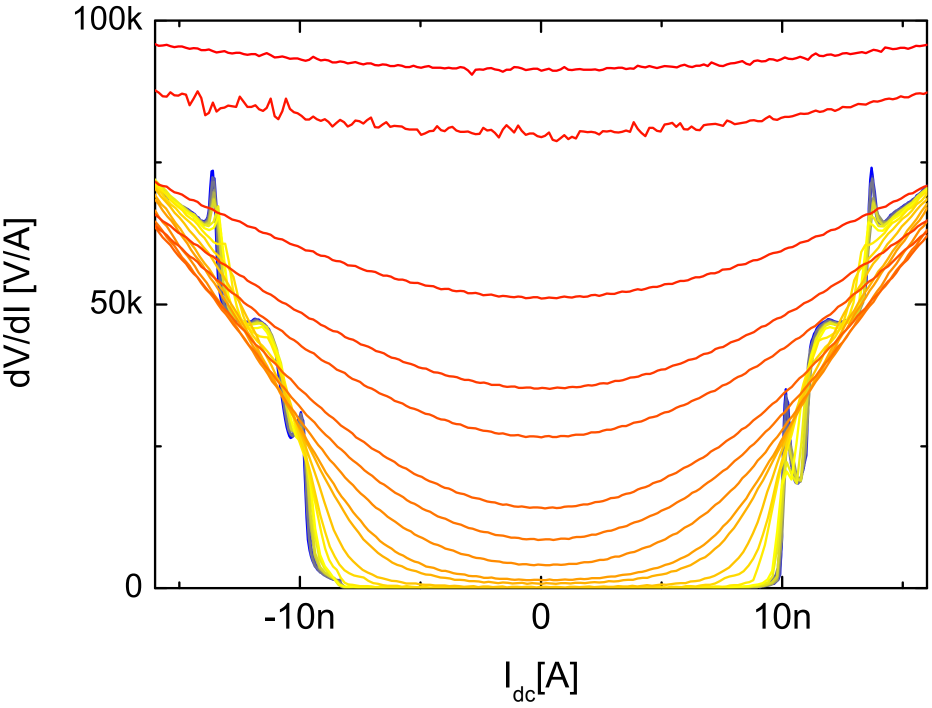

Figure 5.2: dV/dI vs. I in linear scale of sample S at zero magnetic field measured simultaneously with $V(I)$. The current is swept from left to the right. The temperatures range from 500(red) down to 28 mK (dark blue). Below 100 mK a superconducting state emerges with a critical current of 10 nA.

the isotherms are converging at high bias voltages. The blue circle emphasize that from each $I(V)$ the zero bias resistance was extracted for $R(T)$

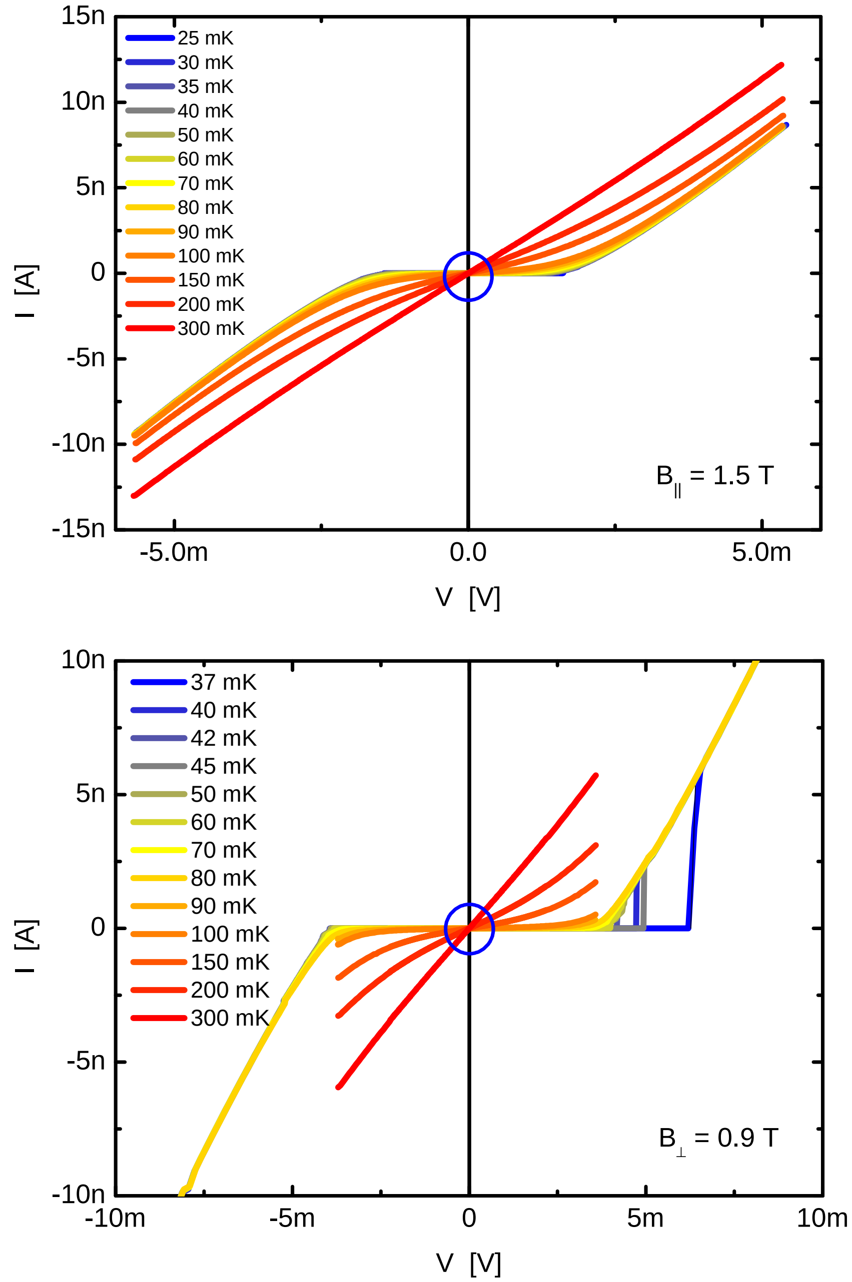

Figure 5.3: Current-voltage isotherms of sample S in the insulating state in both field orientations close to the resistance peak in $R(B)$: *Upper:* Temperature evolution in parallel field orientation with respect to the sample plane $B_{\parallel}$ =1.5 T. *Lower:* In perpendicular field orientation at $B_{\perp}$ =0.9 T. The circle is a guide to the eye indicating the low bias regime where the resistance was taken.

5.2 Activation Energy and Size Dependence

The temperature dependence of the sheet resistance of sample S and I vs. $1/T$ is presented in figure 5.4a,b. Each data point depicts the zero-bias resistance extracted from dc $I(V)$ characteristics either as a slope in the linear response regime or a secant line near $V = 0\,\mathrm{V}$ for temperatures and fields with non-linear conductance (see section 5.3). For sample S the resistance (see fig. 5.4a) in perpendicular field turns out to be several orders of magnitude larger than in parallel field. A similar results were found in amorphous InO [57] which shows a significant anisotropy in its B-SIT behavior. Note that between the measurements of the two field orientations the sample was warmed up at room temperature in order to rotate the stage manually which could change the sample. However, a difference in the room temperature sheet resistance was not observed. The superconducting state is very fragile and can be destroyed by small magnetic fields $B \leq 5$ mT. The resistance of sample I for different length L can be seen in figure 5.4b. Striking differences occur at low temperatures where the resistance of the smaller samples are saturating. In Josephson junction arrays [58] a similar saturation of the resistance was found. Common for all $R(T)$ curves is an Arrhenius activated behavior

$$R_{\square}(T) = R_0 \exp(T_0/T) \tag{5.1}$$

for a certain temperature range. The superconducting state of sample S shows also an activated behavior in the conductance (negative slope in Arrhenius plot 5.4a, $0\,\mathrm{T}$). The origin of this acitvated behavior at zero field is not clear. Interestingly, assuming that the activation energy of the negative slope is equal to the Josephson coupling $E_J/k_B = 970\,\mathrm{mK}$ the theoretical critical current is $I_c = E_J/(\phi_0/2\pi) = 20\,\mathrm{nA}$ which is close to the measured critical current at base temperature ($10\,\mathrm{nA}$). As a crude estimate we use the Ambagaokar-Baratoff [36, 37] formula for $\Delta(0) = 2eI_cR_n/\pi$, where R_n is the resistance of the tunnel junction. Using $R_n = 4.26\,\mathrm{k\Omega}$ the sheet resistance at room temperature as estimate for the tunnelling resistance yield a gap energy of $\Delta = 27\,\mathrm{\mu eV}$ and $54\,\mathrm{\mu eV}$ for the measured critical current and the slope of the Arrhenius fit, respectively. For reference, the bulk energy gap is $\Delta_{\mathrm{bulk}} = 760\,\mathrm{\mu eV}$. The determined values are in the vicinity of the values determined by STM [23] measurements for superconducting samples ($\Delta = 160\text{-}260\,\mathrm{\mu eV}$). In this paper a gap energy is estimated near the SI transition of $\Delta \approx 90\,\mathrm{\mu eV}$ for TiN; even closer to the determined value for sample S.

The activated behavior in the conductance of the superconducting state could be due to single vortex excitation known from artificial Josephson junction arrays [50]. Additionally, such "inverse Arrhenius law " is known for granular films [12]. Up to now, in quasi-homogeneous system, like our system, such activated behavior have not been observed [19] yet. In these granular films the global superconductivity is a competition between Josephson coupling and phase fluctuations [59]. The fluctuation can be thermal or quantum. The quantum fluctuation are due to the charging energy, which is the quantum equivalent to the phase.

The magnetic field dependence of the activation energy k_BT_0 for both field orientations for sample S is given in fig. 5.4c . A non-monotonic B-dependence with the maximum at $B_\perp^{\max} = 0.9$ T and $B_\parallel^{\max} = 1.5$ T, respectively, is observed. Employing the Josephson junction array model [17], explained in section 2.3, on $T_0(B_\perp)$, we can extract the plaquette size of the array by the maximum of the activation energy

$$2k_BT_0 = \Delta_c(B) = \Delta_c\left[1 - \alpha E_J(B)/E_c\right] \quad , \tag{5.2}$$

where the parameter α is of the order of unity and depends on the geometry of the lattice. The field dependent Josephson coupling energy is given by [41]

$$E_J = \begin{cases} E_J|\cos(\pi f)| & \text{1D} \\ E_J\left\{1 - 4f\sin^2\left(\pi(1-f)/4\right)\right\} & \text{2D} \end{cases} \quad , \tag{5.3}$$

with $f = eBA_{loop}/\pi h$, A_{loop} the area of either the SQUID or the plaquette in the 2D array. The maximum of T_0 is at $f = 1$. The resulting size in a 2D array of one plaquette is $30\text{-}40\,\mathrm{nm}$, which is approximately 4ξ, where ξ is the superconducting coherence length of the initial wafer.

Figure 5.4d shows the size dependence of T_0 for sample I at zero magnetic field. The observed linearity of T_0 vs. $\ln L$ is consistent with the JJA model. Using the equation

$$\Delta_C^{\mathrm{2D}} = (E_C/2)\ln(L/d) \tag{5.4}$$

yield a single island charging energy $E_C^I/k_B = 0.2$ K and a elemental Josephson junction size of $d_I = 3$ nm. It is remarkable that the logarithmic size dependence reaches from $1\,\mu\mathrm{m}$ up to $500\,\mu\mathrm{m}$, i.e. 2 orders of magnitude. Thus, a robust experimental value of slope $1/d_I$ is obtained. The size d_I is very close to the average grain size of the polycrystalline film. Following the analysis the electric screening length seems to be larger than $500\,\mu\mathrm{m}$, huge compared to conventional screening lengths. Interestingly, the value d_I is a factor 10 smaller than the determined value of sample S from the magnetic field dependence.

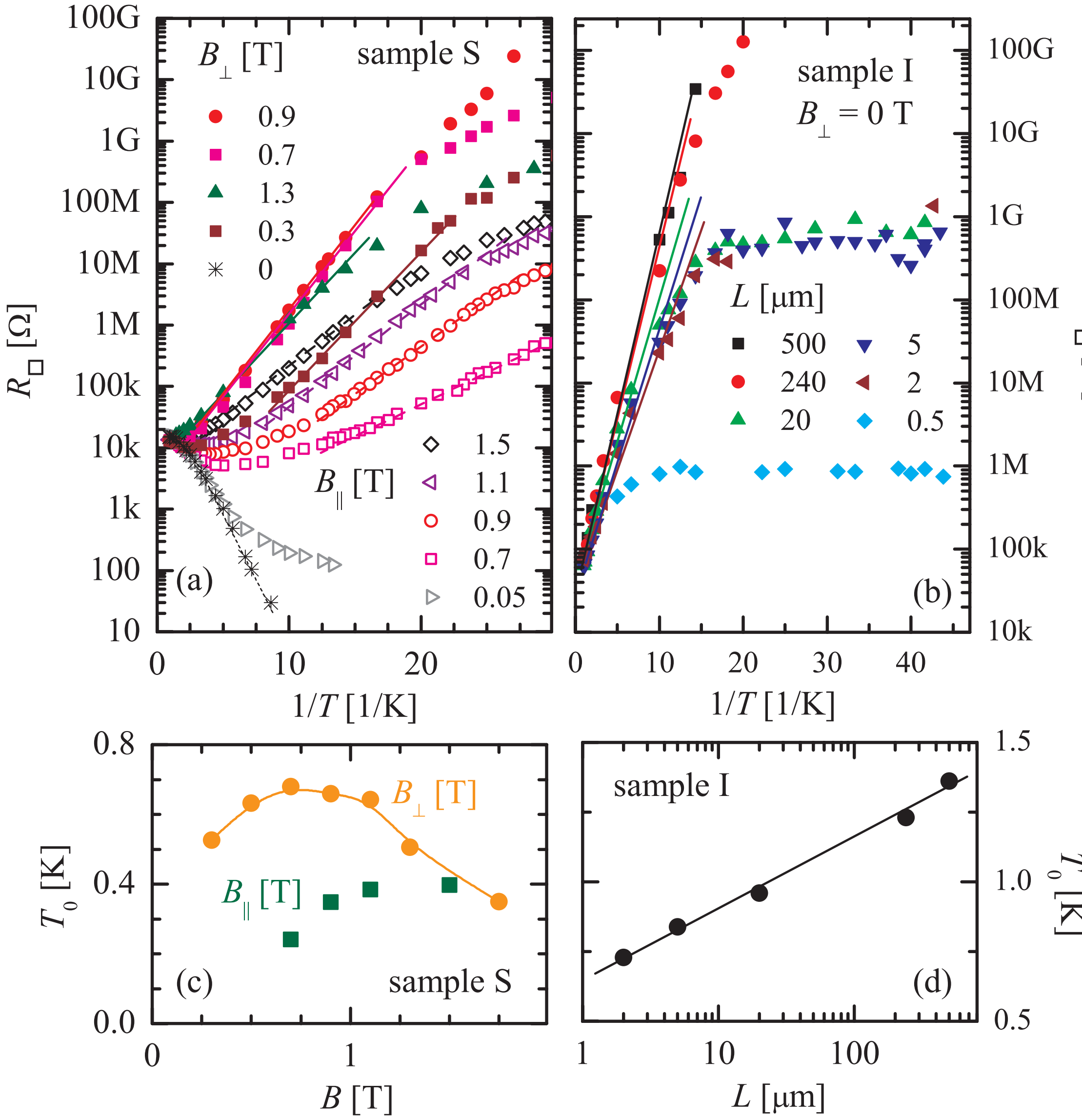

Figure 5.4: Temperature dependence of the resistance: (a) Superconducting sample for both field orientations (b) Insulating sample for different length (c) Activation Energy for superconducting sample vs. magnetic field (d) Activation Energy for insulating sample vs. sample length

5.3 Non-Linear Conductance

In figure 5.5 the $\log I$ vs. $\log V$ isotherms of sample S and I are plotted for selected magnetic fields. Sample S was measured using voltage bias setup and a DL1211 (see fig. 3.5) pre-amplifier while sample I was measured using a Femto-DDPCA-S amplifier and a voltage bias directly applied to the pre-amplifier (see fig. 3.6). Panel (a) and (b) show the isotherms of sample S at the maximum in the activation energy in perpendicular ($B_\perp$ =$0.9\,\mathrm{T}$) and parallel ($B_\parallel$ =$1.5\,\mathrm{T}$) field. Panel (c) the isotherms of sample I in zero field. Both samples and orientations show a jump from a high resistive state at low voltage bias to a low resistive state at high bias V_{HL}. At high temperature all $I-V$'s show Ohmic behavior at low bias but develop a characteristic steep with increasing voltage. At high voltages all $I(V)$'s are converging. Below $T \approx 50$ mK the switching voltages increase on average for sample S at $B_\perp$ but begin to scatter randomly over a finite temperature dependent voltage interval (see below). The high bias behavior and the onset of the $I(V)$ jumps can be modelled with a electron-phonon decoupling model, presented in chapter 4 .

While the Ohmic behavior at low voltage remains in parallel field orientation the current-voltage relation transforms into a power law dependence

$$I \propto V^{\alpha(T)} \tag{5.5}$$

in sample I and in the perpendicular field orientation of sample S. The lines in panel (a) indicate the slope α. In panel (d) the extracted α for sample S and I are shown and we see a continuous transition from the power 1 at high temperatures to the power 3 and above at low temperatures which is an expected feature for a charge-induced BKT transition: In superconductors the change of the slope in $V(I)$ is an indicator for the vortex BKT transition. Additionally, the deviation from the Ohmic law coincides with the failure of the electron-phonon decoupling model predicting V_{HL}, presented in chapter 4 which is a indication for a transition occurring inside the sample. Since these non-linearities occur in the highly-insulating state, leakage currents are an experimental concern. The samples were measured with two different measurement schemes and different pre-amplifiers. The sample S scheme measured the current coming from the sample and the sample I scheme measured the current flowing in the sample. Therefore, a leakage current would have been detected in the last measurement scheme but was not found.

Having in mind the duality between superconductor and superinsulator in the SIT [28], a similar evolution of the $I(V) \propto V^\alpha$ with decreasing temperature and the corresponding temperature dependence of α is expected to be a characteristic of a charge BKT-transition. Analogue to the vortex BKT transition the transition temperature can be determined from the condition $\alpha(T_{BKT}) = 3$. From figure 5.5d we can conclude $T^S_{BKT} = 37$ mK and $T^I_{BKT} = 26$ mK for sample S and I, respectively.

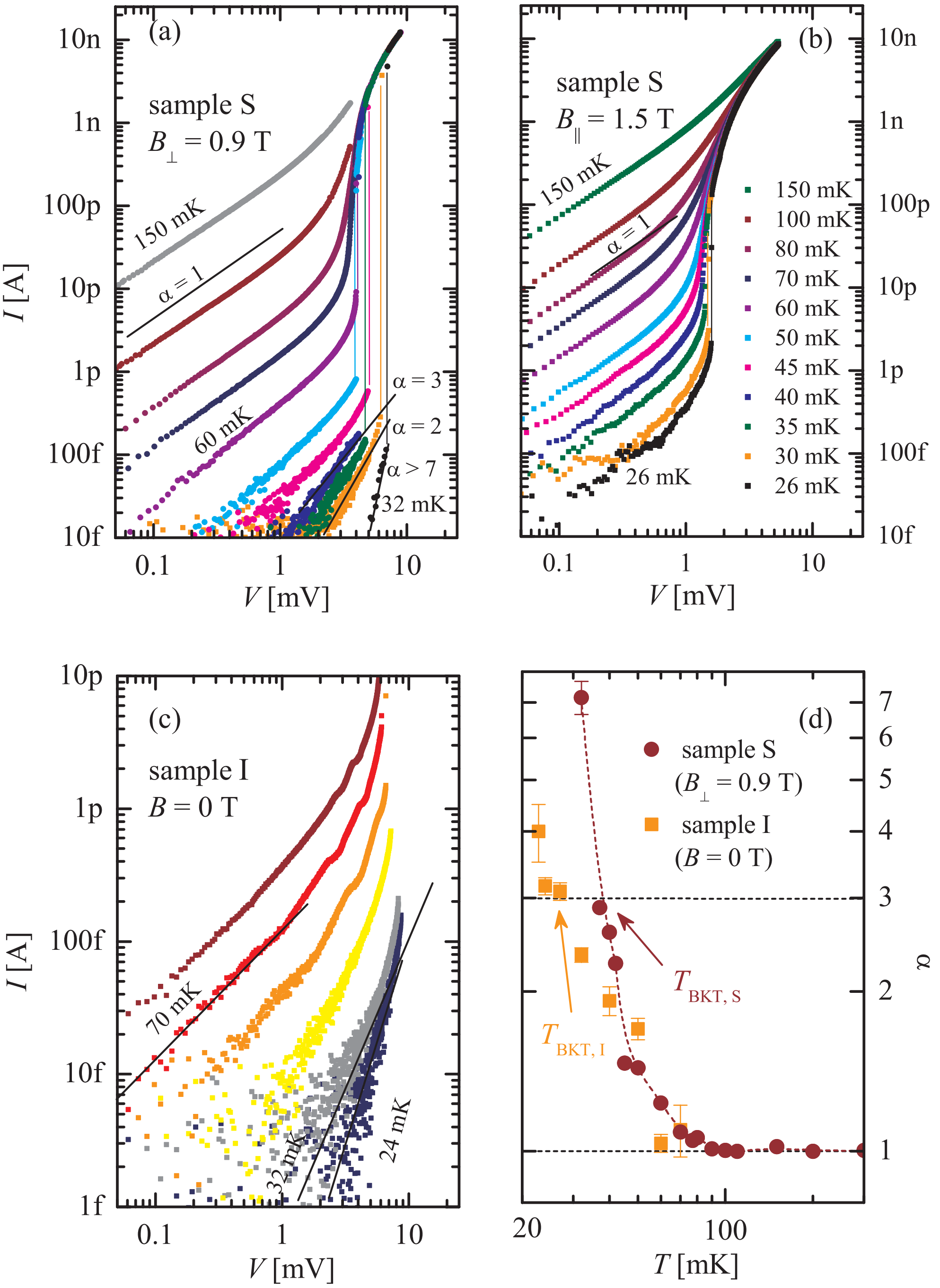

Figure 5.5: $I-V$ isotherms measured at fixed magnetic fields for parallel and perpendicular field orientation (a) isotherms of sample S in perpendicular field orientation close to the magnetoresistance resistance peak (b) isotherms in parallel field orientation close to the magnetoresistance resistance peak (c) low bias area of the isotherms of sample I. (d) extracted low bias exponent $\alpha(T)$ in $I \propto V^{\alpha(T)}$ from the isotherms in (a) and (b)

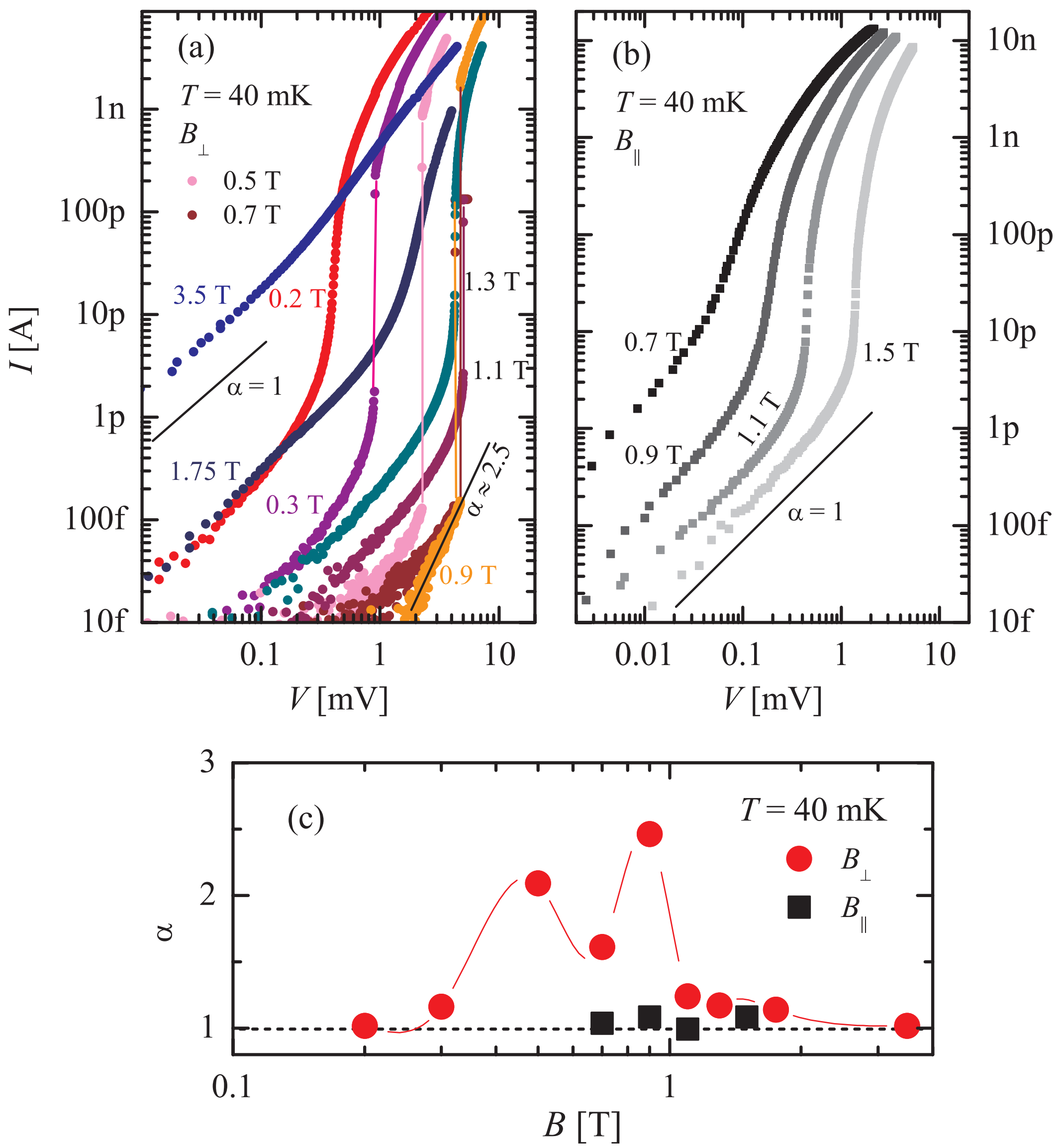

Figure 5.6: $I(V)$ isotherms of sample S at $T = 40$ mK for $B_\perp$ (panel a) and $B_\parallel$ (panel b). The voltage is swept fom negative to positive values, and only the the positive voltage is presented. The solid lines indicate the different values of α in $I \propto V^\alpha$. Panel (c) $\alpha(B)$ vs. $B_\perp/B_{max}$ at $T = 40$ mK, the line is a guide to the eye.

Figure 5.6 focuses on the magnetic field evolution of $I(V)$ for sample S at $T = 40$ mK in perpendicular (a) and parallel (b) field. In perpendicular field the high resistivity state accompanying V_{HL} is opening with increasing field and closing again after the maximum around 0.9 T. Similarly, the power dependence α, shown in panel (c), increases from a simple Ohmic dependence at low fields to $\alpha = 2.5$ at 0.9 T and decreasing again to 1. The maximum shows a double peak which is present for all temperatures. The origin of it is yet unknown.

The parallel field in panel (b) shows no discontinuity at 40 mK and, in contrast to $B_\perp$, shows always Ohmic behavior at low bias. The resistance has its maximum at $B_\parallel = 1.5$ T and therefore the high bias increase in I due to heating is at higher magnetic fields.

Next, we focus on the length dependence of sample S. In figure 5.7 I/L vs. V/L at base temperature for sample size $L = 0.5,\ 5,\ 20,\ 240\ \mu$m is shown. The axis are normalized by the sample size L for better comparison. In absence of long range Coulomb effects the sheet resistance should be size independent and all $I(V)$ should collapse. However, this is clearly not the case: For the shortest three samples the I(V) isotherms is linear at low bias but with a very different resistivity. The size dependence of the $I(V)$ curves and the saturation of the sheet resistance (cf. fig. 5.4b) at the lowest temperature is much more dramatic than expected from the weak logarithmic size dependence of the activation energy, presented in fig. 5.4d. Again, at high bias a step-like behavior is seen which originates from Joule heating. The corresponding electric field increases with decreasing sample size. Only the largest sample displays a strongly non-linear $I(V)$ characteristic at low V with a very high power-law exponent $\alpha \approx 5$. The inset displays $R(L)$ at higher temperatures $T > 4$ K, where the size dependence is reverted: The resistance decreases with L. While the precise reason is yet not known it is plausible that the patterning process, which already pushed the sample into the insulating side, affects strongly the sample edges. A locally suppressed or increased conductivity at the sample edges affects more strongly the smaller samples. An overall gradient of the local conductivity over the whole chip can be excluded since the smallest sample is placed next to the largest one.

We have seen in figure 5.5 that random switching of V_{HL} occurs at low temperatures in sample S for perpendicular field while in parallel field the V_{HL} increases monotonously with decreasing temperature. Figure 5.8 displays a close up view on the $I(V)$ of sample S in linear scale. The sweeping rate is kept slow. The points in the plots represents the real measurement points which are $\simeq 1.2$ seconds apart from each other. In a) the isotherm evolution in temperature in parallel field $B_\parallel = 1.5\,\mathrm{T}$ is shown. At temperatures $T < 50\,\mathrm{mK}$ the isotherms develop a current jump at lower voltages identified earlier with the overheating scenario. At higher voltages a jump like feature is developing. The second feature is not yet discontinuous but is bending stronger with lower temperatures. In b) the isotherm in perpendicular field $B_\perp = 0.9\,\mathrm{T}$ is shown. Below $T \leq 60\,\mathrm{mK}$ several jumps occur. In several steps the curves are reaching the high temperature curves. Note that the voltages where the jumps occur show a random behavior and do not increase monotonously with decreasing temperature, which is expected in the simple overheating model. The isotherms at very low temperature show less multiple jumps. This can be due to the fact that the isotherms are more influenced by overheating effects since the phonon cooling is less. The same observation and argument holds for jumps at high bias. If a jump occurs at high bias the system overheats and the $I(V)$ follows the high temperature isotherms. However, the randomness of the jumps remains. The

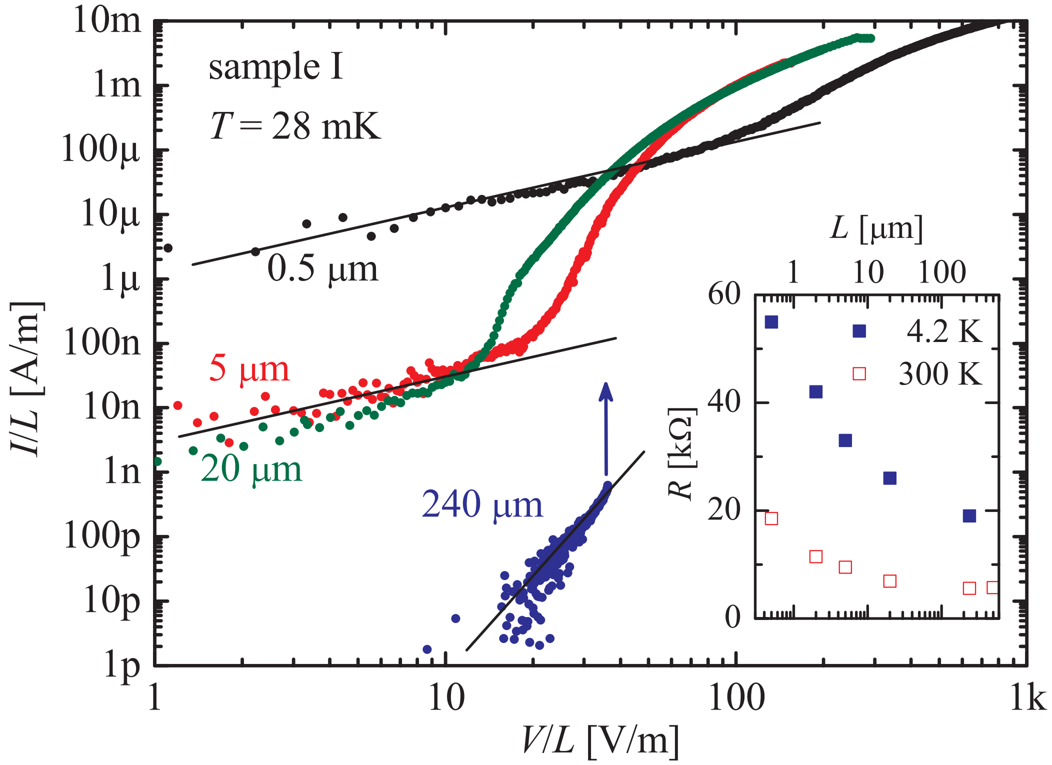

Figure 5.7: Normalized I-V-curves I/L vs. V/L at 28 mK for different sample sizes: The lines indicate power law behavior $\alpha = 1$ for $L = 0.5$, 5 and 20 μm and $\alpha \approx 5$ for 240 μm. Inset: R(L) at higher temperatures 4 K and room temperature.

randomness of the jump in perpendicular field is not observed in parallel field orientation. At intermediate temperatures $45 \leq T \leq 60\,\mathrm{mK}$ the most multiple jumps are visible. In c) the up (black) and the down (red) sweep is shown at $T = 27\,\mathrm{mK}$ at $B_{\perp} = 0.9\,\mathrm{T}$. The arrows indicate the sweeping direction. The isotherms show a strong hysteresis. The up-sweep jumps much later than the down-sweep. At high bias the isotherms are the same. The down sweep shows multiple jumps until it falls into the high resistive state. In d) the isotherms at $T = 45\,\mathrm{mK}$ and the same field as c) are shown. In this figure the jumps at negative and positive voltages are shown. At positive voltages the up and the down-sweep show similar but smaller hysteresis as in c). At negative voltages the hysteresis is there as well but the up-sweep shows a intermediate jump plateau which is absent in the down-sweep. This time difference between the two jumps is $11\,\mathrm{s}$, which is large compared to conventional electronic relaxation mechanisms.

For further investigation, we measured repeatedly $I(V)$ and extracted V_{HL} at representative temperatures and magnetic fields in $B_{\perp}$. The sweeping time for one $I(V)$ was reduced to < 1 minute (≈ 20 minutes for the regular isotherms). Figure 5.9 displays the resulting histograms of V_{HL} (panel a,b); panel c and d the temperature and field dependence of the maximum and minimum value of V_{HL}. The following observations are: (i) The histograms show sharp cut off at the maximal observed V_{HL} and the most

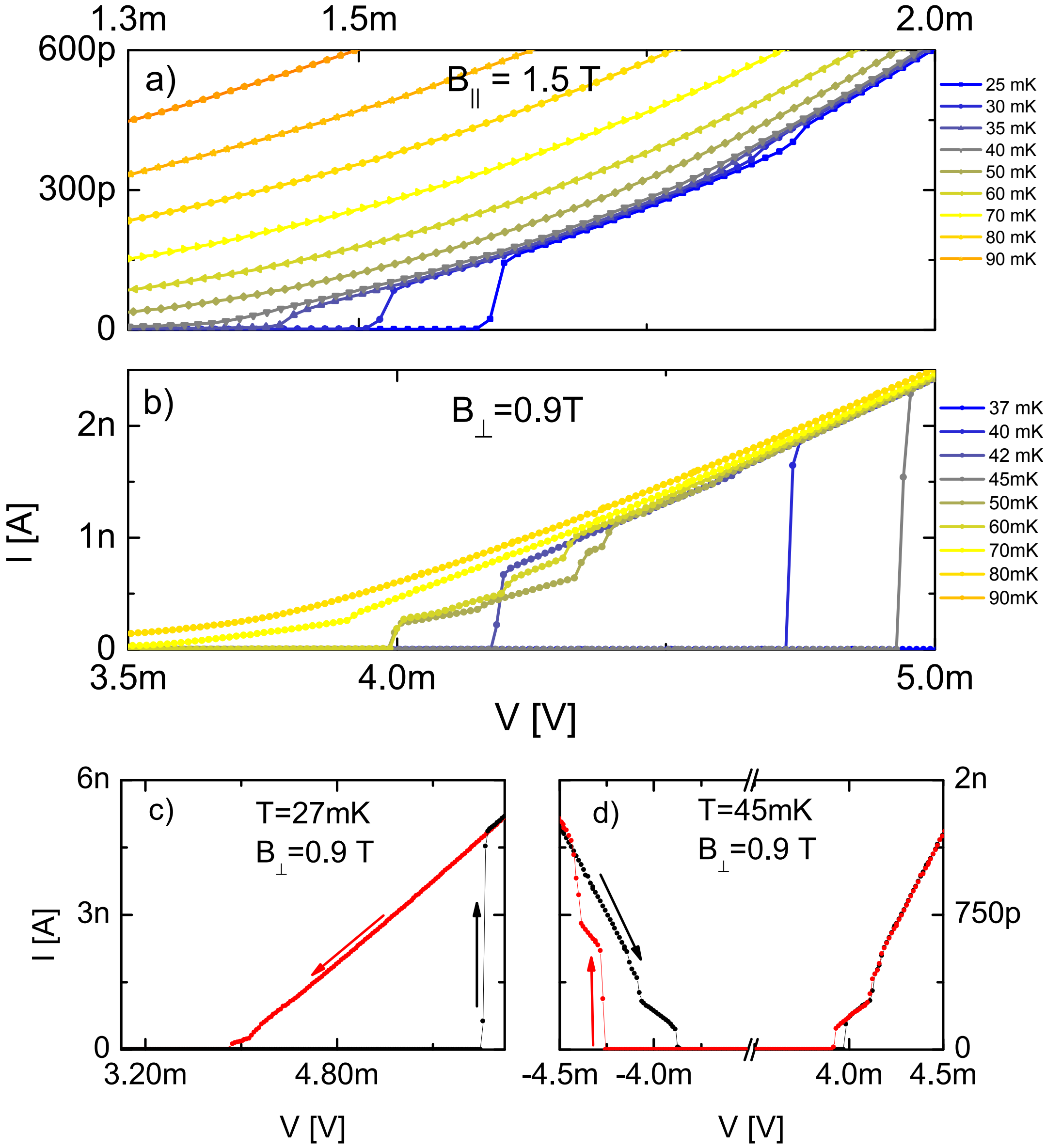

Figure 5.8: Close up view on the $I(V)$ of sample S in linear scale: a) parallel field $B_{\|}$ =1.5 T. The dots highlight the measurement points which are $\simeq$ 1.2 second apart in time from each other. b) perpendicular field $B_{\perp}$ =0.9 T; c) $I(V)$ characteristics at T =27 mK. Up (black) and down (red) sweep is shown. The sweeping direction is indicated by the arrows. d) same as c) at T =45 mK. The voltage axis is truncated at low voltages in order to show the jumps at negative and positive voltages.

probable value close to it. (ii) The field dependence of the most probable value show a non-monotonic behavior and the values are close to the observed ones in insulating samples $B = 0$. (iii) The ratio of max$\{V_{HL}(B)\}$ /min$\{V_{HL}(B)\} \approx 2$ in magnetic fields below the field where the maximum of V_{HL} is reached and drops rapidly upon further field increase. (iv) With increasing temperature the minimal and maximal values getting closer and the random distribution ceases but V_{HL} survives much longer. In the $I(V)$, in sample S, a random distribution is visible: the isotherms with a jump at the maximum show an upturn before the jump while the ones switching earlier show no upturn. Therefore, it is plausible that there are two switching mechanisms one coming from the overheating which shows no measurable random switching and an increasing V_{HL} with lower temperatures and one which show a switching distribution over a larger area and its maximal value is limited by the previous mechanism. A probable candidate for the second one could be an arc-discharge like threshold voltage of localized charge, in particular cooper pairs, which exists on the insulating side of the Josephson junction network model.

A similar $I(V)$ behavior with current jumps and hysteresis has been also observed in a variety of other systems including insulating amorphous YSi [51] and 2D Josephson junction networks [58, 60] in the insulating state. Note that the YSi is not superconducting but shows a low temperature transition from Mott variable range hopping to an activated temperature dependence due to Coulomb blockade. It was remarked that switching in YSi at very low temperatures resulted from the interplay between depinning transition of the high resistive state and overheating of electronic system, but cannot be explained by the overheating alone.

Similar multiple jumps were observed before in, non-superconducting, quantum dot arrays [61] and recently in indium oxide [62]. The multiple steps in indium oxide are interpreted as an indication of inhomogeneities of the insulating phase near the SIT. The I steps results from different current path through the sample. With increasing voltage each path can switch from the "cold" high resistive state to the "hot" low resistive state. It was found that the sweep from high bias to low bias revealed more multiple jumps. It is explained that the channels are closing one by one when reducing the voltage. Coming from low voltages, a jump into a hot state from one channel can produce an avalanche which creates a big jump into the global overheated state.

From the former observations of the switching we can conclude that hysteresis and switching only due to electron-phonon decoupling is dominant at samples with a weak insulating state: In theses samples (In this context, sample is referred to the state created by disorder or magnetic field) the insulating state is present at very low temperatures where the electron-phonon cooling is already weak. Additionally, since the resistance is smaller at this temperatures than in a higher insulating sample the Joule heating $P = V^2/R$ is also larger and so supports heating. For higher insulating samples, the insulating state is present at higher temperatures where the phonon cooling is larger. At these temperatures a switching mechanism is visible which shows an abrupt jump from the high insulating state with a broad switching voltage distribution. This explanation is consistent with our observations where the broad distribution is found in the higher insulating states. A higher resistance means that the Joule power is smaller and thus a switching only due to electron-phonon decoupling is expected at higher voltages. The high voltage cut-off in the switching histograms can interpreted as the global electron-

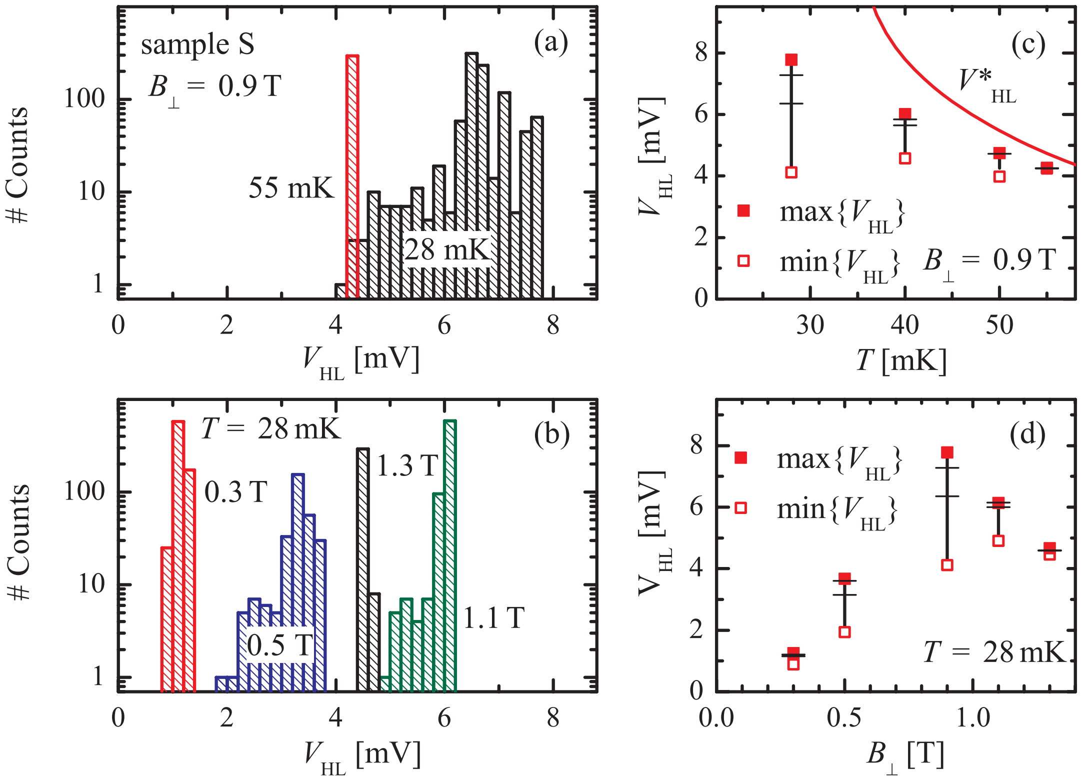

Figure 5.9: Switching histograms for the V_{HL} distribution in sample S, out of plane field orientation: (a) fixed field $B = 0.9$ T for $T = 28$ mK (total sampling number 930) and $T = 55$ mK (296 samplings); (b) fixed temperature $T = 28$ mK for $B = 0.3$T (776 samplings), 0.5 T (299 samplings), 1.1 T (708 samplings), 1.3 T (300 samplings). (c)-(d): Temperature (at $B = 0.9$ T) and field (at $T = 28$ mK) dependence of the variance range of V_{HL}, maximal and minimal values shown by solid and open symbols. Horizontal lines indicate intervals containing 75% of the data. The solid line marked by V^*_{HL} corresponds to the conventional overheating model.

overheating jump.

5.3.1 Comparison of Vortex and Charge Berezinskii-Kosterlitz-Thouless Transition

In this section, the duality between a vortex driven BKT transition and the supposed charge BKT transition will be presented further. This section is a modified version of the paper [54] by Kalok et al. . Both samples were made from the same 5 nm thick TiN wafer. Sample A is unoxidized and was measured by Baturina et al. Employing controlled oxidation in air at $\simeq 270°C$ sample S was pushed very close to SIT. Sample S also allowed for a fine tuning into the insulating state by applying a small magnetic field. The two samples differed in sheet resistance $R_{\square}(300\,\mathrm{K}) \simeq 2.52$ $\mathrm{k}\Omega$ and 4.26 $\mathrm{k}\Omega$, respectively

The temperature dependence of the sheet resistance ($R_{\square}$) of samples A ($B = 0\,$T) and S ($B_{\perp} = 0$ and $0.9\,$T) are shown in Fig. 5.10. $R_{\square}$ first increases from 300 K down to $\simeq 3.5$ K ($\simeq 1$ K) for sample A (S), and then drops to zero. The transition is fluctuation broadened [23]. The estimated transition temperatures are $T_C \simeq 1.3$ K for sample A and 0.3 K for sample S, which are both significantly lower than that of thicker TiN-films (4.7-6K). In perpendicular magnetic field sample S turns insulating.The superconducting state of sample S is very fragile and suppressed by small magnetic fields $B \lesssim 5\,$mT.

Current-voltage characteristics for samples A and S at different temperatures are plotted in Fig. 5.11: panel (a) shows $V(I)$ for sample A at $B = 0$, and (b) $I(V)$ for sample S at $B_{\perp} = B^{\perp}_{\mathrm{max}} = 0.9\,$T. Sweeping the current from zero, voltage jumps occur for sample A indicating switching from low- to high-resistive state, while sample S exhibits the opposite behavior: sweeping the *voltage* from zero, *current* jumps for several orders of magnitude as sample switches from *high*- to *low*-resistive state. The current jumps are seen over rather wide magnetic field range: from $B_{\perp} = 0.3\,$T $= B^{\perp}_{\mathrm{max}}/3$ to $B_{\perp} = 1.3\,$T $\approx 1.5B^{\perp}_{\mathrm{max}}$ for sample B. Note that these fields are well below the upper critical field in TiN superconducting films, $B_{\mathrm{c2}}(0) = 2.8\,$T. At relatively high temperatures ($T \gtrsim 1.190\,$K and $T \gtrsim 70\,$mK for sample A and S, respectively) $I(V)$ is linear at low current/voltage but develops a characteristic steep, but continuous increase with increasing current/voltage. At high current/voltages all the characteristics for different bath temperatures merge for both sample A and S. Such *high bias* nonlinearities are typical for electron overheating phenomena, both on the insulating [14] and the superconducting side [63] of the transition.

Most remarkable, is the dual behavior of the *low bias* current-voltage characteristics, where both samples develop a power-law behavior ($V \propto I^{\alpha}$ for sample A, and $I \propto V^{\alpha}$ for sample S), with a strongly temperature dependent exponent $\alpha(T)$ in the pre-switching regime (Fig. 5.11c). Similar behavior is observed for sample S in perpendicular magnetic field between 0.3 and 1.1 T. For magnetic field oriented parallel to the sample plane, no power-law $I(V)$s was observed at low bias even at the lowest temperatures reachable by our experimental setup ($T \approx 26$ mK) (See fig. 5.5b). The low T, low bias $I(V)$-characteristics of sample S in perpendicular magnetic field cannot be reproduced by

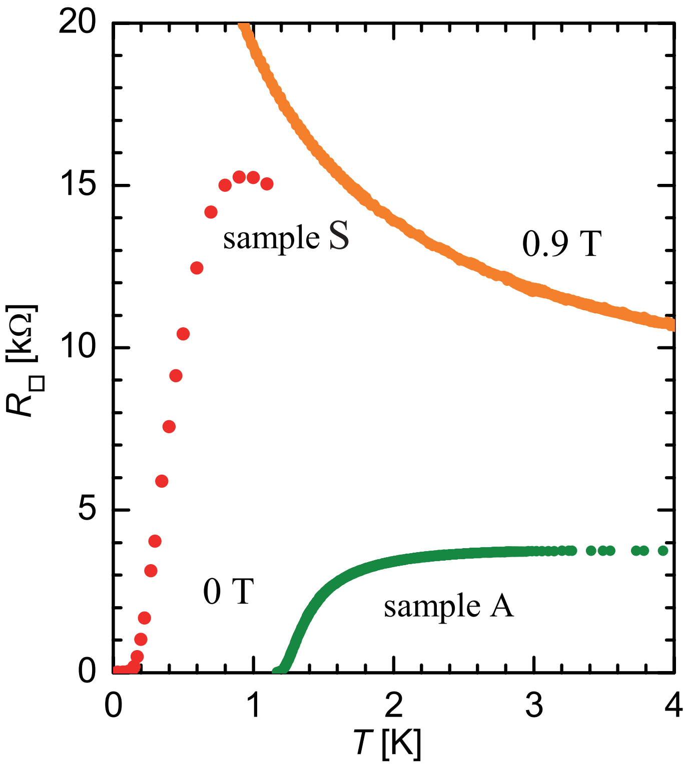

Figure 5.10: $R_\square(T)$ at zero magnetic field [samples A (green dots) and S (red dots)] and at 0.9 T [sample S (orange dots)]. Sample A was measured by Baturina et al.

means of the heating analysis of [14] (See section 4.2).

The low-bias power-law dependences of sample A are characteristic to strictly 2-dimensional superconducting films with a thickness below the superconducting coherence length and a magnetic (Pearl) penetration depth, λ, exceeding the lateral dimension, d, of the sample [in our case $\lambda \simeq 1.5\,\mathrm{mm}$ and $d = 50\,\mu\mathrm{m}$]. In such films the transition to the zero-resistance superconducting state is of the Berezhinskii-Kosterlitz-Thouless (BKT) type and occurs at $T_{\mathrm{BKT}} < T_c$, where T_c is the temperature where the superconducting order parameter appears. At $B = 0$ thermally excited free vortices and antivortices cause dissipation in the interval $T_{\mathrm{BKT}} < T < T_c$. Below T_{BKT} vortices and antivortices get bound into dipole pairs and cannot move independently and thus the resistance vanishes. Below T_{BKT} the pair-dissociation energy depends on the applied current giving rise to the non-linear $V(I)$-characteristics [64]. The BKT-transition is also characteristic to planar Josephson junction arrays (JJAs) [49] whose behavior is controlled by the ratio of two energy scales, the Josephson coupling energy E_J and the charging energy E_C. For $E_J \gg E_C$ JJAs are superconducting, for $E_J \ll E_C$ charging effects become dominant and the arrays turn insulating [35, 60]. In this limit, charges take up the

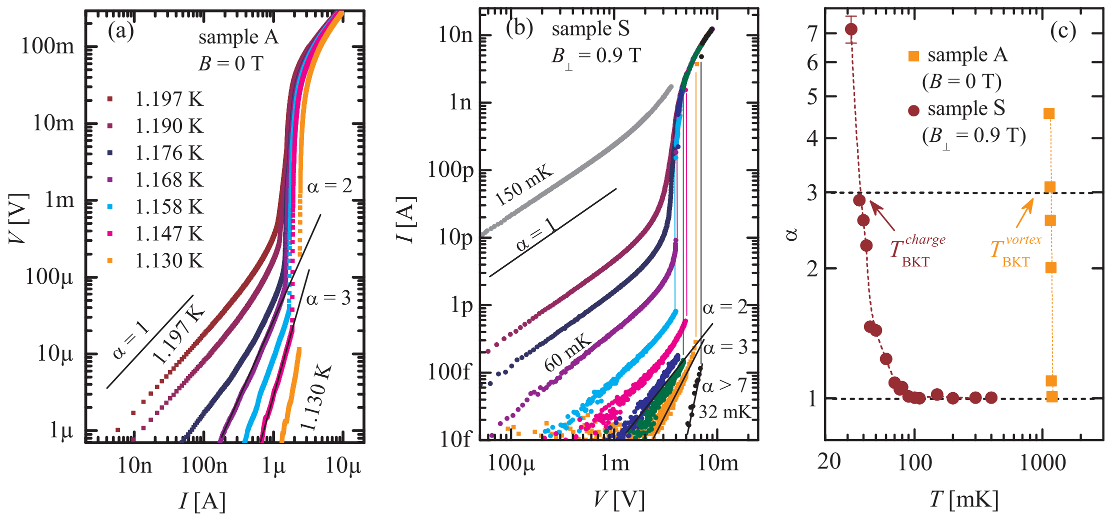

Figure 5.11: (a) $V(I)$ characteristics of sample A at indicated temperatures. (b) $I(V)$ characteristics of sample B at $B_\perp = 0.9\,\mathrm{T}$ and $T = 150, 100, 80, 70, 60, 50, 45, 42, 40, 37$ and $32\,\mathrm{mK}$ from top to bottom. Solid lines indicate the slopes corresponding to different values of power α in the $V \propto I^\alpha$ (sample A) $I \propto V^\alpha$ (sample B). (c) $\alpha(T)$ for sample A ($B = 0\,\mathrm{T}$) and sample B ($B_\perp = 0.9\,\mathrm{T}$) (line is a guide for an eye). Horizontal lines indicate Ohmic regime ($\alpha = 1$) and charge/vortex BKT-transition condition ($\alpha = 3$).

role of vortices. At low bias voltage and low temperature the current is mediated by tunneling of charges (Cooper pairs) and anti-charges (a deficit in Cooper pairs) between the superconducting granules. As long as the lateral system size does not exceed the electrostatic screening length the attraction between charges and anti-charges varies logarithmically with distance and a charge-BKT transition occurs [35,60]. For the charge BKT transition similar non-linear $I(V)$ characteristics as for the vortex BKT transition are expected, as the number of dissociated charge - anticharge pairs increases with bias voltage. In the thermodynamic limit, the exponent α should jump from $\alpha = 1$ to $\alpha = 3$ at T_{BKT}. In a real system this jump is smeared by finite size effects, and by inhomogeneities [47,48]. The transition from superconducting to insulating behavior in JJA can be controlled by a magnetic field [60] analogously to the films. Because of these strong similarities, it was recently suggested that the mechanism of the superconductor-insulator transition in TiN may be of similar nature as that in JJAs [17,28].

The striking duality of the behavior of our TiN films observed in the experiments supports the interpretation of the data in terms of Josephson junction arrays and the notion of the superinsulating state as the low-temperature charge-BKT phase. This interpretation is further supported by the strongly non-monotonic magnetoresistance (see Fig. 5.4c) and the absence of power-law $I(V)$ characteristics in parallel magnetic field. The charge BKT transition is expected to lead also to profound changes in the electronic excitation spectrum of the films. In order to prove the importance of long-ranged

Coulomb interaction in our films, which are an essential element of the charge-BKT transition, a tuning of the electromagnetic environment of the samples, e.g., by means of a conducting ground plane would be highly desirable.

The measurements of $I(V)$ characteristics of thin TiN films revealed a power law dependences at low temperature on either side of the superconductor-insulator transition. This dual behavior corresponds to the picture of superconductor-superinsulator transition derived in the framework of the Josephson junction array model.

5.4 Magnetoresistance

In this chapter, the magnetic field dependence of the resistance is probed further. As seen already in the $I(V)$'s, the resistance is changing dramatically and moreover the low bias linear regime, where the resistance can be extracted, is strongly field dependent. The resulting experimental challenge, when measuring in the AC setup, is to ensure that the AC excitation is within the linear regime but big enough to measure high resistances and small resistances, respectively.

In figure 5.12 the magnetoresistance close to zero field is presented. The low field, low resistance data was taken applying a current excitation ($I_{AC} = 0.4$ nA) much lower than the critical current at zero field ($I_c \approx 9$ nA). The high resistance data was measured employing a voltage excitation ($V_{AC} = 4$ μV) small enough to be in the linear regime in the $I(V)$. At zero field the sample is still superconducting but is getting insulating with applied field. When the resistance is getting bigger the setup is changed from current to voltage bias such that the sensitivity is high enough and the Joule power is kept low. The crossover between these setups is overlapping which indicates that the Joule power was small enough in both setups. Between 10-130 mT the resistance shows an exponential increase $B \propto \exp(B/B_0)$ (dashed line is guide to the eye) with $B_0 = 25.8$ mT. The inset shows a zoom near $B = 0$. Around zero field the magnetoresistance is linear.

The high field magnetoresistance was measured in the High Field Magnet Laboratory (HFML) in Nijmegen. The dilution unit has a base temperature of 50mK and is designed to minimize eddy currents. The resistive magnet can reach magnetic fields up to 30 T. The usual sweep rate was 1 T/min, reducing further eddy current heating. The magnetoresistance traces for out of plane field orientation are presented in fig. 5.13. At zero field the resistance is decreasing with lower temperature because it is still a superconducting sample. With lower temperature, the resistance develops a peak at 1.1 T with a steep positive magnetoresistance (five orders of magnitude increase between zero to one Tesla) at the lower field side and long decay of the resistance at the higher field side. The resistance is increasing with lower temperature for all fields above the magnetoresistance peak. The resistance is saturating at the high field side at ≈ 30 kΩ for temperatures below 150 mK. This resistance value is close to the quantum resistance $h/e^2 = 25.8$kΩ and much higher than for zero field.

Next, we focus on the size dependence of the magnetoresistance. As a reminder, it is crucial for size dependent measurements that the material in all sizes should be the same. Additionally, the steep temperature dependence of the resistance demands a very stable and reproducible temperature. Since on the chip of sample I several squares of several sizes are patterned the problems can be avoided when measuring simultaneously: The sizes $240, 20, 5, 2, 0.5$ μm were also measured in the HFML laboratory. In fig. 5.14 the magnetoresistance curves at $T = 82$ mK is presented. We see that there is still an increase in resistance at low fields and a maximum at ≈ 1.3 T except for 0.5 μm. After the maximum the resistance decreases and all curves, with sizes below 240 μm, converge

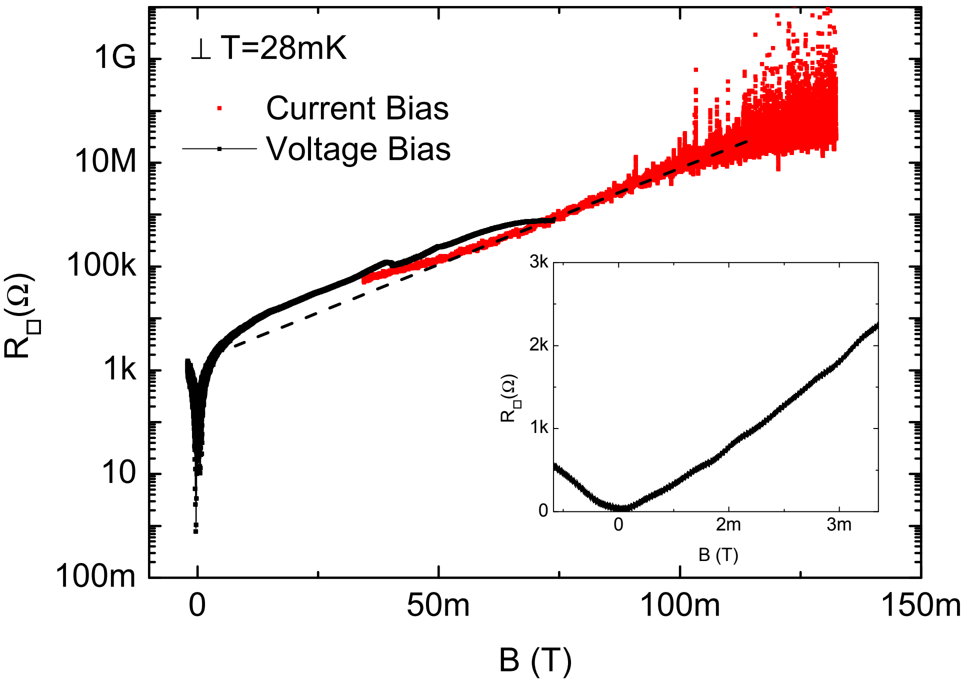

Figure 5.12: Low field magnetoresistance sample S: The low field, low resistance data was taken applying a current excitation ($I_{AC} = 0.4$ nA) much lower than the critical current at zero field ($I_c \approx 9$ nA). The high resistance data was measured employing a voltage excitation ($V_{AC} = 4$ μV) small enough to be in the linear regime in the $I(V)$. Dashed line shows exponential increase of the resistance. Inset: Zoom around $B = 0$

in a resistance window between $50 - 70$kΩ at high fields. This value is again close to the quantum resistance $h/e^2 = 25.8$kΩ. We note that, the $L = 240\mu$m sample shows an exponential decrease between 10 and 30 T.

The high field saturation was already observed for TiN up to 16T before [8] but these measurements confirm it for an insulating sample, several sample sizes and up to 30T magnetic fields. As mentioned in [8] the saturation in the order of the magnetoresistance is known for many other materials as well, e.g. Be [65] and InO [4] and High T_c superconductors [66]. This high field state was named "quantum metallicity" due to its metallic behavior and its apparent quantum origin.

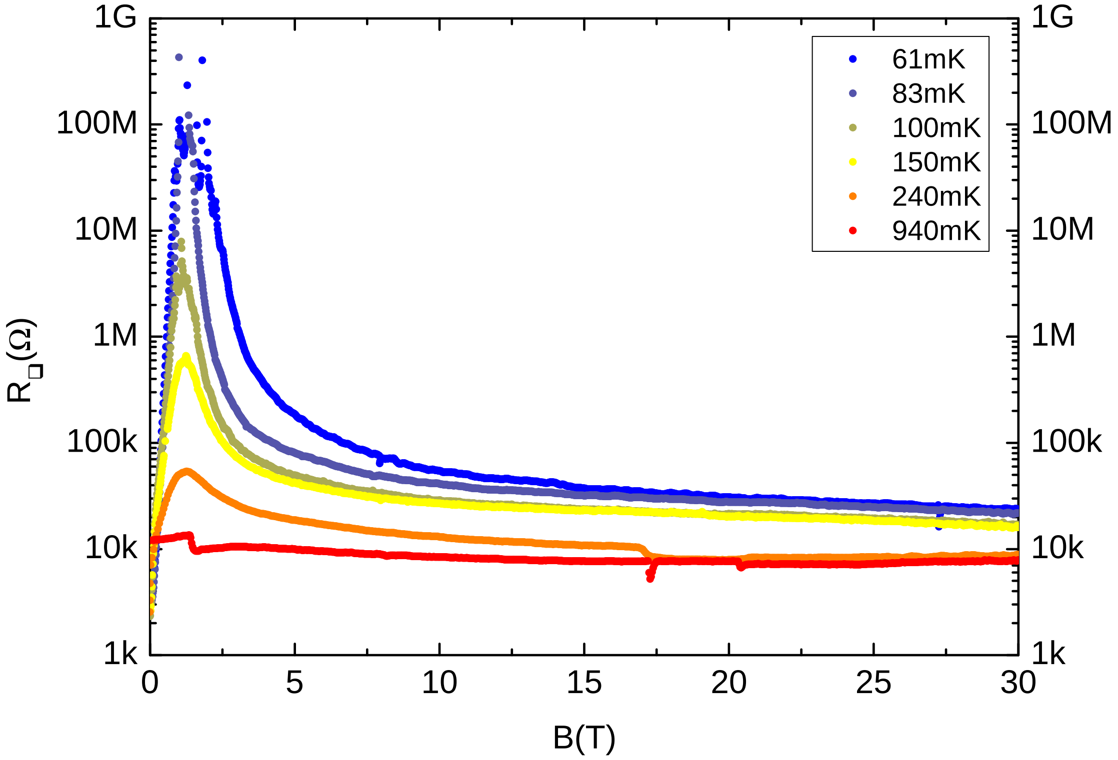

Figure 5.13: Sample S high field magnetoresistance: $R_\square$ in perpendicular field for temperatures $T = 60, 83, 100, 150, 240, 940$ mK. The maximum is reached at $\approx$ 1.3 T

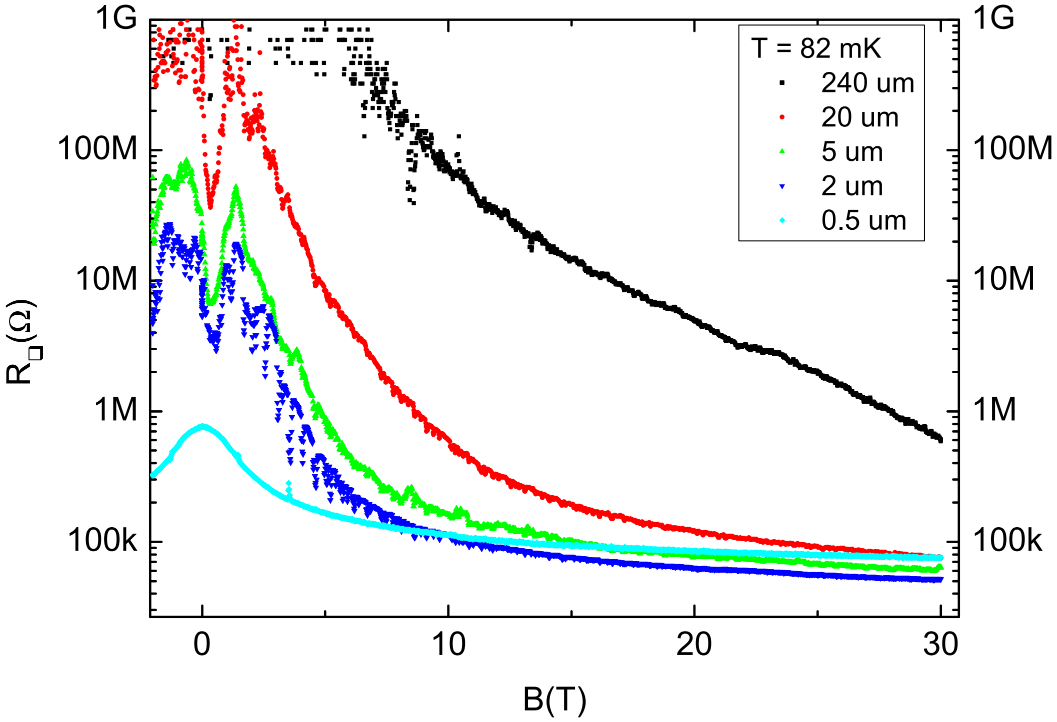

Figure 5.14: Size dependence of magnetoresistance of sample I in perpendicular magnetic fields: Isotherms at T =82 mK for sample sizes 240, 20, 5, 2, 0.5 µm

Chapter 6

Discussion

In this thesis high resolution dc measurements were presented from TiN-films close to the transition. Sample S is superconducting and shows a magnetic field induced SI transition. Sample I is already insulating at zero magnetic field and is above the disorder induced SI transition.

$R(T)$

The temperature dependence of the resistance of the insulating state follows an Arrhenius law at low temperatures for both samples. For sample S the resistance (see fig. 5.4a) in perpendicular field turns out to be several orders of magnitude larger than in parallel field. Similar results were found in amorphous InO [57] which shows a significant anisotropy in its B-SIT behavior.[1] One main result is the observation that the activation energy of sample I is increasing logarithmically with the sample size. So far, such behavior with logarithmic increasing activation energy with system size was observed only in InO films [27], where the temperature range was much smaller than in our case. Striking differences between sample S and I occur at low temperatures where the resistance of the smaller samples of I are saturating. In Josephson junction arrays [58] a similar saturation of the resistance was found.

The superconducting state of sample S shows an activated behavior in the conductance. Such "inverse Arrhenius law" behavior is known for artificial Josephson junction arrays [50] and for granular films [12]. In quasi-homogeneous system, like the measured film, such dependences have not been observed [19] at zero magnetic fields. Interestingly, associating the extracted activation energy with a Josephson coupling energy yield a critical current close to the measured critical current. It is remarkable that the used assumptions in the Josephson junction picture yield good agreements with the ex-

---

[1] Note that between the measurements of the two field orientations the sample has to be warmed up at room temperature in order to rotate the stage manually which could change the sample. A difference in the room temperature sheet resistance was not observed. Since the sample is near the transition a small, not observable change in the sample could lead to a change in the low temperature behavior. For future experiments an in-situ rotation is desirable.

perimental and predicted values. Whether the supposed Josephson junction is due to inhomogeneities in the sample or dynamically generated remains so far unclear. We note that there are several other effects leading to an activated behavior, e.g, single vortex excitation and flux creep, but they exists only at finite magnetic field.

The charge dominated Josephson junction network analysis of the activated temperature behavior described most of the data with respect to sample size and magnetic field dependence in perpendicular fields. The magnetoresistance peak of the activation energy vs. magnetic field is explained by the constraints (analogous to the SQUID) for the phase ($\Delta\phi_{\text{loop}} = 2\pi n$) of four junctions forming a loop. However, this scheme cannot explain the SI transition in the parallel field. Even in perpendicular field only one magnetoresistance peak is observed in the samples. This can be due to inhomogeneities in the junctions such that the smallest loop dominates. The above described magnetic field correction to the Josephson junction energy assumes a constant order parameter Δ_S in magnetic field. This assumption is valid only if the oscillations are far away of the critical field. Therefore, the bare Josephson energy has to incorporate the magnetic field dependence of the order parameter Δ_S. Concluding from the Ambagaokar-Baratoff formula, the Josephson energy depends linearly on the superconducting gap at low temperatures. Therefore, the Josephson junction energy is modulated by the magnetic field dependence of the order parameter $\Delta(B)$, provided the normal tunnelling resistance remains constant with magnetic fields. In Ref. [67] the Josephson energy is modulated by $\sqrt{1-(B/B_c)^2}$. The fact that there is also a peak in parallel field orientation, where no phase difference is acquired from the magnetic field in the smallest loop, supports a change in the order parameter.

The activation energy in the insulating Josephson junction network is given by the activation of Cooper pair charge solitons $E_a = \Delta_C$. However, if the charging energy is large compared to the gap Δ_S it is energetically easier to break the pair and creating a single electron soliton, thus reducing the charging energy to $1/4\Delta_C$ with Δ_C the charging energy of a cooper pair. The resulting activation energy is given by

$$E_a = \Delta_C/4 + \Delta_S(B) \tag{6.1}$$

This transition from Cooper pair solitons to single-electron solitons was found in artificial Josephson junction arrays [58]. The transition occurs at $\Delta_S/\Delta_C = 2$: For larger values, $\Delta_S/\Delta_C > 2$, Cooper pair solitons are responsible for the charge transport while for smaller values $\Delta_S/\Delta_C < 2$ single electron solitons are created by breaking up Cooper pairs. For sample I a charging energy can be extracted from the logarithmic sample size dependence (see Fig. 5.4) of the activation energy of $E_C/k_B = 0.2\,\text{K}$. Unfortunately, there is no direct measurement of the superconducting gap Δ_S in sample I. From the activated behavior in the conductance of the superconducting state at zero field of sample S a gap can be estimated by the Ambagaokar-Baratoff formula of $\Delta_S/k_B \approx 0.3$-$0.6\,\text{K}$. This value is close to the expected value at the SI transition [23]. We note that the normal resistance of the tunnel junction for this analysis is unknown. As a crude estimate the normal sheet resistance at room temperature was used for the calculation

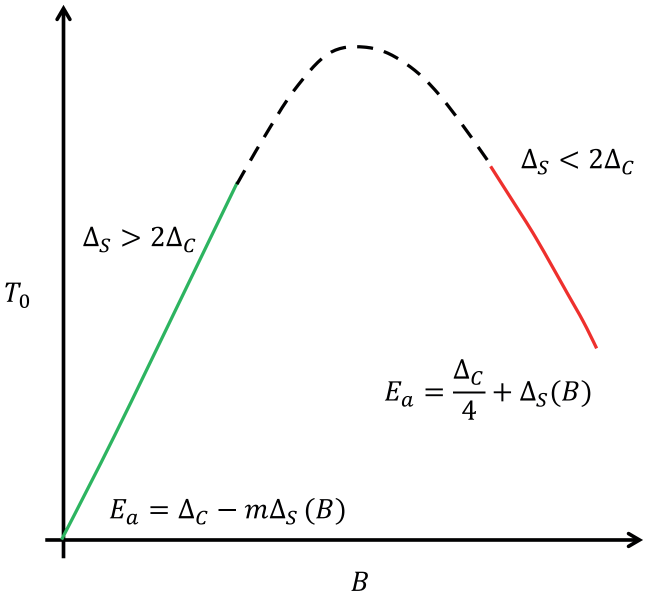

Figure 6.1: Schematic activation energy crossover with magnetic field dependent superconducting gap in parallel field orientation. The green line corresponds to Cooper pair excitations.The red line correspond to electron excitations. The superconducting gap $\Delta_S(B)$ is assumed to decrease monotonously with increasing magnetic fields.

of the superconducting gap. Assuming E_C as a a lower limit of the charging energy, a ratio of $\Delta_S/E_C = 1.5$-3 can be estimated. This means that a transition from Cooper pair excitations to single electron excitations can occur in magnetic fields. Even with the extrapolated superconducting gap near the SI transition [23] of $\Delta_S/k_B = 1\,\mathrm{K}$ the ratio Δ_S/Δ_C is only 5. This value is above the critical value and Cooper pair excitations are expected. For the microscopic models [25, 26], with their Anderson like on site disorder, the previous estimates imply that the charging energy cannot be neglected and should be incorporated.

If the charging energy and the gap energy are comparable, a crossover between Cooper pair excitation and electron excitations can happen. In parallel magnetic field phase corrections in the Josephson array do not exist. However, the gap energy Δ_S can be reduced. In figure 6.1 the following scenario is sketched. With increasing magnetic fields the superconducting gap is decreasing monotonously. The Josephson Energy is given by $E_J = I_c\phi_0/(2\pi) = \Delta_S(0)\phi_0/(4eR_N)$. At small field $\Delta_S > 2\Delta_C$ and therefore Cooper pair excitations are preferred. Hence, the corrected charging energy (see equation (5.2)) with respect to the Josephson coupling is given by

$$k_B T_0 = \Delta_C - m\Delta_S(B) \tag{6.2}$$

$$m = \alpha \frac{\phi_0}{4eR_N} \frac{\Delta_C}{E_C} \quad . \tag{6.3}$$

The superconducting gap can be approximated in a Taylor series around zero field with

$\Delta_S(B) = \Delta_{S0} - \Delta'|\frac{B}{B_C}| + \ldots$. Therefore, the change of the activation energy with small increasing magnetic field is linear and positive. At high fields $\Delta_S < 2\Delta_C$, thus electron excitations are preferred (red line) and the activation energy is given by (6.1). The activation energy is decreasing with increasing magnetic fields because $\Delta_S(B)$ is decreasing. The dashed line indicates the crossover region between the two excitations. With this scenario it is possible to explain the observed non-monotonic behavior of the activation energy even with a monotonously decreasing pairing energy of the Cooper pairs in magnetic fields. Furthermore, it is possible to explain qualitatively why the most insulating samples do not show a positive magnetoresistance at low fields. In these sample the charging energy is already too high at zero field and electron excitations are preferred.

$I(V)$

Non-linear behavior in the isotherms is found at high and low-bias in the insulating state of both samples. The low-bias non-linearity can be an indication for a charge-BKT transition, explained in section 2.4.

Another main result is the analysis of the low-bias non-linearities in the highly insulating state of sample S and I. The exponent α in $I \propto V^\alpha$ increases continuously from the power 1 at high temperatures to the power 3 and above at low temperatures. With the notion of the vortex-BKT transition this increase is an expected characteristic signature for a charge-BKT transition. In the thermodynamic limit, the exponent α should jump from $\alpha = 1$ to $\alpha = 3$ at T_{BKT}. In a real system on the vortex side this jump is smeared by finite size effects, and by inhomogeneities [47, 48] and thus a similar effect can be expected for the charge BKT-transition. From the electron-overheating simulation it can be excluded that this non-linearity is due to simple overheating. The duality between the vortex-BKT transition and the charge-BKT transition is presented in 5.3.1. Recently, similar current-voltage characteristics were found in charge-ordered layered organic molecular crystals [68]. Its temperature dependence of the resistance shows activated behavior and a smooth increase of the exponent of the $I(V)$ as well. The cusp like temperature dependence of the resistance near the supposed charge-BKT transition was not found too. This absence can be due to inhomogeneities and finite size effects. In this work it is pointed out that the Poole-Frenkel effect, known from trapped charges in semiconductors and insulators, creates the identical [68] non-linear behavior. This argument is valid for our low-bias non-linearity too. However, in the above considerations the Poole-Frenkel effect implies a 2D long range Coulomb interaction as well.

The high bias non-linearity and in particular the current jumps can be mainly attributed to electron overheating. The high resistive state of sample S in $B_\perp$ deviates from the electron-phonon decoupling model and moreover this deviation develops in the temperature range where the low-bias non-linearity emerges (see section 5.3). The same observation is made in sample I. For samples which show the low-bias non-linearity the electron-phonon decoupling model deviates from the measured isotherms at low temperatures. However, the model is sufficient to reproduce the isotherms even at low low-bias non-linearity if the electron-phonon coupling is used as a free parameter and is extracted from the high-bias analysis of the specific length . Interestingly, the extracted electron-phonon coupling appears to decrease with increasing system size. From the performed simulations we can conclude that the electron-phonon coupling Γ has to be replaced by a temperature dependent $\Gamma(T)$ which has to decrease at low temperatures for a better fit of the maximal switching voltage. Note, that in this reasoning the exponent in the heat balance equation was assumed fixed. The system size dependence of Γ may indicate more dramatic changes compared to metallic behavior in the electron excitation spectrum. The change in the electronic spectrum leads to a reduced phase space of the scattering integral of the electron-phonon coupling, thus to smaller values of Γ. This reasoning can explain why the electron-phonon coupling is decreasing with increasing system size in sample I: The activation energy is increasing with increasing system size and therefore pushing a significant change of the electronic density of states to higher observable temperatures. In order to prove the electron-overheating model further a direct measurement of the electron temperature or the density of states is desirable.

A possible mechanism for the random switching can be an electric breakdown mechanism with depinning of charges or charge-anti-charge pairs that creates an avalanche. Similar $I(V)$ behavior with current jumps and hysteresis has been also observed in a variety of other systems including insulating amorphous YSi [51] and 2D Josephson junction networks [58, 60] in the insulating state. It was remarked that switching in YSi at very low temperatures resulted from the interplay between depinning transition of the high resistive state and overheating of electronic system, but cannot be explained by the overheating alone. Similar multiple jumps were observed before in non-superconducting, quantum dot arrays [61] and recently in indium oxide [62]. These similarities support further the important role of electron-electron interaction effects in the insulating state of the SI transition.

Concluding remarks

The activated temperature dependence of the resistance and its size and magnetic field dependence, the multiple current jumps and the broad threshold voltage distribution suggest a charge dominated scenario. A charge-BKT transition can explain these findings consistently. The logarithmic scaling of the activation energy with the system size over more than two orders of magnitude (see Fig.5.4) indicates a formation of a long ranged highly correlated state. The fact that there is no observed saturation of the effect at the half a millimetre reaching samples are astonishing and unexpected because conventional electrostatic screening lengths are much smaller. In fact the insulating character is pronounced better at the larger samples. Deviations occur at the smaller samples. The absence of the cusp like temperature dependence of the resistance near the transition temperature is an open question but with the notion of the observations in the vortex-

BKT transition [48] not unusual. There are other mechanism which can create the found low-bias non-linearity, e.g., a change in the electronic density of states or the Poole-Frenkel effect, but they can explain only this specific dependency and not all dependences. Whether the excitations of the activated behavior are electrons or Cooper pairs cannot be determined. From the approximated ratio between charging energy and superconducting gap both scenarios are possible and moreover a transition from Cooper pair to electron excitations can occur as well. For further investigation a direct measurement of the superconducting gap in the insulating regime and its magnetic field dependence is desirable. In order to prove the importance of long-ranged Coulomb interaction in our films, which are an essential element of the charge-BKT transition, a tuning of the electromagnetic environment of the samples, e.g., by means of a conducting ground plane, would be highly interesting.

Chapter 7

Summary and Outlook

In this thesis the superconductor-insulator transition in titanium nitride films was investigated. In particular, the non-linear conductance was examined. The results were analyzed in the framework of Josephson junction arrays. The effect of electron overheating was investigated and current-voltage characteristics simulations were performed.

Two types of samples were measured. Sample S is on the superconducting side just below the disorder driven SI transition and the magnetic field dependence was examined. Sample I consists of different square shaped samples of different length on one chip. These samples are already insulating at zero magnetic field and the length dependence of the insulating state is probed.

As an experimental achievement, the dc current resolution could be improved down to a few femto amperes which enabled the measurement of a finite current below the current jumps in the insulating state. Below the current jumps at finite bias voltage in the insulating state at low temperatures low bias non-linearities in $I(V)$ are discovered. The current jumps in the $I(V)$ develop a broadened switching distribution with decreasing temperatures. Above the first jump multiple jumps are found. Extensive simulations of the electron-phonon decoupling could reproduce the high bias-behavior of the isotherms and the onset of the current jumps. With these simulations it can be excluded that a global electron-heating can explain the low-bias non-linearities. The appearance of low-bias non-linearities coincides with deviations between the electron-phonon decoupling simulated isotherms and the measured isotherms. Investigating further the low-bias non-linearities revealed a temperature dependence of the exponent in $I \propto V^{\alpha}$, which is dual (swapping current and voltage) to the vortex BKT transition. This increase in the exponent is found in both samples.

The insulating state shows activated temperature dependence of the resistance. The logarithmic sample size dependence of the activation energy in the insulating state was measured for the first time in titanium nitride. The evolution of the activation energy in magnetic field and in sample size can be explained within the framework of 2D Josephson junction arrays: The activation energy in this model is determined by a collective charging energy and first order perturbation theory with respect to the Josephson coupling. In insulating arrays a low temperature state with frozen charge dipoles is postulated. The melting process in 2D in this model is described by the charge BKT-transition. We note that a hallmark in the vortex BKT transition in superconductors is a change in the exponent in the non-linear $I(V)$ characteristics $V \propto I^{\beta(T)}$. The experimentally found temperature dependence of the exponent $I \propto V^{\alpha(T)}$ can be attributed to the charge-BKT transition. The temperature dependence can differ from the pure thermodynamic limit due to additional thermal excitations.

The high-bias non-linearities, including the jump in the current-voltage characteristics, can be explained and simulated within the electron overheating model. However, the high resistive state of sample S in $B_\perp$ and for the larger squares of sample I at low temperatures deviates from the electron-phonon decoupling model and moreover this deviation develops in the temperature range where the low-bias power law dependence of $I(V)$ deviates from linear Ohmic law.

Recent scanning tunnelling measurements revealed pseudo-gapped regions in the superconducting state. Calculations showed that this gap can be reproduced by on-site, Anderson like, disorder. It is assumed that charging effects can be neglected. However, in this thesis the insulating state dependence on magnetic fields, temperature, length of the sample and low-voltages could be explained with a charge dominated Josephson junction array model. The increase of the exponent in the power law dependence is a strong evidence for the charge Berezinskii-Kosterlitz-Thouless transition. The current jumps in the highly insulating state support a charge driven switching mechanism as well. Therefore, the results suggest that charging effects must be included into microscopical models, to reach a satisfactory understanding. In particular, the dielectric properties of the pseudo-gapped regions, found in scanning tunnelling measurements and in calculations, are of interest.

In order to test the charge dominated regime, future experiments should probe the gate dependence of the transport properties. Additionally, systematic investigations of different length-width ratios should reveal the relevance of percolation effects. Smaller samples should probe further the system size effects.

Bibliography

[1] D. B. Haviland, Y. Liu, and A. M. Goldman. Onset of superconductivity in the two-dimensional limit. *Physical Review Letters*, 62:2180–2183, May 1989.

[2] P.W. and Anderson. Theory of dirty superconductors. *Journal of Physics and Chemistry of Solids*, 11(1-2):26 – 30, 1959.

[3] AF Hebard and MA Paalanen. Magnetic-field-tuned superconductor-insulator transition in two-dimensional films. *Physical Review Letters*, 65(7):927–930, August 1990.

[4] VF Gantmakher, MV Golubkov, VT Dolgopolov, GE Tsydynzhapov, and AA Shashkin. Scaling analysis of the magnetic field-tuned quantum transition in superconducting amorphous In-O films. *JETP Letters*, 71(4):160–164, 2000.

[5] TI Baturina, DR Islamov, J Bentner, C Strunk, MR Baklanov, and A Satta. Superconductivity on the localization threshold and magnetic-field-tuned superconductor-insulator transition in TiN films. *JETP Letters*, 79(7):337–341, 2004.

[6] VF Gantmakher, MV Golubkov, JGS Lok, and AK Geim. Giant negative magnetoresistance of semi-insulating amorphous indium oxide films in strong magnetic fields. *Zh. Eksp. Teor. Fiz*, 109:1765–1778, 1996.

[7] G Sambandamurthy, LW Engel, A Johansson, and D Shahar. Superconductivity-related insulating behavior. *Physical Review Letters*, 92(10):107005, 2004.

[8] T. Baturina, C. Strunk, M. Baklanov, and A. Satta. Quantum Metallicity on the High-Field Side of the Superconductor-Insulator Transition. *Physical Review Letters*, 98(12):1–4, March 2007.

[9] D. Shahar and Z. Ovadyahu. Superconductivity near the mobility edge. *Physical Review B*, 46(17):10917–10922, 1992.

[10] T. Baturina, a. Mironov, V. Vinokur, M. Baklanov, and C. Strunk. Localized Superconductivity in the Quantum-Critical Region of the Disorder-Driven Superconductor-Insulator Transition in TiN Thin Films. *Physical Review Letters*, 99(25):1–4, 2007.

[11] G. Sambandamurthy, L. Engel, a. Johansson, E. Peled, and D. Shahar. Experimental Evidence for a Collective Insulating State in Two-Dimensional Superconductors. *Physical Review Letters*, 94(1):1–4, 2005.

[12] Aviad Frydman. The superconductor insulator transition in systems of ultrasmall grains. *Physica C: Superconductivity*, 391(2):189–195, August 2003.

[13] Yoichi Ando, G. Boebinger, A. Passner, Tsuyoshi Kimura, and Kohji Kishio. Logarithmic Divergence of both In-Plane and Out-of-Plane Normal-State Resistivities of Superconducting La2-xSrxCuO4 in the Zero-Temperature Limit. *Physical Review Letters*, 75(25):4662–4665, December 1995.

[14] M. Ovadia, B. Sacépé, and D. Shahar. Electron-Phonon Decoupling in Disordered Insulators. *Physical Review Letters*, 102(17):1–4, 2009.

[15] B.L. Altshuler, V.E. Kravtsov, I.V. Lerner, and I.L. Aleiner. Jumps in current-voltage characteristics in disordered films. *Physical Review Letters*, 102(17):176803, 2009.

[16] Matthew P. A. Fisher. Quantum phase transitions in disordered two-dimensional superconductors. *Physical Review Letters*, 65:923–926, Aug 1990.

[17] M. Fistul, V. Vinokur, and T. Baturina. Collective Cooper-Pair Transport in the Insulating State of Josephson-Junction Arrays. *Physical Review Letters*, 100(8):1–4, 2008.

[18] M. V. Feigel'man, L. B. Ioffe, and M. Mézard. Superconductor-insulator transition and energy localization. *Physical Review B*, 82:184534, Nov 2010.

[19] Vsevolod F Gantmakher and Valery T Dolgopolov. Superconductor-insulator quantum phase transition. *Physics-Uspekhi*, 53(1):1–49, January 2010.

[20] Amit Ghosal, Mohit Randeria, and Nandini Trivedi. Role of Spatial Amplitude Fluctuations in Highly Disordered s-Wave Superconductors. *Physical Review Letters*, 81(18):3940–3943, November 1998.

[21] Yonatan Dubi, Yigal Meir, and Yshai Avishai. Nature of the superconductor-insulator transition in disordered superconductors. *Nature*, 449(7164):876–80, October 2007.

[22] Karim Bouadim, Yen Lee Loh, Mohit Randeria, and Nandini Trivedi. Single- and two-particle energy gaps across the disorder-driven superconductor-insulator transition. *Nature Physics*, 7(7):1–6, July 2011.

[23] B. Sacepe, C. Chapelier, T. I. Baturina, V. M. Vinokur, M. R. Baklanov, and M. Sanquer. Disorder Induced Inhomogeneities of the Superconducting State Close to the Superconductor Insulator Transition. *Physical Review Letters*, 157006(October):4, 2008.

[24] Benjamin Sacépé, Thomas Dubouchet, Claude Chapelier, Marc Sanquer, Maoz Ovadia, Dan Shahar, Mikhail Feigel'man, and Lev Ioffe. Localization of preformed Cooper pairs in disordered superconductors. *Nature Physics*, 7(3):239–244, January 2011.

[25] Mintu Mondal, Anand Kamlapure, Madhavi Chand, Garima Saraswat, Sanjeev Kumar, John Jesudasan, L. Benfatto, Vikram Tripathi, and Pratap Raychaudhuri. Phase Fluctuations in a Strongly Disordered s-Wave NbN Superconductor Close to the Metal-Insulator Transition. *Physical Review Letters*, 106(4):1–4, January 2011.

[26] Mikhail Feigel'man, Lev Ioffe, and M. Mézard. Superconductor-insulator transition and energy localization. *Physical Review B*, 82(18):1–25, November 2010.

[27] D Kowal and Z Ovadyahu. Scale dependent superconductor-insulator transition. *Physica C: Superconductivity*, 468(4):322–325, February 2008.

[28] Valerii M Vinokur, Tatyana I Baturina, Mikhail V Fistul, Aleksey Yu Mironov, Mikhail R Baklanov, and Christoph Strunk. Superinsulator and quantum synchronization. *Nature*, 452(7187):613–5, 2008.

[29] C. J. Lobb and D. J. Frank. Percolative conduction and the Alexander-Orbach conjecture in two dimensions. *Physical Review B*, 30:4090–4092, Oct 1984.

[30] W. Buckel and R. Hilsch. Supraleitung und Widerstand von Zinn mit Gitterstörungen. *Zeitschrift für Physik A Hadrons and Nuclei*, 131:420–442, 1952. 10.1007/BF01329552.

[31] Werner Buckel. Elektronenbeugungs-Aufnahmen von dünnen Metallschichten bei tiefen Temperaturen. *Zeitschrift für Physik A Hadrons and Nuclei*, 138:136–150, 1954. 10.1007/BF01337905.

[32] A M Finkel'stein. Suppression of superconductivity in homogeneously disordered systems. *Physica B: Condensed Matter*, 197(1-4):636–648, March 1994.

[33] P.W. Anderson, K. Muttalib, and T. Ramakrishnan. Theory of the "universal" degradation of T_{c} in high-temperature superconductors. *Physical Review B*, 28(1):117–120, July 1983.

[34] L. Cooper and D. Feldman. Bardeen-Cooper-Schrieffer theory. *Scholarpedia*, 3(11):6439, 2008.

[35] Rosario Fazio and Herre van der Zant. Quantum phase transitions and vortex dynamics in superconducting networks. *Physics Reports*, 355(4):235 – 334, 2001.

[36] Vinay Ambegaokar and Alexis Baratoff. Tunneling between superconductors. *Physical Review Letters*, 10:486–489, Jun 1963.

[37] Vinay Ambegaokar and Alexis Baratoff. Tunneling between superconductors. *Physical Review Letters*, 11:104–104, Jul 1963.

[38] Edmond Chow, Per Delsing, and David Haviland. Length-Scale Dependence of the Superconductor-to-Insulator Quantum Phase Transition in One Dimension. *Physical Review Letters*, 81(1):204–207, July 1998.

[39] JE Mooij, BJ Van Wees, LJ Geerligs, M. Peters, R. Fazio, and G. Schön. Unbinding of charge-anticharge pairs in two-dimensional arrays of small tunnel junctions. *Physical Review Letters*, 65(5):645–648, 1990.

[40] R. Fazio and G. Schön. Charge and vortex dynamics in arrays of tunnel junctions. *Physical Review B*, 43(7):5307–5320, 1991.

[41] M. Tinkham, David W. Abraham, and C. J. Lobb. Periodic flux dependence of the resistive transition in two-dimensional superconducting arrays. *Physical Review B*, 28(11):6578–6581, Dec 1983.

[42] J.M. Kosterlitz and D.J Thouless. Ordering , metastability and phase transitions in two-dimensional systems. *Solid State Physics*, 6, 1973.

[43] B. I. Halperin and David R. Nelson. Resistive transition in superconducting films. *Journal of Low Temperature Physics*, 36(5-6):599–616, September 1979.

[44] A. P. Young. Melting and the vector Coulomb gas in two dimensions. *Physical Review B*, 19:1855–1866, Feb 1979.

[45] J. Pearl. Current distribution in superconducting films carrying quantized fluxoids. *Applied Physics Letters*, 5(4):65, 1964.

[46] David R. Nelson and J. M. Kosterlitz. Universal jump in the superfluid density of two-dimensional superfluids. *Physical Review Letters*, 39:1201–1205, Nov 1977.

[47] A. M. Kadin, K. Epstein, and A. M. Goldman. Renormalization and the Kosterlitz-Thouless transition in a two-dimensional superconductor. *Physical Review B*, 27:6691–6702, Jun 1983.

[48] L. Benfatto, C. Castellani, and T. Giamarchi. Broadening of the Berezinskii-Kosterlitz-Thouless superconducting transition by inhomogeneity and finite-size effects. *Physical Review B*, 80:214506, Dec 2009.

[49] D. J. Resnick, J. C. Garland, J. T. Boyd, S. Shoemaker, and R. S. Newrock. Kosterlitz-Thouless transition in proximity-coupled superconducting arrays. *Physical Review Letters*, 47:1542–1545, Nov 1981.

[50] H. S. J. Zant, H. A. Rijken, and J. E. Mooij. The superconducting transition of 2-D Josephson-junction arrays in a small perpendicular magnetic field. *Journal of Low Temperature Physics*, 79:289–310, 1990. 10.1007/BF00682288.

[51] F. Ladieu, M. Sanquer, and J. P. Bouchaud. Depinning transition in mott-anderson insulators. *Physical Review B*, 53(3):973–976, Jan 1996.

[52] Boris Altshuler, Vladimir Kravtsov, Igor Lerner, and Igor Aleiner. Jumps in Current-Voltage Characteristics in Disordered Films. *Physical Review Letters*, 102(17):1–4, 2009.

[53] A Savin, J Pekola, M Prunnila, J Ahopelto, and P Kivinen. Electronic Cooling and Hot Electron Effects in Heavily Doped Silicon on Insulator Film. *Physica Scripta*, T114:57–60, January 2004.

[54] D. Kalok, A. Bilušić, T. I. Baturina, A. Yu. Mironov, S. V. Postolova, A. K. Gutakovskii, A.V. Latyshev, V. M. Vinokur, and C. Strunk. Non-linear conduction in the critical region of the superconductor-insulator transition in tin thin films. *Journal of Physics: Conference Series (To be published)*, 2011.

[55] J. B. Johnson. Thermal agitation of electricity in conductors. *Phys. Rev.*, 32:97–109, Jul 1928.

[56] H. Nyquist. Thermal agitation of electric charge in conductors. *Phys. Rev.*, 32:110–113, Jul 1928.

[57] A. Johansson, I. Shammass, N. Stander, E. Peled, G. Sambandamurthy, and D. Shahar. Angular dependence of the magnetic-field driven superconductor-insulator transition in thin films of amorphous indium-oxide. *Solid State Communications*, 151:743–746, February 2011.

[58] P. Delsing, C. D. Chen, D. B. Haviland, Y. Harada, and T. Claeson. Charge solitons and quantum fluctuations in two-dimensional arrays of small josephson junctions. *Physical Review B*, 50:3959–3971, Aug 1994.

[59] Yakov Strelniker, Aviad Frydman, and Shlomo Havlin. Percolation model for the superconductor-insulator transition in granular films. *Physical Review B*, 76(22):1–6, December 2007.

[60] L. J. Geerligs, M. Peters, L. E. M. de Groot, A. Verbruggen, and J. E. Mooij. Charging effects and quantum coherence in regular josephson junction arrays. *Physical Review Letters*, 63:326–329, Jul 1989.

[61] C. I. Duruöz, R. M. Clarke, C. M. Marcus, and J. S. Harris, Jr. Conduction threshold, switching, and hysteresis in quantum dot arrays. *Physical Review Letters*, 74:3237–3240, Apr 1995.

[62] O. Cohen, Maoz Ovadia, and Dan Shahar. Electric breakdown effect in the current-voltage characteristics of amorphous indium oxide thin films near the superconductor-insulator transition. *Physical Review B*, 84(10):1–4, September 2011.

[63] D. Babić, J. Bentner, C. Sürgers, and C. Strunk. Flux-flow instabilities in amorphous $\mathrm{nb}_{0.7}\mathrm{ge}_{0.3}$ microbridges. *Physical Review B*, 69:092510, Mar 2004.

[64] K. Epstein, A. M. Goldman, and A. M. Kadin. Vortex-antivortex pair dissociation in two-dimensional superconductors. *Physical Review Letters*, 47:534–537, Aug 1981.

[65] V Y Butko and P W Adams. Quantum metallicity in a two-dimensional insulator. *Nature*, 409(6817):161–4, January 2001.

[66] M. Steiner, G. Boebinger, and a. Kapitulnik. Possible Field-Tuned Superconductor-Insulator Transition in High-Tc Superconductors: Implications for Pairing at High Magnetic Fields. *Physical Review Letters*, 94(10):1–4, March 2005.

[67] David Haviland and Per Delsing. Cooper-pair charge solitons: The electrodynamics of localized charge in a superconductor. *Physical Review B*, 54(10):R6857–R6860, September 1996.

[68] Yamaguchi Takahide, Motoi Kimata, Kaori Hazama, Taichi Terashima, Shinya Uji, Takako Konoike, and Hiroshi M. Yamamoto. Charge transport in charge-ordered layered crystals $\theta-(BEDT-TTF)_2MZn(SCN)_4$(M=Cs,Rb) : Effects of long-range Coulomb interaction and the Pauli exclusion principle. *Physical Review B*, 81(23), June 2010.

Acknowledgement

I would like to thank

- My advisor Prof. Dr. Strunk who gave me the possibility to work on this interesting topic. He gave me the support and the required measurement time to improve the experiment resolution and the measurement routines. The subsequent discussions of the results were very helpful.
- Prof. Dr. Grifoni who agreed to act as referee for my thesis.
- Dr. Ante Bilušić who introduced me to the experimental world of low temperature measurements, the organization of measurement data and was involved in most of the electron-phonon simulations. He also read this manuscript.
- Dr. Tatyana Baturina and Dr. Valerii Vinokur who belong to the leading experts in the superconductor-insulator transition in TiN and helped us to understand the data.
- Dr. Andreas Hüttel who put me in contact with the Perl interface Lab::Visa.
- Dr. Dominik Preusche who introduced me in the clean room work and in the field of carbon nanotubes.
- Prof. Dr. Weiss, who let me use his clean room facilities, his dilution fridge and other infrastructure at the chair.
- The Graduiertenkolleg 638 for financial support.
- Dr. Emiliano Pallecchi who gave me the suggestion to switch to titanium nitride finally and gave me some hints about Python programming in the beginning.
- Christian Haimerl and Thomas Solleder from the He-station who always succeeded in providing enough helium even in the toughest times.
- The electronic and machine workshop for their support.
- Our technicians Thomas Haller and Michael Weigl as well as the cleanroom engineers Cornelia Deinhart and Uli Gürster for assistance on many technical details.

- Our secretaries Claudia Rahm and Elke Haushalter, for the smooth handling of administrative tasks.
- Markus Gaaß for the hints and tips in Latex, Illustrator etc.
- Dipl.-Wirtsch.-Ing. Michael Faust for reading parts of this thesis carefully.
- Emilliano, Dominik, Daniel, Maurice, Sasmita and Lorenz for the good time in the office together and interesting conversations.
- All members of the group for the pleasant atmosphere.
- My friends, in particular Michael and Timm, who accompanied me during the last years.
- My parents and my sister for their support.